Impedance Spectroscopy as a Tool for the Electrochemical Study of Mixed Conducting Ceria

Thesis by

Wei Lai

In Partial Fulfillment of the Requirements

for the Degree of

Doctor of Philosophy

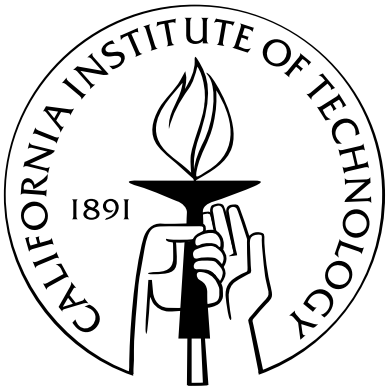

California Institute of Technology

Pasadena, California

2007

(Defended November 29, 2006)

Acknowledgements

First and foremost, I would like to thank my advisor, Professor Sossina Haile, who has always been a great mentor to me. I feel so grateful to her for her patience and support through the course of my research.

Secondly, I am indebted to the group members, Dr. Mary Thundathil, Dr. Zongping Shao, Dr. Tetsuya Uda, Dr. Jian Wu, Dr. Liping Li, Dr. Calum Chisholm, Dr. Dane Boysen, Ryan Merle, Lisa Cowan, Peter Babilo, Martin Smith-Martinez for their help with the experiments in the lab.

Next, I would like to thank Professor David Goodwin and his students Francesco Ciucci, Yong Hao and Vaughan Thomas for the help on the program codes. I would like to thank Jeffrey Krimmel for the technical support of the use of Rayleigh cluster. I would also like to thank Dr. Chi Ma for the help on the use of Scanning Electron Microscope, Mike Vondrus for the help of building the instrument, and Lou Zaharopoulos and Irene Loera for the general assistance in my work.

My warmest thanks to my wife Ping Lian. Without her understanding and support, this endeavor would not be possible.

Lastly, I would like to thank the Office of Naval Research, Office of Electrochemical Power Science and Technology through the Multidisciplinary University Research Initiative (MURI) program for funding this work.

Abstract

The A.C. impedance response of mixed ionic and electronic conductors (MIECs) is derived from first principles and quantitatively compared with experimental data of three model systems: p_{O_2}|Pt|$Sm_{0.15}Ce_{0.85}O_{2-\delta}$(1350 °C)|Pt|$p_{O_2}$ (system I), p_{O_2}|Pt|$Sm_{0.15}Ce_{0.85}O_{2-\delta}$(1550 - °C)|Pt|$p_{O_2}$ (system II), and $p_{O_2}(c)$|$Ba_{0.5}Sr_{0.5}Co_{0.8}Fe_{0.2}O_{3-\delta}$|$Sm_{0.15}Ce_{0.85}O_{2-\delta}$(1350 °C)|Pt|-$p_{O_2}(a)$ (system III). For the *equilibrium* systems I and II, which differ in terms of the preparation of the electrolyte, a broad spectrum of electrical and thermodynamic properties is extracted solely from the measurement of impedance spectra over wide oxygen partial pressure (10^{-31}–0.21 atm) and temperature ranges (500 to 650 °C). Electrolyte parameters derived from quantitative fitting of the impedance spectra include the concentration of free electron carriers, the mobilities for both ion and electron transport, the entropy and enthalpy of reduction of Ce^{4+} to Ce^{3+}, and, for system II, the space charge potential characterizing the grain boundary behavior. In addition, the electrochemical behavior of O_2 and H_2 at the Pt|ceria interface has been characterized from these measurements. Under oxidizing conditions, the data suggest an oxygen electro-reduction reaction that is rate limited by the dissociated adsorption/diffusion of oxygen species on the Pt electrode, similar to Pt|zirconia. Under reducing conditions, the inverse of the electrode polarization resistivity obeys a $p_{O_2}^{-1/4}$ dependence, with an activation energy that is similar to that measured for the electronic conductivity. These results suggest that ceria is electrochemically active for hydrogen electro-oxidation and that the reaction is limited by the rate of removal of electrons from the ceria surface. For the *nonequilibrium* system III, examined from 550 to 650 °C, the cathode oxygen partial pressure was fixed at 0.21 atm and the anode H_2 was varied from 0.2 to 1 atm. The combination of Open Circuit Voltage (OCV) measurement and quantitative fitting of the impedance spectra yields electrochemical information at the

two interfaces. The results are consistent with the H_2 electro-oxidation mechanism at the Pt|ceria interface of systems I and II, whereas the resistance to the electro-reduction at the $Ba_{0.5}Sr_{0.5}Co_{0.8}Fe_{0.2}O_{3-\delta}$|ceria is negligible.

Contents

List of Figures

List of Tables

Chapter 1

Introduction

A.C. impedance spectroscopy is a valuable tool for studying both the bulk transport properties of materials and the electrochemical reactions at interfaces. Typically, A.C. impedance experiments are carried out over a wide range of frequencies (several millihertz to several megahertz), and the interpretation of the resulting spectra is aided by analogy to equivalent circuits involving simple components such as resistors and capacitors. In general, such equivalent circuits are not unique, and indeed there exists an infinite set of circuits that can represent any given impedance. It is common to select a physically plausible circuit containing a minimal number of components and, in a somewhat *ad hoc* way, assign physical significance to the derived parameters. Often, meaningful insight into material behavior can be gained from such analyses. However, the *ad hoc* approach is lacking in mathematical and physical rigor, and can lead one to overlook some of the more subtle, but significant, features of the data.

In the present study, a first principle derivation of the equivalent circuit is provided and the analysis then applied to the evaluation of a mixed ionic and electronic conductor (MIEC)—ceria. It is shown that not only can one extract the important electrical parameters of a MIEC, but also, from measurements carried out over wide oxygen partial pressures and at a range of temperatures, essential thermodynamic parameters. The measurements and analysis furthermore provide some indication as to the rate-limiting step for hydrogen electro-oxidation at the metal|ceria interface.

Ceria has been selected for study because of increasing interest in this material as an electrolyte for "reduced" temperature solid oxide fuel cells (SOFCs),[2] that is SOFCs in

which the traditional operating temperature of 800–1000 °C has been reduced to 500–800 °C. Samaria doped ceria (SDC) and gadolinia doped ceria (GDC) exhibit higher conductivity than YSZ at 700 °C, and it has been possible to obtain power densities as high as 1 W/cm^2 from anode-supported SDC fuel cells at 600 °C using humidified hydrogen as the fuel and air as the oxidant.[4] Fuel cell operation in this intermediate temperature regime has the potential for substantially lowering auxiliary component costs and increasing the thermomechanical stability of the SOFC system. The large body of experimental data already existent for acceptor-doped ceria[5] as a consequence of its value for fuel cell applications renders this an ideal model material against which to verify a new measurement approach, whereas the new insight that is to be gained from careful analysis of impedance data into electro-catalytic pathways is of great value to the design of SOFC electrodes.

1.1 Defect Chemistry and Electrical Properties of Acceptor-Doped Ceria

1.1.1 Defect Chemistry

In acceptor-doped ceria, there are three main types of charge carriers—the dopant, the oxygen vacancy and the electron that are created both intrinsically and extrinsically. *Intrinsically*, there is a thermodynamic equilibrium between the lattice oxygen ions and ambient oxygen molecules. Under reducing conditions, ceria tends to lose oxygen to the ambient atmosphere, accompanied by the creation of oxygen vacancies and a change in the cerium oxidation state from 4+ to 3+. In Kröger-Vink notation,[6] this equilibrium can be written as

$$O_O^{\times} \leftrightarrow \frac{1}{2}O_2 + V_O^{\bullet\bullet} + 2Ce'_{Ce}\left(2e'\right) \tag{1.1}$$

where $O_O^{\times}$ represents an oxygen ion residing on a regular oxygen ion site, $V_O^{\bullet\bullet}$ represents an oxygen vacancy, Ce'_{Ce} represents a Ce^{3+} ion residing on a Ce^{4+} site and e' represents an effective electron. *Extrinsically*, the acceptor doping of dopant, *e.g.*, Sm_2O_3, into CeO_2 introduces oxygen vacancies through the doping reaction

$$Sm_2O_3 + 2Ce_{Ce}^{\times} + 4O_O^{\times} \rightarrow 2Sm'_{Ce} + 3O_O^{\times} + V_O^{\bullet\bullet} + 2CeO_2 \tag{1.2}$$

where $Ce_{Ce}^{\times}$ represents a Ce^{4+} ion residing on a Ce^{4+} site and Sm'_{Ce} represents a Sm^{3+} ion residing on a Ce^{4+} site. The dopant, Sm'_{Ce}, oxygen vacancy, $V_O^{\bullet\bullet}$, and electron, e', are denoted as "AD," "ion" and "eon" respectively in the following discussion.

The concentration of oxygen vacancy c_{ion} and the concentration of electron c_{eon} are related by the equilibrium constant, K_r, of reaction (1.1)

$$K_r = c_{ion} c_{eon}^2 p_{O_2}^{1/2} \tag{1.3}$$

where the concentration of $O_O^{\times}$ is taken to be unity. K_r depends on temperature according to

$$K_r = \exp\left(\frac{\Delta S_r}{k_B}\right) \exp\left(-\frac{\Delta H_r}{k_B T}\right) \tag{1.4}$$

where k_B is the Boltzmann constant, T is the absolute temperature, and ΔS_r and ΔH_r are, respectively, the reduction entropy and enthalpy.

Under certain materials and experimental conditions such as heavily doped materials and oxidizing atmospheres, the creation of oxygen vacancy through the reduction reaction (1.1) is negligible compared to the doping reaction (1.2). Thus the oxygen vacancy concentration is mainly dominated by the dopant concentration. That is

$$c_{ion} = c_{AD}/2 \tag{1.5}$$

This is called the constant oxygen vacancy approximation.[7] From (1.3) and (1.5), the electron concentration becomes

$$c_{eon} = \sqrt{\frac{2K_r}{c_{AD}}} p_{O_2}^{-1/4} \tag{1.6}$$

where electron concentration increases with decreasing oxygen partial pressure in a power of $-1/4$.

1.1.2 Electrical Properties

1.1.2.1 Mobilities

At the interested temperature range, the dopant is assumed to be immobile. The oxygen vacancy moves from one to another oxygen sublattice site through a thermally activated process. The mobility of oxygen vacancy u_{ion} is

$$u_{ion} = \frac{u_{ion}^0}{T} \exp\left(-\frac{\Delta H_{ion}}{k_B T}\right) \tag{1.7}$$

where u_{ion}^0 is a constant and ΔH_{ion} is the activation energy for ionic motion.

The electronic charge carrier in ceria is in the form of "small polaron." When the electronic carrier is moving in the polar oxide, it polarizes (by its electric field) the lattice around it. The resulting lattice polarization acts as a potential well that hinders the movements of the charge, thus decreasing its mobility. A polaron consists of the charge carrier and the distortion of the ionic lattice induced by the carrier itself and it is a quasi-particle. When the interaction between the electronic charge carrier and the lattice is relatively weak, the polaron is referred to as a large polaron. Large polarons behave much like free carriers except for an increased mass caused by the fact that polarons carry their associated distortions. When the interaction between the electronic charge carrier and the lattice is strong, the polaron is referred to as a small polaron. The electronic charge carrier is now so slow that it can be imagined to become self-trapped in its own polarization field generated in the ionic lattice, and thus to become localized at a certain lattice site (valence defect). At high temperatures, movement of a small polaron is an activated hopping process similar to that of ionic conduction with the mobility[8]

$$u_{eon} = \frac{u_{eon}^0}{T^\alpha} \exp\left(-\frac{\Delta H_{eon}}{k_B T}\right) \tag{1.8}$$

where u_{eon}^0 is a constant, ΔH_{eon} is the activation energy for electronic motion, α equals 1 for adiabatic hopping and 3/2 for non-adiabatic hopping. In this work, the adiabatic hopping mechanism is used.

1.1.2.2 Conductivities

The conductivity is the product of charge and mobility. The ionic and electronic conductivities are

$$\sigma_{ion} = 2eu_{ion}c_{ion} = eu_{ion}c_{AD} \tag{1.9}$$

$$\sigma_{eon} = eu_{eon}c_{eon} = \sigma^0_{eon}p_{O_2}^{-1/4} \tag{1.10}$$

with

$$\sigma^0_{eon} = eu_{eon}\sqrt{\frac{2K_r}{c_{AD}}} \tag{1.11}$$

The total conductivity, σ_T (the sum of the ionic, σ_{ion}, and electronic, σ_{eon}, conductivities), thus exhibits an oxygen partial pressure dependence given as

$$\sigma_T = \sigma_{ion} + \sigma_{eon} = \sigma_{ion} + \sigma^0_{eon}p_{O_2}^{-1/4} \tag{1.12}$$

In the ionic regime of doped ceria, the total conductivity (essentially equal to the ionic conductivity) is independent of oxygen partial pressure. Under slightly more reducing conditions, the well-known $-1/4$ power law for the dependence of electronic conductivity on oxygen partial pressure is obtained. From a plot of conductivity as a function of oxygen partial pressure one can, by fitting to (1.12), determine the ionic and electronic conductivities over the entire p_{O_2} regime of interest, and such measurements are performed relatively routinely.[3, 9, 10]

Under the conditions of a fixed oxygen vacancy concentration (as considered here), the temperature dependence of the ionic conductivity, (1.9), derives from the temperature dependence of the ionic mobility, (1.7). This gives

$$\sigma_{ion} = \frac{\sigma^0_{ion}}{T}\exp\left(-\frac{\Delta H_{ion}}{k_B T}\right) \tag{1.13}$$

where σ^0_{ion} is a constant. Thus, an Arrhenius plot of the ionic conductivity directly yields ΔH_{ion} from its slope.

For the electronic conductivity, because K_r also depends on temperature via (1.4), the

temperature dependence of σ^0_{eon} is then

$$\sigma^0_{eon} = \frac{\sigma^{00}_{eon}}{T} \exp\left(-\frac{\Delta H^0_{eon}}{k_B T}\right) = \frac{\sigma^{00}_{eon}}{T} \exp\left(-\frac{\Delta H_{eon} + 1/2\Delta H_r}{k_B T}\right) \tag{1.14}$$

where σ^{00}_{eon} is a constant, and σ^0_{eon} exhibits an apparent, or combined, activation energy of $\Delta H^0_{eon} = \Delta H_{eon} + 1/2\Delta H_r$.

1.2 Three Systems

Three specific systems are investigated in this work. From the point view of *materials*, they can be written in the form of $p_{O_2}(a)$|anode|electrolyte|cathode|$p_{O_2}(c)$ where $p_{O_2}(a)$ and $p_{O_2}(c)$ are the oxygen partial pressures in the anode and cathode chambers respectively. The electrolyte is 15% Sm-doped ceria sintered at 1350 and 1550 °C. Specifically, three systems are

I. p_{O_2}|Pt|$Sm_{0.15}Ce_{0.85}O_{1.925-\delta}$ (1350 °C)|Pt|p_{O_2},

II. p_{O_2}|Pt|$Sm_{0.15}Ce_{0.85}O_{1.925-\delta}$ (1550 °C)|Pt|p_{O_2},

III. $p_{O_2}(a)$|Pt|$Sm_{0.15}Ce_{0.85}O_{1.925-\delta}$ (1350 °C)|$Ba_{0.5}Sr_{0.5}Co_{0.8}Fe_{0.2}O_{3-\delta}$|$p_{O_2}(c)$.

For systems I and II, both the anode and cathode are the same, Pt. The systems are also exposed to a uniform atmosphere such that $p_{O_2}(a) = p_{O_2}(c) = p_{O_2}$. Accordingly, there is no charge carrier transport under open circuit and such systems are called equilibrium systems. The only difference between I and II is the electrolyte. As will be shown in the following, the electrolyte sintered at high temperatures such as 1550 °C shows space charge effect at 500–650 °C while the space charge effect is not observable at this temperature range for the electrolyte sintered at the lower temperature 1350 °C. For system III, the anode is also Pt and the cathode is a high-performance material $Ba_{0.5}Sr_{0.5}Co_{0.8}Fe_{0.2}O_{3-\delta}$ (BSCF). There is also an oxygen chemical potential gradient across the system such that $p_{O_2}(a) < p_{O_2}(c)$. Accordingly, there are charge carrier transports even under open circuit and it is called a nonequilibrium system.

From the point view of *microstructure*, all three systems are treated in one dimension for mathematical simplicity. The polycrystalline electrolyte, along the current direction, is

divided into multiple layers of the same width. This is called the serial layer model.[11] The schematic plots of microstructure and concentration profiles are shown in Figure 1.1. In all three systems, the dopant concentration is assumed to the same across the electrolyte. For the system with space charge, system II, every layer is divided into two space charge (SC) regions and one grain interior (GI) region as shown in Figure 1.1(b). In the space charge region, there is depletion of oxygen vacancies and accumulation of electrons. The neighboring two space charge regions constitute the grain boundary (GB). In the grain interior region, both the oxygen vacancy and electron concentrations are constants using the constant oxygen vacancy approximation. For the systems without space charge, systems I and III, the microstructure can be ignored and the whole electrolyte can be treated a single crystal as shown in Figure 1.1(a) and 1.1(c). Again, the constant oxygen vacancy approximation is used. For system I, this gives the constant electron concentration in Figure 1.1(a). For system III, since there is an oxygen potential gradient from the anode to the cathode, $p_{O_2}(a) < p_{O_2}(c)$, there is a gradual decrease of electron concentration according to (1.6) as shown in Figure 1.1(c).

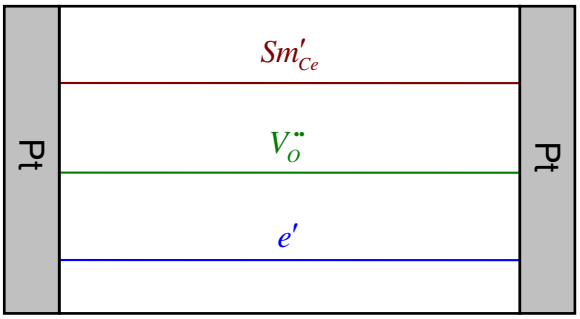

(a)

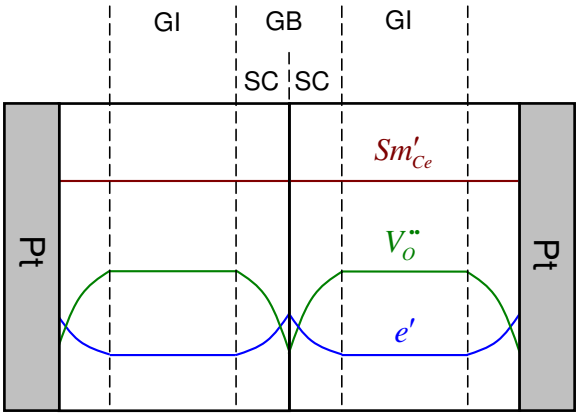

(b)

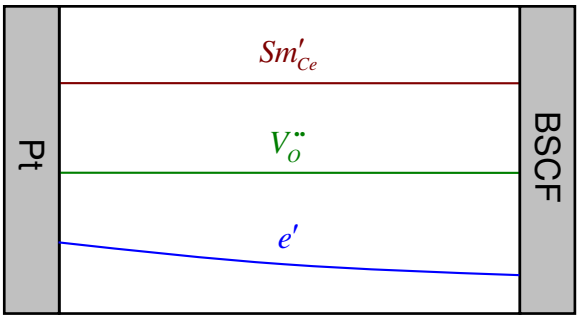

(c)

Figure 1.1: Schematics of carrier concentration profiles of (a) system I, (b) system II and (c) system III.

1.3 Fundamentals of Impedance Spectroscopy

A.C. impedance spectroscopy is a powerful technique for the characterization of electrochemical systems. As shown in Figure 1.2, the fundamental approach of the impedance spectroscopy is to apply a small amplitude sinusoidal current excitation to the system under the steady-state and measure the voltage response. The experiment is carried at a wide range of frequencies. The value of A.C. impedance spectroscopy derives from the effectiveness of the technique in isolating individual reaction/migration steps in a multistep process. That is, because each reaction or migration step has, ideally, a unique time constant associated with it, these steps can be separated in the frequency domain. In recent years, impedance spectroscopy has found widespread applications in the field of characterization of materials. It is routinely used in the characterization of coatings, batteries, fuel cells, *etc.*

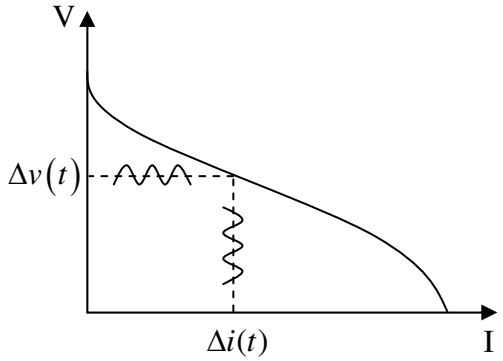

Figure 1.2: Principles of impedance spectroscopy.

1.3.1 System Dynamics

1.3.1.1 Dynamics of Linear System

Generally, a linear system is such that the output function y is related to the input function x by

$$a_0 y(t) + \sum_{i=1}^{n} a_i \frac{d^i y(t)}{dt^i} = b_0 x(t) + \sum_{i=1}^{m} b_i \frac{d^i x(t)}{dt^i},\ n \geq m \tag{1.15}$$

In the steady-state mode, one obtains

$$a_0 y_0 = b_0 x_0 \tag{1.16}$$

For small variations of the input function: $x = x_0 + \Delta x$, the output function can be written as $y = y_0 + \Delta y$ such that

$$a_0 \Delta y(t) + \sum_{i=1}^{n} a_i \frac{d^i \Delta y(t)}{dt^i} = b_0 \Delta x(t) + \sum_{i=1}^{m} b_i \frac{d^i \Delta x(t)}{dt^i} \tag{1.17}$$

The Laplace transform gives

$$\Delta Y(s) \sum_{i=0}^{n} a_i s^i = \Delta X(s) \sum_{i=0}^{m} b_i s^i \tag{1.18}$$

where $\Delta Y(s)$ and $\Delta X(s)$ are the Laplace transforms of $\Delta y(t)$ and $\Delta x(t)$ respectively. Transfer function of the system is defined as

$$H(s) = \frac{\Delta Y(s)}{\Delta X(s)} = \frac{\sum\limits_{i=0}^{m} b_i s^i}{\sum\limits_{i=0}^{n} a_i s^i} \tag{1.19}$$

The factorization of $\sum\limits_{i=0}^{n} a_i s^i = 0$ can be written as

$$\prod_{i=1}^{n} (s - s_i) = 0 \tag{1.20}$$

where s_i are the poles of $H(s)$. The application of partial fraction decomposition to (1.19) gives

$$H(s) = \sum_{i=1}^{n} \frac{d_i}{s - s_i} \tag{1.21}$$

where d_i are constants. Inverse Laplace transform of (1.21) gives

$$h(t) = \sum_{i=1}^{n} d_i e^{s_i t} \tag{1.22}$$

where $h(t)$ is the inverse Laplace transform of $H(s)$. For a stable system, the real part of s_i must be negative. This suggests

$$\lim_{t \to \infty} \sum_{i=1}^{n} d_i e^{s_i t} = 0 \tag{1.23}$$

If the input is an impulse signal $\Delta x(t) = \delta(t)$, $\Delta y(t)$ is called the impulse response. The Laplace transform of the impulse input is

$$\Delta X(s) = 1 \tag{1.24}$$

The Laplace transform of the impulse response is the transfer function

$$\Delta Y(s) = H(s) \tag{1.25}$$

Equation (1.22) and the inverse Laplace transform of (1.25) give

$$\Delta y(t) = h(t) = \sum_{i=1}^{n} d_i e^{s_i t} \tag{1.26}$$

Since $\Delta y(t)$ decays after sufficient time, it is also called the transient response or natural response. It is obvious that the transient response or the natural response in the time domain for the impulse input is due to the poles of $H(s)$.

If the input is a sinusoidal signal $\Delta x(t) = \Delta x_0 \sin(\omega t)$, the Laplace transform of this signal is

$$\Delta X(s) = \Delta x_0 \frac{\omega}{s^2 + \omega^2} \tag{1.27}$$

From (1.18),

$$\Delta Y(s) = \Delta x_0 \frac{\sum_{i=0}^{m} b_i s^i}{\sum_{i=0}^{n} a_i s^i} \frac{\omega}{s^2 + \omega^2} \tag{1.28}$$

This can be written as

$$\Delta Y(s) = \frac{d}{s - j\omega} + \frac{d^*}{s + j\omega} + \sum_{i=1}^{n} \frac{k_i}{s - s_i} \tag{1.29}$$

where s_i again are the poles of $H(s)$, d and d^* are complex conjugates and k_i are some constants. Inverse Laplace transform of (1.29) gives

$$\Delta y(t) = d e^{j\omega t} + d^* e^{-j\omega t} + \sum_{i=1}^{n} d_i e^{s_i t} \tag{1.30}$$

As $t \to \infty$, $\sum_{i=1}^{n} d_i e^{s_i t}$ again vanishes while $de^{-j\omega t} + d^* e^{j\omega t}$ remains. Thus the output response for the sinusoidal input has two components. $\sum_{i=1}^{n} d_i e^{-s_i t}$ is called the transient response or natural response. The expression $de^{-j\omega t} + d^* e^{j\omega t}$ is called the sinusoidal steady-state response $\Delta y_{SSS}(t)$ or forced response. It is obvious that the sinusoidal steady-state response in the time domain is due to the poles of $\Delta X(s)$. The unknown parameter d can be determined from (1.29)

$$d = \lim_{s \to j\omega} \left[(s - j\omega)\, \Delta Y(s) \right] = \lim_{s \to j\omega} \left[(s - j\omega)\, H(s) \frac{\Delta x_0 \omega}{(s - j\omega)\,(s + j\omega)} \right] = \frac{H(j\omega)\Delta x_0}{2j} \tag{1.31}$$

$H(j\omega)$ can be written in the polar coordinates

$$H(j\omega) = |H(j\omega)|\, e^{j\theta(\omega)} \tag{1.32}$$

where $|H(j\omega)|$ is the modulus and $\theta(\omega)$ is the phase angle of $H(j\omega)$. The sinusoidal steady-state response is then

$$\begin{aligned} \Delta y_{SSS}(t) &= de^{-j\omega t} + d^* e^{j\omega t} \\ &= \frac{\Delta x_0}{2} |H(j\omega)|\, e^{j[\omega t + \theta(\omega) - \pi/2]} + \frac{\Delta x_0}{2} |H(j\omega)|\, e^{-j[\omega t + \theta(\omega) - \pi/2]} \\ &= |H(j\omega)|\, \Delta x_0 \sin\left[\omega t + \theta(\omega)\right] \end{aligned} \tag{1.33}$$

Thus for a sinusoidal input the steady-state output is also a sinusoidal signal with the same frequency. The ratio of output and input amplitude is the modulus of $H(j\omega)$ and the phase shift between the output and input is the phase angle of $H(j\omega)$. $H(j\omega)$ is called the frequency response of the transfer function $H(s)$ and it describes the response characteristics of the system at the steady-state subject to sinusoidal inputs. It is given by its evaluation as a function of a complex variable at $s = j\omega$

$$H(j\omega) = \frac{\Delta Y(j\omega)}{\Delta X(j\omega)} \tag{1.34}$$

Experimentally, $H(j\omega)$ is obtained through the Correlation Frequency Response Analysis method.[1] The sinusoidal steady-state response $\Delta y_{SSS}(t)$ to the perturbing signal is

correlated with two synchronous reference signals, one in phase with $x(t)$ and the other 90° out of phase, *i.e.*, $\sin(\omega t)$ and $\cos(\omega t)$ as in Figure 1.3.

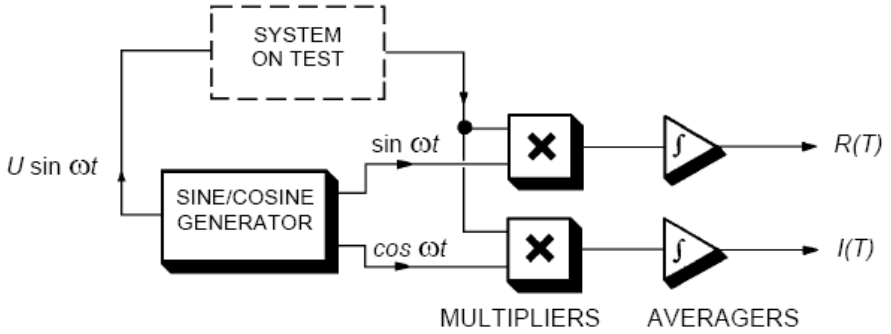

Figure 1.3: Principle of the Correlation Frequency Response Analysis.[1]

The sine and cosine channel outputs are

$$Re(T) = \frac{1}{T}\int_0^T \sin(\omega t)\,\Delta y_{SSS}(t)\,dt = \frac{|H(j\omega)|\,\Delta x_0}{T}\int_0^T \sin(\omega t)\sin[\omega t + \theta(\omega)]\,dt \quad (1.35)$$

$$Im(T) = \frac{1}{T}\int_0^T \cos(\omega t)\,\Delta y_{SSS}(t)\,dt = \frac{|H(j\omega)|\,\Delta x_0}{T}\int_0^T \cos(\omega t)\sin[\omega t + \theta(\omega)]\,dt \quad (1.36)$$

If $T = N\dfrac{2\pi}{\omega}$,

$$Re(N\frac{2\pi}{\omega}) = \frac{|H(j\omega)|\,\Delta x_0}{2}\cos\theta(\omega) \quad (1.37)$$

$$Im(N\frac{2\pi}{\omega}) = \frac{|H(j\omega)|\,\Delta x_0}{2}\sin\theta(\omega) \quad (1.38)$$

From (1.37) and (1.38) both the modulus and phase angle of the frequency response function $H(j\omega)$ can be recovered from the signals $Re(T)$ and $Im(T)$ evaluated at appropriate multiples of $2\pi/\omega$.

1.3.1.2 Dynamics of Nonlinear System

However, in reality few systems are linear, and so we are really measuring some linear approximation. For a nonlinear system, the output function can be expanded around the steady-state solution

$$\Delta y = \left(\frac{dy}{dx}\right)_{x_0,y_0}\Delta x + \frac{1}{2}\left(\frac{d^2y}{dx^2}\right)_{x_0,y_0}(\Delta x)^2 + \ldots \quad (1.39)$$

For a sinusoidal perturbation $\Delta x(t) = \Delta x_0 \sin(\omega t)$, the quadratic terms, containing $\sin^2(\omega t)$ $= [1 - \cos(2\omega t)]/2$, give rise to a second harmonic and a D.C. response. If the magnitude of the perturbing signal Δx_0 is small, then the higher-order terms (including the quadratic terms) in (1.39) can be assumed to be negligible. Thus the nonlinear system under the small perturbation can be approximated to a linear system.

In the context of correlation frequency response, the nonlinear signal $S(t)$ can be expressed as a sum of sine and cosine waves

$$S(t) = |H(j\omega)|\, \Delta x_0 \sin[\omega t + \theta(\omega)] + \sum_{m=2} A_m \sin[m\omega t + \theta_m(\omega)] \tag{1.40}$$

The correlation of this signal to reference sine and cosine waves gives

$$Re(T) = \frac{1}{T}\int_0^T \sin(\omega t)\, S(t) dt \tag{1.41}$$

$$Im(T) = \frac{1}{T}\int_0^T \cos(\omega t)\, S(t) dt \tag{1.42}$$

If $T = N\dfrac{2\pi}{\omega}$,

$$\frac{1}{T}\int_0^T \sin(\omega t) \sum_{m=2} A_m \sin[m\omega t + \theta_m(\omega)] dt = 0 \tag{1.43}$$

$$\frac{1}{T}\int_0^T \cos(\omega t) \sum_{m=2} A_m \sin[m\omega t + \theta_m(\omega)] dt = 0 \tag{1.44}$$

one still obtains

$$Re(N\frac{2\pi}{\omega}) = \frac{|H(j\omega)|\, \Delta x_0}{2} \cos\theta(\omega) \tag{1.45}$$

$$Im(N\frac{2\pi}{\omega}) = \frac{|H(j\omega)|\, \Delta x_0}{2} \sin\theta(\omega) \tag{1.46}$$

Considering harmonics, the only non-zero integral is given by the first harmonic (fundamental); all other harmonics are rejected. By correlating the output of a system with harmonic frequencies 2ω, 3ω, ..., the harmonic components of frequency response are obtainable. These higher-frequency components are useful in computing the exact frequency response.

1.3.2 Complex Impedance and Graphic Representation

If the input is current and the output is voltage, $H(j\omega)$ is called the impedance and denoted as $Z(j\omega)$. If the input is voltage and the output is current, $H(j\omega)$ is called the admittance and denoted as $Y(j\omega) = 1/Z(j\omega)$. In the study of dielectric properties of materials, two other complex functions are more widely used. One of them is the complex permittivity which is related to the complex admittance by

$$\varepsilon(j\omega) = \frac{Y(j\omega)}{j\omega C_0} \tag{1.47}$$

where C_0 is the vacuum capacitance of the material

$$C_0 = \frac{\varepsilon_0 A}{L} \tag{1.48}$$

where ε_0 is the vacuum permittivity, A is the area and L is the thickness of the material. The other one is the complex modulus

$$M(j\omega) = \frac{1}{\varepsilon(j\omega)} \tag{1.49}$$

For the graphic representation of these complex functions, both polar and Cartesian coordinates can be used. Specifically, for the complex impedance $Z(j\omega)$, the plot of modulus $|Z(j\omega)|$ and phase angle $\theta(\omega)$ vs. frequency ω or $f = \omega/2\pi$ is called the Bode-Bode plot. Like other spectroscopic plots, the frequency is explicit. The plot of imaginary part of the impedance, $ImZ(j\omega)$ or $-ImZ(j\omega)$, vs. real part of the impedance, $ReZ(j\omega)$, is called the Nyquist plot. In this case, the frequency is implicit. It is worth mentioning that the plot of $Im\varepsilon(j\omega)$ vs. $Re\varepsilon(j\omega)$ is called the Cole-Cole plot and sometimes in the literature the name is exchangeable with the Nyquist plot. Unless specified, both the Nyquist plot and Bode-Bode plot are called the impedance spectrum.

Figure 1.4 gives an example of the Nyquist plot and Bode-Bode plot for the same impedance function. There appears to be three different processes (I, II, III) in both plots. Three different processes appear as three arcs in the Nyquist plot with the frequency increasing from the right to the left. An analogy can be drawn between one of the Bode-Bode

plot, $|Z|$ vs. f, and the thermogravimetry plot in which weight is plotted against the temperature. There is a corresponding weight loss for every process. A similar analogy can be drawn between the other one of the Bode-Bode plot, θ vs.s f, and the infrared spectrum. There is a corresponding peak for every process.

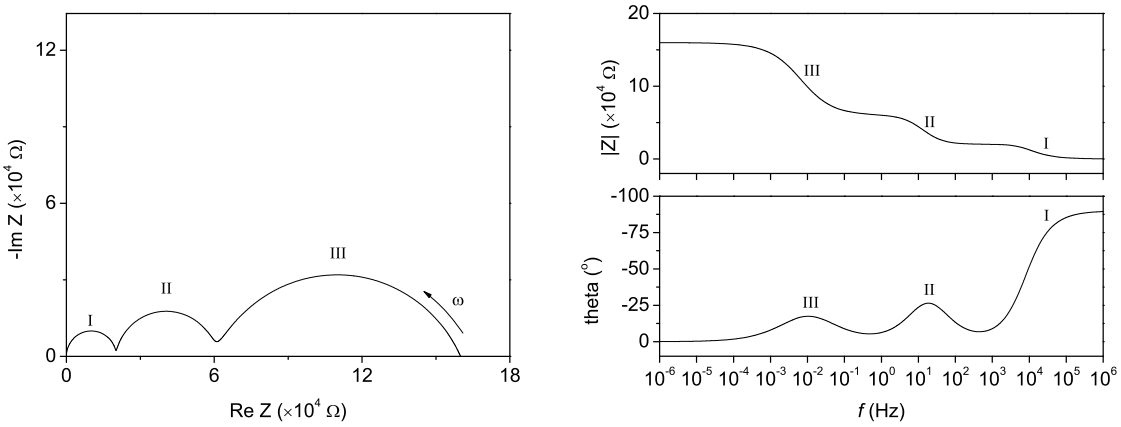

(a) (b)

Figure 1.4: An example (a) the Nyquist and (b) the Bode-Bode plots.

In the study of polycrystalline electroceramics, the three processes are found to be related to the grain interior conduction (I), grain boundary conduction (II) and electrode reaction (III) respectively. This is also the field where the Nyquist plot is more popular than the Bode-Bode plot because from the size of the arc the resistance of the different processes can be easily estimated.

1.3.3 Equivalent Circuits

One of the most attractive aspects of impedance spectroscopy is the direct connection that often exists between the behavior of a real system and that of an idealized model circuit consisting of discrete electrical components. For example, the impedance plot in Figure 1.4 can be fitted using the circuit in Figure 1.5. R is resistor and Q is Constant Phase Element as discussed in the following. This circuit is called the equivalent circuit of the impedance function given in Figure 1.4. Thus it is worth looking at the impedance expression for some common circuit elements.

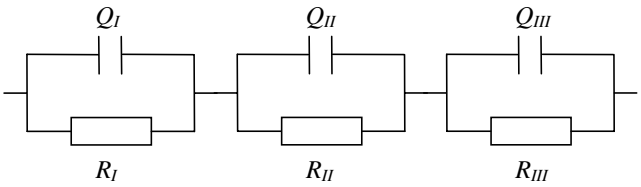

Figure 1.5: One equivalent circuit corresponding to the plots in Figure 1.4.

1.3.3.1 Resistor

The current $\Delta i(t)$ and voltage $\Delta v(t)$ relation for a resistor is

$$\Delta v(t) = R\Delta i(t) \tag{1.50}$$

where R is the resistance. Laplace transform of (1.50) for the sinusoidal input gives

$$\Delta V(j\omega) = R\Delta I(j\omega) \tag{1.51}$$

The impedance for the resistor is thus

$$Z(j\omega) = \frac{\Delta V(j\omega)}{\Delta I(j\omega)} = R \tag{1.52}$$

1.3.3.2 Capacitor

The current $\Delta i(t)$ and voltage $\Delta v(t)$ relation for a capacitor is

$$\Delta i(t) = C\frac{d\Delta v(t)}{dt} \tag{1.53}$$

where C is the capacitance. Laplace transform of (1.53) for the sinusoidal input gives

$$\Delta I(j\omega) = j\omega C\Delta V(j\omega) \tag{1.54}$$

The impedance for the capacitor is thus

$$Z(j\omega) = \frac{\Delta V(j\omega)}{\Delta I(j\omega)} = \frac{1}{j\omega C} \tag{1.55}$$

1.3.3.3 Inductor

The current $\Delta i(t)$ and voltage $\Delta v(t)$ relation for an inductor is

$$\Delta v(t) = L\frac{d\Delta i(t)}{dt} \tag{1.56}$$

Laplace transform of (1.56) for the sinusoidal input gives

$$\Delta V(j\omega) = j\omega L\Delta I(j\omega) \tag{1.57}$$

where L is the inductance. The impedance for the inductor is thus

$$Z(j\omega) = \frac{\Delta V(j\omega)}{\Delta I(j\omega)} = j\omega L \tag{1.58}$$

1.3.3.4 Constant Phase Element

The Constant Phase Element[12] (CPE) is a non-intuitive circuit element that was invented while looking at the response of real-world systems. Mathematically, it is defined as

$$Z(j\omega) = \frac{1}{(j\omega)^{\alpha} C_{\alpha}} \tag{1.59}$$

with two parameters α and C_{α}. It reduces to pure resistor, capacitor and inductor when $\alpha = 0$, $\alpha = 1$ and $\alpha = -1$ respectively. However, in the real application of this element, α is defined between 0 and 1 and this element can be thought of as a fractional generalization of a conventional capacitor.

1.3.3.5 Generalized Finite-Length Warburg Element

Mathematically, the Generalized Finite-Length Warburg Element (GFLW) is the solution to the one-dimensional anomalous diffusion equation subject to the absorbing boundary[13]

$$Z(j\omega) = R_{GFLW}\frac{\tanh\left(j\omega C_{GFLW}\right)^{\alpha_{GFLW}}}{\left(j\omega C_{GFLW}\right)^{\alpha_{GFLW}}} \tag{1.60}$$

with three parameters R_{GFLW}, C_{GFLW} and α_{GFLW}. When $\left(j\omega C_{GFLW}\right)^{\alpha_{GFLW}} \gg 1$, it

reduces to a CPE as in (1.59). When $\alpha_{GFLW} = 0.5$, it reduces to a Finite-Length Warburg (FLW) element[14]

$$Z(j\omega) = R_{FLW} \frac{\tanh \sqrt{j\omega C_{FLW}}}{\sqrt{j\omega C_{FLW}}} \tag{1.61}$$

with two parameters R_{FLW} and C_{FLW}. Again, in the real application of this element, α_{GFLW} is defined between 0 and 0.5. GFLW element gives a half-tear-drop arc called Warburg arc in the Nyquist plot as shown in Figure 1.6. For the FLW element, the slope at the high-frequency part is 45° as in Figure 1.6(a). For the GFLW element, the arc is more depressed and the slope at the high-frequency part is less than 45° as in Figure 1.6(b).

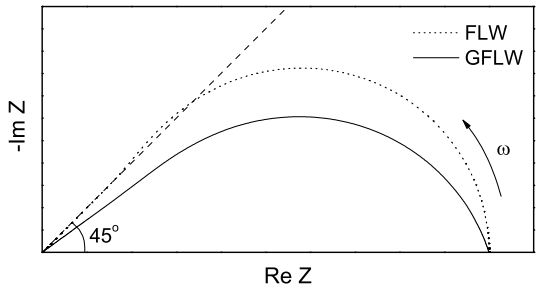

Figure 1.6: Schematic Nyquist plots of a Finite-Length Warburg (FLW) element and a Generalized Finite-Length Warburg (GFLW) element.

1.3.3.6 A Simple Subcircuit—ZARC Element

Series and parallel connections of the above basic elements will produce subcircuits or circuits. One of the most important subcircuits is the parallel connection of a resistor R and a Constant Phase Element Q as one of the three shown in Figure 1.5. This subcircuit is called the ZARC element and labeled as RQ in the circuit code. Thus the circuit in Figure 1.5 is labeled as $R_I Q_I - R_{II} Q_{II} - R_{III} Q_{III}$. The impedance of the ZARC element is

$$\frac{1}{Z\left(j\omega\right)} = \frac{1}{R} + C_\alpha (j\omega)^\alpha \tag{1.62}$$

It can also be written as

$$\left(ReZ - \frac{R}{2}\right)^2 + \left(-ImZ + \frac{R}{2}\cot\frac{\alpha\pi}{2}\right)^2 = \left(\frac{R}{2}\csc\frac{\alpha\pi}{2}\right)^2 \tag{1.63}$$

If $\alpha = 1$, the ZARC element is a parallel connection of a resistor and a capacitor

$$\left(ReZ - \frac{R}{2}\right)^2 + (-ImZ)^2 = \left(\frac{R}{2}\right)^2 \tag{1.64}$$

This gives a perfect semicircle in the Nyquist plot as shown in Figure 1.7. The center of the semicircle is on the real axis. The angular frequency corresponding to highest point in the imaginary axis is called the characteristic frequency ω_0, which can be written as

$$\omega_0 = \frac{1}{RC} \tag{1.65}$$

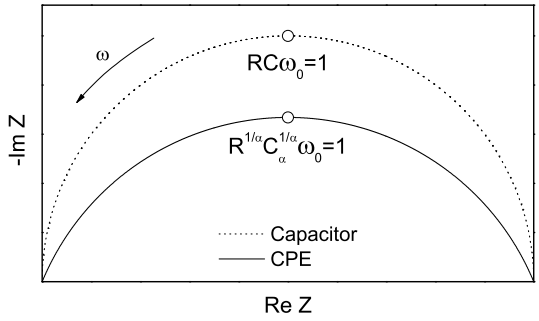

Figure 1.7: Schematic Nyquist plots of the parallel connection of a resistor and a capacitor and a Constant Phase Element.

In the more general case of a ZARC element with a Constant Phase Element, (1.63) gives a depressed arc in the Nyquist plot with the center located below the real axis as also shown in Figure 1.7. The associated characteristic frequency is

$$\omega_0 = \left(\frac{1}{RC_\alpha}\right)^{1/\alpha} \tag{1.66}$$

It is worth noting that C_α does not have the unit of capacitance. The equivalent capacitance of a Constant Phase Element C_{equiv} can be obtained by equating the characteristic frequencies from (1.65) and (1.66)

$$\frac{1}{RC_{equiv}} = \left(\frac{1}{RC_\alpha}\right)^{1/\alpha} \tag{1.67}$$

This gives

$$C_{equiv} = C_{\alpha}^{1/\alpha} R^{1/\alpha - 1} \tag{1.68}$$

The physical concept behind the parallel connection of a resistor and a capacitor to represent a process is that the resistor describes the resistance of the process to the moving charge carriers and the capacitor describes the dielectric response of the process. The resistance is defined as

$$R = \frac{L}{\sigma A} \tag{1.69}$$

where σ is the conductivity, L is the thickness and A is the area of the material. The capacitance is defined as

$$C = \frac{\varepsilon_r \varepsilon_0 A}{L} \tag{1.70}$$

where ε_r is the relative permittivity and ε_0 is the vacuum permittivity. From (1.65), (1.69) and (1.70), one obtains

$$\omega_0 = \frac{1}{RC} = \frac{1}{\frac{L}{\sigma A}\frac{\varepsilon_r \varepsilon_0 A}{L}} = \frac{\sigma}{\varepsilon_r \varepsilon_0} \tag{1.71}$$

It can be seen that ω_0 is a materials constant.

As mentioned above, the parallel connection of a resistor and a capacitor will give a perfect semicircle in the Nyquist plot. However, the perfect semicircles are rarely observed in real measurements. Instead the depressed arcs are often encountered and can be modeled reasonably well by the ZARC element with the Constant Phase Element. The most widely used explanation for the arc depression is the distribution of characteristic frequency. While the variation of relative permittivity ε_r can be safely ignored, the distribution of both carrier concentration and mobility will lead to the distribution of conductivity σ and thus the distribution of ω_0 in (1.71).

1.3.4 Physical Models vs. Empirical Equivalent Circuits

One of the biggest disadvantages of the equivalent circuit method is that equivalent circuits are seldom unique. A simple example would be that the circuit in Figure 1.8 will also give the plots in Figure 1.4.

While the equivalent circuit in Figure 1.5 have some physical roots, sometimes arbitrary

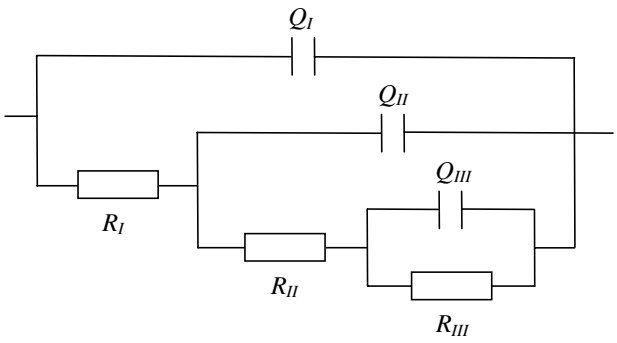

Figure 1.8: Another equivalent circuit corresponding to the plots in Figure 1.4.

equivalent circuits lacking explicit physical explanations are used. On the other hand, if the physical processes in the system are already known, it is possible to directly derive the impedance response of the system under the small-signal perturbation. In the next chapter, it will be shown that the impedance response of the electrolyte can be derived from basic equations describing the charge carrier transport within the electrolyte. It is worth mentioning that an accompanying equivalent circuit can also be constructed for this impedance response and all the circuit elements have explicit physical meanings. It will also be shown in the next chapter that the equivalent circuit in Figure 1.5 is only a rough approximation to a system with only one mobile charge carrier and it is not sufficient to describe a system with more than one mobile charge carrier.

1.3.5 Complex Nonlinear Least-Squares Fitting

The fitting of the model impedance response to the experimental impedance spectrum is performed by the Complex Nonlinear Least-Squares (CNLS) fitting. Consider a model expression $f^{cal}(x; \boldsymbol{P})$ which is a nonlinear function of both x and a set of model parameters $\boldsymbol{P} = (p_1, p_2, \ldots, p_m)$. Consider $i = 1, 2, \ldots, n$ $(n \geq m)$ experimental values $f_i^{exp}(x_i)$. The least-squares procedure involves minimizing the sum of square function

$$S = \sum_{i=1}^{n} w_i \left[f_i^{exp}(x_i) - f_i^{cal}(x_i; \boldsymbol{P}) \right]^2 \tag{1.72}$$

where w_i is the weighting function.

For the CNLS fitting of impedance spectra, the data points are collected at different

frequencies ω_i and the function f is the complex impedance $Z(\omega)$. $Z(\omega)$ is separated into real and imaginary parts and the objective function becomes

$$S = \sum_{i=1}^{n} \left\{ w_i^{Re} \left[ReZ_i^{exp}(\omega_i) - ReZ_i^{cal}(\omega_i; \boldsymbol{P}) \right]^2 + w_i^{Im} \left[ImZ_i^{exp}(\omega_i) - ImZ_i^{cal}(\omega_i; \boldsymbol{P}) \right]^2 \right\} \tag{1.73}$$

where $Z_i^{exp}(\omega_i)$ and $Z_i^{cal}(x; \boldsymbol{P})$ are the experimental and calculated impedance respectively. There are several choices for the weighting function.

1. Unit weighting or no weighting

$$w_i^{Re} = w_i^{Im} = 1 \tag{1.74}$$

   Unit weighting treats each data point equally. This tends to overemphasize data points with a large magnitude.

2. Proportional weighting

$$w_i^{Re} = \frac{1}{(ReZ_i)^2}, \quad w_i^{Im} = \frac{1}{(ImZ_i)^2} \tag{1.75}$$

   At high and low frequencies the imaginary part of the data is very small. This tends to overemphasize data points at high and low frequencies.

3. Modulus weighting

$$w_i^{Re} = \frac{1}{|Z_i|^2}, \quad w_i^{Im} = \frac{1}{|Z_i|^2} \tag{1.76}$$

   Weighting the data by the modulus of impedance is the most recommended weighting strategy and is the default weighting in several kinds of commercial software.

In this work, the weighting function is chosen as the modulus of the calculated impedance, *i.e.*, the function that needs to be minimized is[15]

$$S = \sum_{i=1}^{n} \left\{ \left[\frac{ReZ_i^{exp}(\omega_i) - ReZ_i^{cal}(\omega_i; \boldsymbol{P})}{\left|Z_i^{cal}(\omega_i; \boldsymbol{P})\right|} \right]^2 + \left[\frac{ImZ_i^{exp}(\omega_i) - ImZ_i^{cal}(\omega_i; \boldsymbol{P})}{\left|Z_i^{cal}(\omega_i; \boldsymbol{P})\right|} \right]^2 \right\} \tag{1.77}$$

CNLS starts with initial guesses for the model's parameters $\boldsymbol{P}$. Then one or several parameters in $\boldsymbol{P}$ are changed according to the algorithm. For every set of parameters, the objective function S is calculated. If the change of parameters decreases S, the new parameters are kept. If the change of parameters increase S, the old parameters are kept. The fitting stops when S is below a preset tolerance. Generally, the objective function S has several local minima so a good initial guess is essential. Most of the time this requires some prior basic knowledge of the physical system.

The algorithm used in this work for the CNLS fitting is the Levenberg-Marquardt[16,17] algorithm. It is a standard technique for nonlinear least-squares problems and can be thought of as a combination of steepest descent and the Gauss-Newton method.[18] When the current solution is far from the correct one, the algorithm behaves like a steepest descent method: slow, but guaranteed to converge. When the current solution is close to the correct solution, it becomes a Gauss-Newton method.

Chapter 2

Derivation of Impedance from Physical Models

The derivation of impedance from physical models has its roots in earlier studies by Macdonald *et al.*[19–30] The mapping of physical models to equivalent circuits for the equilibrium (flat-band) conditions was intuitively recongized by Barker[31] and later proved by Brumleve and Buck.[32] Some recent developments include the works of Jamnik and Maier[33,34] and of Moya, Hayas, and Horno.[35] However, so far the discussion of this kind of equivalent circuits has only been limited to equilibrium conditions, namely, constant concentration, zero electric field and charge density, and zero flux. In this work, a rigorous derivation of impedance and equivalent circuits has been presented to include both equilibrium and nonequilibrium conditions.

2.1 Basic Equations

2.1.1 Charge Carrier Transport in the Electrolyte

A set of three fundamental equations govern charge transport in solids. The first is the generalized transport equation that relates the driving force (electrochemical potential) to the mass flux[36]

$$J_i^{mass}(x,t) = -\frac{\sigma_i(x,t)}{(z_i e)^2}\frac{\partial \tilde{\mu}_i(x,t)}{\partial x} \tag{2.1}$$

where x is position and t is time, i is the species of charge carrier, z_i is the number of charges, e is the electron charge, $J_i^{mass}(x,t)$ is the carrier mass flux, $\sigma_i(x,t)$ is the electrical conductivity and $\tilde{\mu}_i(x,t)$ is the electrochemical potential. The electrical conductivity $\sigma_i(x,t)$

of charge carrier i is related to the diffusivity by the Nernst-Einstein relation

$$\sigma_i(x,t) = \frac{(z_i e)^2 D_i}{k_B T} c_i(x,t) \tag{2.2}$$

where D_i is the diffusivity (assumed independent of position and concentration), $c_i(x,t)$ is the carrier concentration, k_B is the Boltzmann constant and T is the absolute temperature. The electrochemical potential $\tilde{\mu}_i(x,t)$ is the sum of the chemical potential $\mu_i(x,t)$ and electrical energy $z_i e\phi(x,t)$

$$\tilde{\mu}_i(x,t) = \mu_i(x,t) + z_i e\phi(x,t) \tag{2.3}$$

For the ideal solution, the chemical potential $\mu_i(x,t)$ is given as

$$\mu_i(x,t) = \mu_i^0 + k_B T \ln \frac{c_i(x,t)}{c_i^0 - c_i(x,t)} \tag{2.4}$$

where μ_i^0 is the standard chemical potential, c_i^0 is the concentration of the total available lattice sites. Here the site exclusion was explicitly taken into account. In the dilute limit, (2.4) becomes

$$\mu_i(x,t) = \mu_i^0 + k_B T \ln \frac{c_i(x,t)}{c_i^0} \tag{2.5}$$

such that the mass flux, (2.1), becomes

$$J_i^{mass}(x,t) = -D_i \frac{\partial c_i(x,t)}{\partial x} - \frac{\sigma_i(x,t)}{z_i e} \frac{\partial \phi(x,t)}{\partial x} = -D_i \frac{\partial c_i(x,t)}{\partial x} - \frac{z_i e D_i c_i(x,t)}{k_B T} \frac{\partial \phi(x,t)}{\partial x} \tag{2.6}$$

Equation (2.6) been given a variety of different names in the literature such as the diffusion-drift, diffusion-migration, Nernst-Planck or electrodiffusion equation. Equation (2.1) can also be rewritten in terms of charge flux and reduced potentials as

$$J_i^{charge}(x,t) = -\sigma_i(x,t) \frac{\partial \tilde{\mu}_i^*(x,t)}{\partial x} \tag{2.7}$$

with

$$J_i^{charge}(x,t) = z_i e J_i^{mass}(x,t) \tag{2.8}$$

$$\tilde{\mu}_i^*(x,t) = \frac{\tilde{\mu}_i(x,t)}{z_i e} = \mu_i^*(x,t) + \phi(x,t) \tag{2.9}$$

$$\mu_i^*(x,t) = \frac{\mu_i(x,t)}{z_i e} \tag{2.10}$$

where $J_i^{charge}(x,t)$ is the carrier charge flux, $\tilde{\mu}_i^*(x,t)$ is the reduced electrochemical potential and $\tilde{\mu}_i^*(x,t)$ is the reduced chemical potential. It is worth noting that both $\mu_i^*(x,t)$ and $\tilde{\mu}_i^*(x,t)$ have units of electrical potential.

The second fundamental equation is describing continuity. In the case where there are no sources or sinks of mass, continuity requires that the variation in mass flux with position balance the variation in concentration with time according to the continuity equation

$$\frac{\partial c_i(x,t)}{\partial t} + \frac{\partial}{\partial x} J_i^{mass}(x,t) = 0 \tag{2.11}$$

In terms of charge flux, this can be written as

$$z_i e \frac{\partial c_i(x,t)}{\partial t} + \frac{\partial}{\partial x} J_i^{charge}(x,t) = 0 \tag{2.12}$$

The third fundamental equation is that due to Poisson, which relates the sum of the charges in the system, $\sum_i z_i e c_i(x,t)$, to the electrical potential according to

$$-\varepsilon_r \varepsilon_0 \frac{\partial^2 \phi(x,t)}{\partial x^2} = \sum_i z_i e c_i(x,t) \tag{2.13}$$

where ε_r is the dielectric constant or relative permittivity and ε_0 is the vacuum permittivity.

2.1.2 Charge Carrier Transport at the Boundaries

In order to solve the above system of equations one requires, in principle, knowledge of the relevant boundary conditions. These can be formulated in terms of the fluxes at the electrolyte|electrode interfaces, which are fixed by the values of the electrochemical potential at the respective interfaces and in the respective gas phase chambers. This type of boundary condition can be written in the most general case as

$$J_i^{charge}(0,t) = g\left[\tilde{\mu}_i^*(a,t), \tilde{\mu}_i^*(0,t)\right] \tag{2.14}$$

$$J_i^{charge}(L,t) = h\left[\tilde{\mu}_i^*(c,t), \tilde{\mu}_i^*(L,t)\right] \tag{2.15}$$

where $\tilde{\mu}_i^*(a,t)$ and $\tilde{\mu}_i^*(c,t)$ are the reduced electrochemical potentials at the electrodes a and c, g and h are functions which embody the characteristics of the electrochemical reactions. The explicit forms of the boundary condition functions, g and h, depend on the details of the electrode reactions including steps such as adsorption, surface diffusion, charge transfer *etc.* Of course, the relevant parameters such as surface coverage, surface diffusivity, charge transfer rate constants *etc.* have to be known. Two forms of these functions have been discussed in the literature. The first is the Butler-Volmer (B-V) type equation, in which a portion of the voltage is taken to drive a concentration gradient and hence the overall rate of reaction.[37] Written in terms of the reduced electrochemical potential for the electrode a, the B-V equation is

$$\begin{aligned} J_i^{charge}(0,t) = {} & J_{i0}(a) \exp\left\{\alpha_i(a)\frac{e\left[\tilde{\mu}_i^*(a,t) - \tilde{\mu}_i^*(0,t)\right]}{k_B T}\right\} \\ & - J_{i0}(a) \exp\left\{-\left[1-\alpha_i(a)\right]\frac{e\left[\tilde{\mu}_i^*(a,t) - \tilde{\mu}_i^*(0,t)\right]}{k_B T}\right\} \end{aligned} \tag{2.16}$$

where $J_{i0}(a)$ is the exchange current density and $\alpha_i(a)$ is the transfer coefficient. When the arguments of the exponential terms are small, the B-V boundary conditions can be approximated as a linear function

$$J_i^{charge}(0,t) = J_{i0}(a) e \frac{\tilde{\mu}_i^*(a,t) - \tilde{\mu}_i^*(0,t)}{k_B T} \tag{2.17}$$

Another possible function for g or h has the form of the Chang-Jaffé (C-J) equation,[21,38] in which the overall rate of reaction is directly proportional to the voltage driving force

$$J_i^{charge}(0,t) = k_i(a)\left[\tilde{\mu}_i^*(a,t) - \tilde{\mu}_i^*(0,t)\right] \tag{2.18}$$

where $k_i(a)$ represents the rate of the electrochemical reaction.

If g and h are linear functions, one can define a charge transfer resistance, $R_i^{\perp}(a)$, which

relates the electrochemical potential drop at the interface to the flux across the interface

$$\tilde{\mu}_i^*(a,t) - \tilde{\mu}_i^*(0,t) = J_i^{charge}(0,t) A R_i^{\perp}(a) \tag{2.19}$$

For the linearized B-V boundary condition, the charge transfer resistance is simply

$$R_i^{\perp}(a) = \frac{k_B T}{e J_{i0}(a) A} \tag{2.20}$$

whereas for the C-J boundary condition it is

$$R_i^{\perp}(a) = \frac{1}{k_i(a) A} \tag{2.21}$$

2.2 Steady-State Solution under Open Circuit Conditions

2.2.1 Steady-State Solution in the Electrolyte

For the steady-state solution, the time dependence in the three fundamental equations (2.7), (2.12) and (2.13) can be dropped. From (2.12)

$$\frac{d}{dx} J_i^{charge}(x) = 0 \tag{2.22}$$

This implies the charge flux is constant J_i^{charge}. Thus from (2.6)–(2.8)

$$J_i^{charge} = -\sigma_i(x) \frac{d\tilde{\mu}_i^*(x)}{dx} = -z_i e D_i \frac{dc_i(x)}{dx} - \frac{(z_i e)^2 D_i c_i(x)}{k_B T} \frac{d\phi(x)}{dx} \tag{2.23}$$

If $J_i^{charge} = 0$, it is called the steady-state *equilibrium* condition. If $J_i^{charge} \neq 0$, it is called the steady-state *nonequilibrium* condition. From (2.13), if there is no time dependence

$$-\varepsilon_r \varepsilon_0 \frac{d^2\phi(x)}{dx^2} = -\sum_i z_i e c_i(x) \tag{2.24}$$

Finally, in the absence of an external applied electric potential gradient, *i.e.*, under open circuit conditions, the charge fluxes of all the carriers are balanced so as to produce no net charge flow. That is

$$\sum_i J_i^{charge} = 0 \tag{2.25}$$

which provides an additional constraint on the system.

The above set of equations (2.23)–(2.25) are coupled nonlinear differential equations for which only numerical solutions are typically available. However, some approximate methods can be used to simplify the solution process. Two widely used approximations are the constant-field approximation and electroneutrality approximation, both of which rely on the fact that the terms in equation (2.24) are small.[39,40] The *constant-field* approximation results when the left-side term in equation (2.24) is assumed to be zero, but the right side remains non-zero

$$-\varepsilon_r\varepsilon_0\frac{d^2\phi(x)}{dx^2} = 0, \sum_i z_i e c_i(x) \neq 0 \tag{2.26}$$

This implies

$$\frac{d\phi(x)}{dx} = -E \tag{2.27}$$

in which E is the electric field and a constant. In the field of biological system, it is usually called the Goldman constant field approximation.[41] The *electroneutrality* approximation results when the right term in equation (2.24) is assumed to be zero, but the left side remains non-zero, the result is simply

$$\sum_i z_i e c_i(x) = 0, \quad -\varepsilon_r\varepsilon_0\frac{d^2\phi(x)}{dx^2} \neq 0 \tag{2.28}$$

This is called the electroneutrality approximation since the total charge at any position is zero. This approximation has been employed in the work of Tannhauser[42] and Liu.[43] There have been some investigations in the literature as to determine which approximation works better under different conditions.[40,44]

For the MIEC ceria, three charge carriers are the mobile oxygen vacancy, mobile electron and immobile acceptor dopant, from (2.23)–(2.25)

$$J_{ion}^{charge} = -\sigma_{ion}(x)\frac{d\tilde{\mu}_{ion}^*(x)}{dx} = -z_{ion}eD_{ion}\frac{dc_{ion}(x)}{dx} - \frac{(z_{ion}e)^2 D_{ion}c_{ion}(x)}{k_BT}\frac{d\phi(x)}{dx} \tag{2.29}$$

$$J_{eon}^{charge} = -\sigma_{eon}(x)\frac{d\tilde{\mu}_{eon}^*(x)}{dx} = -z_{eon}eD_{eon}\frac{dc_{eon}(x)}{dx} - \frac{(z_{eon}e)^2 D_{eon}c_{eon}(x)}{k_BT}\frac{d\phi(x)}{dx} \tag{2.30}$$

$$-\varepsilon_r\varepsilon_0\frac{d^2\phi(x)}{dx^2} = z_{ion}ec_{ion}(x) + z_{eon}ec_{eon}(x) + z_{AD}ec_{AD} \tag{2.31}$$

$$J_{ion}^{charge} + J_{eon}^{charge} = 0 \tag{2.32}$$

As discussed in Chapter 1, an additional constraint is the local equilibrium

$$O_O^{\times} \leftrightarrow \frac{1}{2}O_2 + V_O^{\bullet\bullet} + 2e' \tag{2.33}$$

with the equilibrium constant

$$K_r = c_{ion}(x)c_{eon}^2(x)p_{O_2}^{1/2}(x) \tag{2.34}$$

Again, the solution of coupled differential equations (2.29)–(2.32) and (2.34) requires some approximation methods. In this work, the constant oxygen vacancy approximation is used.

2.2.1.1 System III. Nonequilibrium Conditions without Space Charge

For the investigated system, the oxygen vacancy concentration is mainly dominated by the acceptor doping while the creation of oxygen vacancy by the reduction reaction is negligible. This is called the constant oxygen vacancy approximation.[7] That is

$$c_{ion}(x) = c_{ion} = c_{AD}/2 \tag{2.35}$$

In the context of constant-field and electroneutrality approximations mentioned above, it is important to recognize that the constant-field approximation is implicitly included in the constant oxygen vacancy approximation because from (2.29) and (2.35)

$$\frac{d\phi}{dx} = -\frac{J_{ion}^{charge}}{\sigma_{ion}} = -E \tag{2.36}$$

with the Nernst-Einstein relation from (2.2)

$$\sigma_{ion} = \frac{(z_{ion}e)^2 D_{ion}}{k_B T}c_{ion} \tag{2.37}$$

The concentration of the electron can be evaluated by taking the derivative of the drift-diffusion equation (2.30) with respect to position

$$0 = -\frac{d^2 c_{eon}(x)}{dx^2} - \frac{z_{eon} e}{k_B T} \frac{dc_{eon}(x)}{dx} \frac{d\phi(x)}{dx} - \frac{z_{eon} e}{k_B T} c_{eon}(x) \frac{d^2\phi(x)}{dx^2} \tag{2.38}$$

For the constant-field approximation (2.36), (2.38) becomes

$$0 = \frac{d^2 c_{eon}(x)}{dx^2} - \frac{z_{eon} e E}{k_B T} \frac{dc_{eon}(x)}{dx} \tag{2.39}$$

The solution of (2.39) gives the electron concentration profile

$$c_{eon}(x) = c_{eon}(0) - [c_{eon}(0) - c_{eon}(L)] \frac{1 - \exp\left(\frac{z_{eon} e E}{k_B T} x\right)}{1 - \exp\left(\frac{z_{eon} E}{k_B T} L\right)} \tag{2.40}$$

with the boundary values obtained from the local equilibrium

$$c_{eon}(0) = \sqrt{\frac{K_r}{c_{ion}}} p_{O_2}^{-1/4}(0) \tag{2.41}$$

$$c_{eon}(L) = \sqrt{\frac{K_r}{c_{ion}}} p_{O_2}^{-1/4}(L) \tag{2.42}$$

Inserting (2.40) into (2.30), and making use of the constant-field approximation, (2.36), yields the electron flux

$$J_{eon}^{charge} = \frac{\sigma_{eon}(L) - \sigma_{eon}(0) \exp\left(-\frac{eE}{k_B T} L\right)}{1 - \exp\left(-\frac{eE}{k_B T} L\right)} E \tag{2.43}$$

with

$$\sigma_{eon}(0) = \sigma_{eon}^0 p_{O_2}^{-1/4}(0) \tag{2.44}$$

$$\sigma_{eon}(L) = \sigma_{eon}^0 p_{O_2}^{-1/4}(L) \tag{2.45}$$

$$\sigma_{eon}^0 = \frac{D_{eon} e^2}{k_B T} \sqrt{\frac{K_r}{c_{ion}}} \tag{2.46}$$

Using the fact that the electron and ionic charge fluxes are exactly balanced under steady-state conditions, (2.32), and combining this with the solution to the electric field under the constant vacancy approximation, (2.36), one obtains the electric field

$$E = -\frac{k_B T}{eL} \ln \frac{\sigma_{ion} + \sigma^0_{eon} p_{O_2}^{-1/4}(L)}{\sigma_{ion} + \sigma^0_{eon} p_{O_2}^{-1/4}(0)} = -\frac{\phi(L) - \phi(0)}{L} \tag{2.47}$$

Thus, under the constant vacancy approximation, one needs only to know the value of the oxygen partial pressures at the MIEC|electrode interfaces, $p_{O_2}(0)$ and $p_{O_2}(L)$ and one can immediately evaluate electron concentration profile (2.40) from (2.41), (2.42) and (2.47). The concentration profiles are schematically drawn in Figure 1.1(c). From the local equilibrium, the oxygen partial pressure profile is then simply

$$p_{O_2}(x) = \left[\frac{K_r}{c_{ion} c^2_{eon}(x)}\right]^2 \tag{2.48}$$

2.2.1.2 System II. Equilibrium Conditions with Space Charge

At the steady-state equilibrium condition, $J_{ion}^{charge} = J_{eon}^{charge} = 0$. Equations (2.29) and (2.30) become

$$\frac{d\tilde{\mu}^*_{ion}(x)}{dx} = 0 \tag{2.49}$$

$$\frac{d\tilde{\mu}^*_{eon}(x)}{dx} = 0 \tag{2.50}$$

From the definition of the reduced electrochemical potential (2.5) and (2.9)

$$\frac{d \ln c_i(x)}{dx} = -\frac{z_i e}{k_B T} \frac{d\phi(x)}{dx} \tag{2.51}$$

Defining c_i^∞ as the concentration at the reference point ∞ where $\phi = 0$, integrating (2.51) from the reference point to x yields

$$c_{ion}(x) = c^\infty_{ion} \exp\left[-\frac{z_{ion} e \phi(x)}{k_B T}\right] \tag{2.52}$$

$$c_{eon}(x) = c^\infty_{eon} \exp\left[\frac{-z_{eon} \phi(x)}{k_B T}\right] \tag{2.53}$$

This is the Boltzmann distribution. At the reference point $\phi = 0$, from (2.24)

$$z_{ion} e c_{ion}^{\infty} + z_{eon} e c_{eon}^{\infty} + z_{AD} e c_{AD} = 0 \tag{2.54}$$

This is the electroneutrality condition. At the reference point, from the local equiblibrium

$$K_r = c_{ion}^{\infty} \left(c_{eon}^{\infty}\right)^2 \left(p_{O_2}^{\infty}\right)^{1/2} \tag{2.55}$$

As discussed above, the solution of coupled nonlinear differential equations (2.52)–(2.55) require some approximations to be made.

In the *grain interior* region, the potential is assumed to be zero, *i.e.*, the reference point is assumed to be situated in the whole grain interior region. Actually, the numerical solution suggests that at distances several Debye length away from the interface, the potential can be approximated to be zero.[45] Thus the oxygen partial pressure $p_{O_2}^{\infty}$ is the experimental oxygen partial pressure p_{O_2}. The concentrations of charge carriers are given by the solution of (2.54) and (2.55). Of course it is possible to directly solve (2.54) and (2.55) to obtain the ionic c_{ion}^{∞} and electronic concentrations c_{eon}^{∞}. However, for the interested material and experimental conditions, further simplification is applicable. Again, under the constant oxygen vacancy approximation, (2.54) and (2.55) become

$$c_{ion}^{\infty} = c_{AD}/2 \tag{2.56}$$

$$c_{eon}^{\infty} = \sqrt{\frac{2K_r}{c_{AD}}} p_{O_2}^{-1/4} \tag{2.57}$$

In the *space charge* region, the concentrations of ions and electrons are assumed to be negligible compared with the concentration of the dopants, $c_{ion}(x), c_{eon}(x) \ll c_{AD}$, thus (2.24) becomes

$$-\varepsilon_r \varepsilon_0 \frac{d^2\phi(x)}{dx^2} = -e c_{AD} \tag{2.58}$$

If the boundary conditions are chosen as

$$\phi(x = 0) = \phi_0 \tag{2.59}$$

$$\phi(x = \lambda_S) = \left.\frac{d\phi}{dx}\right|_{x=\lambda_S} = 0 \tag{2.60}$$

where λ_S is the arbitrary space charge layer width, the solution of (2.58) gives the approximate solution

$$\phi(x) = \phi_0 \left(1 - \frac{x}{\lambda_S}\right)^2 \tag{2.61}$$

with

$$\lambda_S = \sqrt{\frac{2\varepsilon_r \varepsilon_0 \phi_0}{e c_{AD}}} \tag{2.62}$$

This is called the Mott-Schottky profile.[46–48] From (2.52) and (2.53) the carrier concentrations in the space charge region are

$$c_{ion}(x) = c_{ion}^{\infty} \exp\left[-\frac{2e\phi_0}{k_B T}\left(1 - \frac{x}{\lambda_S}\right)^2\right] \tag{2.63}$$

$$c_{eon}(x) = c_{eon}^{\infty} \exp\left[\frac{e\phi_0}{k_B T}\left(1 - \frac{x}{\lambda_S}\right)^2\right] \tag{2.64}$$

Equations (2.56), (2.57), (2.63) and (2.64) give the complete description of the steady-state carrier concentrations in both the space charge and grain interior regions within a grain. In one-dimension condition, this is the solution within one serial layer. The solution will be repeated for N numbers of serial layers. The concentration profiles are schematically drawn in Figure 1.1(b).

2.2.1.3 System I. Equilibrium Conditions without Space Charge

If there is no space charge effect

$$\frac{d\phi(x)}{dx} = 0 \tag{2.65}$$

From (2.51) and (2.65), this means that the carrier concentration is constant

$$c_i(x) = c_i \tag{2.66}$$

Now the whole grain is assumed to be the reference. As in (2.56) and (2.57), similarly, the ionic and electronic concentrations are given by

$$c_{ion} = c_{AD}/2 \tag{2.67}$$

$$c_{eon} = \sqrt{\frac{2K_r}{c_{AD}}} p_{O_2}^{-1/4} \tag{2.68}$$

The concentration profiles are schematically drawn in Figure 1.1(a).

2.2.2 Steady-State Solution at the Boundaries

A complete description of the electrode|MIEC|electrode system requires application of the boundary conditions discussed in section 2.1.2. While the flux through the system is a constant under steady-state conditions, the voltage will be influenced by the electrochemical activity of the electrodes. The macroscopically measured voltage generated between the anode and cathode chambers is given as

$$V_{ca} = V_c - V_a = \tilde{\mu}^*_{eon}(c) - \tilde{\mu}^*_{eon}(a) \tag{2.69}$$

Under the assumption of local equilibrium for reaction (2.33), the electrochemical potentials of the species in the electrodes chambers are related according to

$$\frac{1}{4e}\mu_{O_2}(a) + \tilde{\mu}^*_{ion}(a) - \tilde{\mu}^*_{eon}(a) = 0 \tag{2.70}$$

$$\frac{1}{4e}\mu_{O_2}(c) + \tilde{\mu}^*_{ion}(c) - \tilde{\mu}^*_{eon}(c) = 0 \tag{2.71}$$

Inserting the expressions implied by these relationships into (2.69) yields

$$V_{ca} = \frac{1}{4e}\mu_{O_2}(c) - \frac{1}{4e}\mu_{O_2}(a) + \tilde{\mu}^*_{ion}(c) - \tilde{\mu}^*_{ion}(a) \tag{2.72}$$

The difference between the first two terms in (2.72) is readily recognized as the Nernst potential, V_N, of the system

$$V_N = \frac{1}{4e}\left[\mu_{O_2}(c) - \mu_{O_2}(a)\right] = \frac{k_B T}{4e} \ln \frac{p_{O_2}(c)}{p_{O_2}(a)} \tag{2.73}$$

The final two terms can be evaluated by reference to the charge transfer resistance, as defined in (2.19). That definition implies

$$\tilde{\mu}^*_{ion}(a) - \tilde{\mu}^*_{ion}(0) = J^{charge}_{ion} A R^{\perp}_{ion}(a) \tag{2.74}$$

$$\tilde{\mu}^*_{ion}(L) - \tilde{\mu}^*_{ion}(c) = J^{charge}_{ion} A R^{\perp}_{ion}(c) \tag{2.75}$$

and thus (2.72) becomes

$$V_{oc} = V_N + \tilde{\mu}^*_{ion}(L) - \tilde{\mu}^*_{ion}(0) - J^{charge}_{ion} A \left[R^{\perp}_{ion}(a) + R^{\perp}_{ion}(c) \right] \tag{2.76}$$

The quantity $\tilde{\mu}^*_{ion}(L) - \tilde{\mu}^*_{ion}(0)$ in this expression can be obtained by integration of (2.29) and is given as

$$\tilde{\mu}^*_{ion}(L) - \tilde{\mu}^*_{ion}(0) = -J^{charge}_{ion} A R_{ion} \tag{2.77}$$

with

$$R_{ion} = \int_0^L \frac{dx}{\sigma_{ion}(x) A} \tag{2.78}$$

where R_{ion} is defined as the total ionic resistance of the electrolyte. Thus, the externally measured voltage is

$$V_{ca} = V_N - J^{charge}_{ion} A \left[R^{\perp}_{ion}(a) + R_{ion} + R^{\perp}_{ion}(c) \right] \tag{2.79}$$

This voltage depends not only on the oxygen partial pressures at the electrodes (which establish V_N), but also on the ionic resistivity of the electrolyte and the electrochemical activity of the electrodes.

The voltage can also be alternatively expressed in terms of the electronic properties of the MIEC, if again, appropriate boundary conditions are applied. If the electrodes are taken to be reversible with respect to electrons, such that the variation in electrochemical potential of electrons throughout each electrode and across each electrode|electrolyte interface is assumed to be negligible, then

$$\tilde{\mu}^*_{eon}(a) = \tilde{\mu}^*_{eon}(0) \tag{2.80}$$

$$\tilde{\mu}^*_{eon}(c) = \tilde{\mu}^*_{eon}(L) \tag{2.81}$$

Insertion into (2.69) simply yields

$$V_{ca} = \tilde{\mu}^*_{eon}(L) - \tilde{\mu}^*_{eon}(0) \tag{2.82}$$

which can be evaluated by integration of (2.30) to obtain

$$\tilde{\mu}^*_{eon}(L) - \tilde{\mu}^*_{eon}(0) = -J^{charge}_{eon} A R_{eon} = V_{ca} \tag{2.83}$$

with

$$R_{eon} = \int_0^L \frac{dx}{\sigma_{eon}(x) A} \tag{2.84}$$

where R_{eon} is defined as the total electronic resistance of the electrolyte. This treatment takes the voltage drop across the electrodes to be zero (implied in the statement that there is no change in the electrochemical potential of the electrons). However, there is a change in oxygen chemical potential (and hence virtual oxygen partial pressure gradient) across the electrodes as a consequence of non-ideal kinetics for the ionic reactions. The situation is shown schematically in Figure 2.1. The characteristics of the electrodes thus establish the total electronic conductivity of the MIEC by fixing the oxygen partial pressures at $x = 0$ and L, which, in turn, fix the values of the electronic conductivity at the integration limits of (2.84).

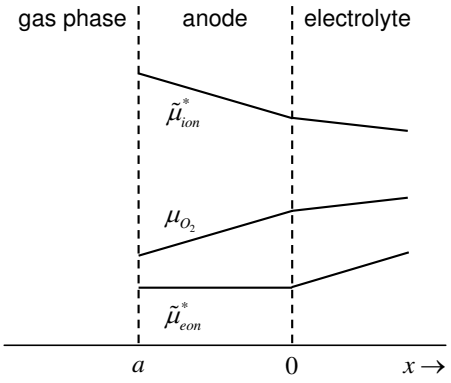

Figure 2.1: Schematic illustration of the chemical potential changes occurring at an electrode|electrolyte interface, shown for the particular case of the anode, under the assumption of an electron reversible electrode.

Physically, the oxygen chemical potential change across the electrodes must be related to the atomistic terms describing the boundary conditions. The electron reversibility of the electrodes implies from (2.70)

$$\frac{1}{4e}\mu_{O_2}(a) + \tilde{\mu}^*_{ion}(a) - \tilde{\mu}^*_{eon}(0) = 0 \tag{2.85}$$

Simultaneously, local chemical equilibrium at the anode|electrolyte interface implies

$$\frac{1}{4e}\mu_{O_2}(0) + \tilde{\mu}^*_{ion}(0) - \tilde{\mu}^*_{eon}(0) = 0 \tag{2.86}$$

Taking the difference yields

$$\frac{1}{4e}\left[\mu_{O_2}(a) - \mu_{O_2}(0)\right] + \tilde{\mu}^*_{ion}(a) - \tilde{\mu}^*_{ion}(0) = 0 \tag{2.87}$$

Defining $\Delta\mu_{O_2}(a)$ as the difference in oxygen chemical potential in the anode gas chamber and that at the electrolyte interface, and making use of (2.74) gives

$$\Delta\mu_{O_2}(a) = -4eJ^{charge}_{ion}AR^{\perp}_{ion}(a) \tag{2.88}$$

Inserting the expressions for the charge transfer resistance obtained from the B-V and the C-J boundary conditions, (2.20) and (2.21), respectively, yields

$$\Delta\mu_{O_2}(a) = -4k_BT\frac{J^{charge}_{ion}}{J_{ion,0}(a)} \tag{2.89}$$

and

$$\Delta\mu_{O_2}(a) = \frac{-4e}{k_{ion}(a)}J^{charge}_{ion} \tag{2.90}$$

The change in partial pressure across the electrodes, furthermore, contribute, along with the electronic leakage, to the reduction of the cell voltage below the Nernstian value. As discussed above, the measured cell voltage can be expressed as (2.79) and (2.83) from the ionic and electronic properties of the system. At open circuit conditions, given the relationship between J^{charge}_{ion} and J^{charge}_{eon}, (2.32), the measured open circuit voltage V_{oc} can be expressed as

$$V_{oc} = \frac{R_{eon}}{R_{eon} + R^{\perp}_{ion}(a) + R_{ion} + R^{\perp}_{ion}(c)}V_N \tag{2.91}$$

In the case of ideally active electrodes, in which the oxygen partial pressures at the $x = 0$

and $x = L$ matches precisely the respective values in the anode and cathode chambers, the open circuit voltage the theoretical maximum voltage across the mixed conductor, V_{oc}^{th}, is obtained. Setting the charge transfer resistors to be zero in (2.91) yields

$$V_{oc}^{th} = \frac{R_{eon}}{R_{eon} + R_{ion}} V_N \tag{2.92}$$

A noteworthy consequence of these relationships is that it is not possible to directly evaluate the mean ionic transference number of a mixed conductor from a simple measurement of the voltage at open circuit unless care is taken to develop ion reversible electrodes (which is not the case for the typical experiment). That is, in general, $\langle t_{ion} \rangle \neq V_{oc}/V_N$, a result which has received some attention in the recent literature.

As discussed above, if the electrodes are taken to be reversible with respect to electrons, the voltage is determined by the difference in reduced electrochemical potential of the electronic species

$$V_{oc} = \tilde{\mu}_{eon}^{*}(L) - \tilde{\mu}_{eon}^{*}(0) \tag{2.93}$$

Rewriting (2.93) in terms of the chemical and electrical potentials, (2.9)–(2.5), yields

$$V_{oc} = \frac{k_B T}{z_{eon} e} \ln \frac{c_{eon}(L)}{c_{eon}(0)} + \phi(L) - \phi(0) \tag{2.94}$$

Upon insertion of the oxygen partial pressure dependence of $c_{eon}(0)$ and $c_{eon}(L)$, (2.41) and (2.42), and the value of the electric field, (2.47), the voltage becomes

$$V_{oc} = \frac{k_B T}{e} \ln \frac{\sigma_{eon}^{0} + \sigma_{ion} p_{O_2}^{1/4}(L)}{\sigma_{eon}^{0} + \sigma_{ion} p_{O_2}^{1/4}(0)} \tag{2.95}$$

The open circuit voltage V_{oc} is generally an experimentally measurable parameter. Thus to continue the above discussion in section 2.2.1.1, if either one of $p_{O_2}(0)$ or $p_{O_2}(L)$ is known, the electron concentration profile can be obtained using (2.40), (2.41), (2.42), (2.47) and (2.95).

2.3 Small-Signal Impedance Solution

2.3.1 Small-Signal Solution in the Electrolyte

If a small perturbation is applied to a system otherwise described by the above steady-state conditions, the system will evolve with time. The small perturbation can be the impulse signal or the sinusoidal signal, *etc.* For sufficiently small perturbations, all quantities can be written as the sum of their steady-state values and time dependent perturbations to those values

$$\begin{aligned}
\phi(x,t) &= \phi(x) + \Delta\phi(x,t) \\
c_i(x,t) &= c_i(x) + \Delta c_i(x,t) \\
\sigma_i(x,t) &= \sigma_i(x) + \Delta\sigma_i(x,t) \\
\tilde{\mu}_i^*(x,t) &= \tilde{\mu}_i^*(x) + \Delta\tilde{\mu}_i^*(x,t) \\
J_i^{charge}(x,t) &= J_i^{charge} + \Delta J_i^{charge}(x,t)
\end{aligned} \tag{2.96}$$

Plugging (2.96) into (2.7), (2.12) and (2.13) and employing the steady-state solution (2.23) and (2.24) while ignoring the second-order term $\Delta\sigma_i(x,t)\Delta\tilde{\mu}_i^*(x,t)$

$$\Delta J_i^{charge}(x,t) = -\sigma_i(x)\frac{\partial\Delta\tilde{\mu}_i^*(x,t)}{\partial x} - \Delta\sigma_i(x,t)\frac{d\tilde{\mu}_i^*(x)}{dx} \tag{2.97}$$

$$\frac{\partial\Delta J_i^{charge}(x,t)}{\partial x} = -z_i e\frac{\partial\Delta c_i(x,t)}{\partial t} \tag{2.98}$$

$$-\varepsilon_r\varepsilon_0\frac{\partial^2\Delta\phi(x,t)}{\partial x^2} = \sum_i z_i e\Delta c_i(x,t) \tag{2.99}$$

For the dilute solution, from (2.5)

$$\Delta c_i(x,t) = c_i(x)\left[\frac{c_i(x,t)}{c_i(x)} - 1\right] = c_i(x)\left\{\exp\left[\frac{\Delta\mu_i(x,t)}{k_BT}\right] - 1\right\} \tag{2.100}$$

For the small signal, the second order term $\Delta\mu_i(x,t)\Delta\mu_i(x,t)$ can be ignored

$$\exp\left[\frac{\Delta\mu_i(x,t)}{k_BT}\right] \approx 1 + \frac{\Delta\mu_i(x,t)}{k_BT} \tag{2.101}$$

Thus (2.100) becomes

$$\Delta c_i(x,t) = c_i(x)\frac{\Delta\mu_i(x,t)}{k_BT} \tag{2.102}$$

From (2.102), (2.98) can be written as

$$\frac{z_i e c_i(x)}{k_BT}\frac{\partial\Delta\mu_i(x,t)}{\partial t} = -\frac{\partial\Delta J_i^{charge}(x,t)}{\partial x} \tag{2.103}$$

From (2.2) and (2.102)

$$\Delta\sigma_i(x,t) = \sigma_i(x)\frac{\Delta\mu_i(x,t)}{k_BT} \tag{2.104}$$

From (2.23) and (2.104), (2.97) can be written as

$$\Delta J_i^{charge}(x,t) = -\sigma_i(x)\frac{\partial\Delta\tilde{\mu}_i^*(x,t)}{\partial x} + z_i e J_i^{charge}\frac{\Delta\mu_i^*(x,t)}{k_BT} \tag{2.105}$$

As (2.98) is true for any particular species, it must also be true for the sum of all species such that

$$\sum_i \frac{\partial\Delta J_i^{charge}(x,t)}{\partial x} = -\sum_i z_i e\frac{\partial\Delta c_i(x,t)}{\partial t} \tag{2.106}$$

Insertion of (2.99) yields

$$\frac{\partial}{\partial x}\left[\sum_i \Delta J_i^{charge}(x,t) - \varepsilon_r\varepsilon_0\frac{\partial}{\partial t}\frac{\partial\Delta\phi(x,t)}{\partial x}\right] = 0 \tag{2.107}$$

which implies the total charge flux $\Delta J_T^{charge}(t)$ is

$$\Delta J_T^{charge}(t) = \sum_i \Delta J_i^{charge}(x,t) + \Delta J_{dis}^{charge}(x,t) \tag{2.108}$$

with

$$\Delta J_{dis}^{charge}(x,t) = -\varepsilon_r\varepsilon_0\frac{\partial}{\partial x}\frac{\partial}{\partial t}\Delta\phi(x,t) \tag{2.109}$$

where $\Delta J_{dis}^{charge}(x,t)$ is the displacement current.

The Laplace transform of (2.103), (2.105), (2.108) and (2.109) for the sinusoidal signal gives

$$\Delta J_i^{charge}(x,\omega) = -\sigma_i(x)\frac{\partial \Delta\tilde{\mu}_i^*(x,\omega)}{\partial x} + \frac{z_i e J_i^{charge}}{k_B T}\Delta\mu_i^*(x,\omega) \tag{2.110}$$

$$\frac{\partial \Delta J_i^{charge}(x,\omega)}{\partial x} = -j\omega\frac{(z_i e)^2 c_i(x)}{k_B T}\Delta\mu_i^*(x,\omega) \tag{2.111}$$

$$\Delta J_{dis}^{charge}(x,\omega) = -j\omega\varepsilon_r\varepsilon_0\frac{\partial \Delta\phi(x,\omega)}{\partial x} \tag{2.112}$$

$$\Delta J_T^{charge}(\omega) = \Delta J_{dis}^{ch\,\arg e}(x,\omega) + \sum_i \Delta J_i^{charge}(x,\omega) \tag{2.113}$$

2.3.2 Small-Signal Solution at the Boundaries

If the function g and h in (2.14) and (2.15) are known, the same methodology for the small-signal solution can be applied after obtaining the steady-state solution. However, generally the electrode reactions are much more complicated and the detailed electrochemical mechanisms can not be easily obtained. Thus here the boundary conditions were treated phenomenologically with boundary impedance $Z_i(a)$, $Z_i(c)$, $Z_{dis}(a)$ and $Z_{dis}(c)$. The idea is that for any specific electrochemical mechanism, it can be modeled by an equivalent impedance function.

The boundary conditions can be written as

$$\begin{aligned}
V(a) - \Delta\tilde{\mu}_i^*(0,\omega) &= Z_i(a)\Delta J_1^{charge}(0,\omega)A \\
V(a) - \Delta\phi(0,\omega) &= Z_{dis}(a)\Delta J_{dis}^{charge}(0,\omega)A \\
\Delta\tilde{\mu}_i^*(L,\omega) - V(c) &= Z_i(c)\Delta J_i^{charge}(L,\omega)A \\
\Delta\phi(L,\omega) - V(c) &= Z_{dis}(c)\Delta J_{dis}^{charge}(L,\omega)A
\end{aligned} \tag{2.114}$$

where $V(a)$ and $V(c)$ are boundary voltages.

2.3.3 Impedance Calculation

The total impedance is defined as

$$Z(\omega) = \frac{V(a) - V(c)}{\Delta J_T^{charge}(\omega)} \tag{2.115}$$

Again, equations (2.110)–(2.115) can only be solved numerically. First, the steady-state concentrations of charge carriers are calculated at discrete grid points x_i. The total number

of grid points is $N+1$ with $x_0 = 0$ and $x_N = L$. Then the system of volume elements is constructed. The edge of the volume elements is taken to be the middle position of the two adjacent grid points as in Figure 2.2. This method is the same as the work of Brumleve and Buck.[49]

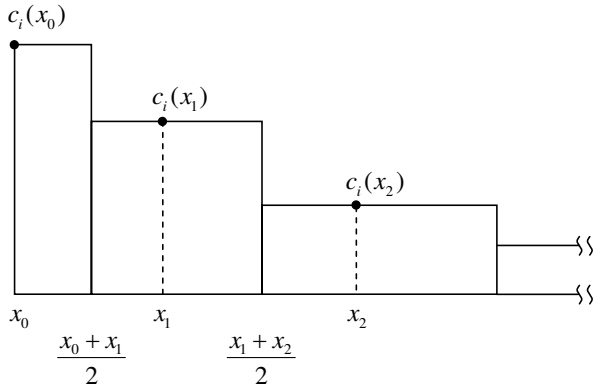

Figure 2.2: The system of carrier concentration grids and volume elements. The edges of volume elements are defined at the middle point between two grid points.

For this system of volume elements, equations (2.110)–(2.113) are discretized as

$$\Delta J_i^{charge}(\frac{x_n+x_{n+1}}{2},\omega) = -\frac{\sigma_i(x_n)+\sigma_i(x_{n+1})}{2}\frac{\Delta\tilde{\mu}_i^*(x_{n+1},\omega)-\Delta\tilde{\mu}_i^*(x_n,\omega)}{x_{n+1}-x_n} + \frac{z_i e J_i^{charge}}{k_B T}\frac{\Delta\mu_i^*(x_{n+1},\omega)+\Delta\mu_i^*(x_n,\omega)}{2},\ 0 \le n \le N-1 \quad (2.116)$$

$$\Delta J_i^{charge}(\frac{x_n+x_{n+1}}{2},\omega) - \Delta J_i^{charge}(\frac{x_{n-1}+x_n}{2},\omega) = -j\omega\frac{(z_i e)^2 c_i(x_n)}{k_B T}\frac{x_{n+1}-x_{n-1}}{2}\Delta\mu_i^*(x_n,\omega),\ 1 \le n \le N-1 \quad (2.117)$$

$$J_{dis}^{charge}(\frac{x_n+x_{n+1}}{2},\omega) = -j\omega\varepsilon_r\varepsilon_0\frac{\Delta\phi(x_{n+1},\omega)-\Delta\phi(x_n,\omega)}{x_{n+1}-x_n},\ 0 \le n \le N-1 \quad (2.118)$$

$$\Delta J_{dis}^{charge}(\frac{x_{n-1}+x_n}{2},\omega) + \sum_i \Delta J_i^{charge}(\frac{x_{n-1}+x_n}{2},\omega) = \Delta J_{dis}^{charge}(\frac{x_n+x_{n+1}}{2},\omega) + \sum_i \Delta J_i^{charge}(\frac{x_n+x_{n+1}}{2},\omega),\ 1 \le n \le N-1 \quad (2.119)$$

The above equations can be written as

$$I_i(n) = -\frac{V_i(n+1)-V_i(n)}{Z_i(n)} + I_i^0(n+1) + I_i^0(n), \quad 0 \le n \le N-1 \quad (2.120)$$

$$I_i(n) - I_i(n-1) = -\frac{V_i(n)-V_{dis}(n)}{Z_i^{chem}(n)}, \quad 1 \le n \le N-1 \quad (2.121)$$

$$I_{dis}(n) = -\frac{V_{dis}(n+1) - V_{dis}(n)}{Z_{dis}(n)}, \qquad 0 \le n \le N-1 \quad (2.122)$$

$$I_{dis}(n) + \sum_i I_i(n) = I_{dis}(n-1) + \sum_i I_i(n-1), \qquad 1 \le n \le N-1 \quad (2.123)$$

with the following parameters

$$Z_i(n) = R_i(n) = \left[\frac{\sigma_i(x_n) + \sigma_i(x_{n+1})}{2}\right]^{-1} \frac{x_{n+1} - x_n}{A}, \quad 0 \le n \le N-1 \quad (2.124)$$

$$Z_{dis}(n) = \frac{1}{j\omega C_{dis}(n)}, \qquad 0 \le n \le N-1 \quad (2.125)$$

$$C_{dis}(n) = \varepsilon_r \varepsilon_0 \frac{A}{x_{n+1} - x_n}, \qquad 0 \le n \le N-1 \quad (2.126)$$

$$Z_i^{chem}(n) = \frac{1}{j\omega C_i^{chem}(n)}, \qquad 1 \le n \le N-1 \quad (2.127)$$

$$C_i^{chem}(n) = \frac{(z_i e)^2 c_i(x_n)}{k_B T} \frac{x_{n+1} - x_{n-1}}{2} A, \qquad 1 \le n \le N-1 \quad (2.128)$$

$$Z_i^0 = \frac{2k_B T}{(z_i e)^2 J_i^{mass} A} \quad (2.129)$$

$$I_i(n) = \Delta J_i^{charge}(\frac{x_n + x_{n+1}}{2}, \omega) A, \qquad 0 \le n \le N-1 \quad (2.130)$$

$$I_{dis}(n) = \Delta J_{dis}^{charge}(\frac{x_n + x_{n+1}}{2}, \omega) A, \qquad 0 \le n \le N-1 \quad (2.131)$$

$$V_i(n) = \Delta \tilde{\mu}_i^*(x_n, \omega), \qquad 0 \le n \le N \quad (2.132)$$

$$V_{dis}(n) = \Delta \phi(x_n, \omega), \qquad 0 \le n \le N \quad (2.133)$$

$$V_i(n) - V_{dis}(n) = \Delta \mu_i^*(x_n, \omega), \qquad 0 \le n \le N \quad (2.134)$$

$$I_i^0(n) = \frac{V_i(n) - V_{dis}(n)}{Z_i^0}, \qquad 0 \le n \le N \quad (2.135)$$

It is apparent then that R_i in (2.124) is the resistance of carrier i in the volume element and C_{dis} in (2.126) is the dielectric capacitance of the element. C_i^{chem} in (2.128) is the "chemical capacitance" of carrier i, as termed by Jamnik and Maier,[33] and discussed in detail in Appendix A. The estimate of the usual electrical and chemical capacitances is given in Appendix B. Z_i^0 in (2.129) is the "source resistance" caused by the constant flux J_i^{mass}. I_i in (2.130) is the current flowing through R_i and I_{dis} in (2.131) is the current flowing through C_{dis}. V_i in (2.132) is the reduced electrochemical potential, V_{dis} in (2.133) is the electrical potential and $V_i - V_{dis}$ in (2.134) is the reduced chemical potential. Finally, I_i^0 in (2.135) is the voltage dependent current source. Using Kirchhoff's law, the above equations

(2.120)–(2.135) can also be mapped to an equivalent circuit with passive elements such as resistors (R_i) and capacitors (C_{dis}, C_i^{chem}) and active elements such as voltage controlled current sources (I_i^0). This mapping can give a better understanding of the physical processes and the frequency response of the system. For the mixed ionic and electronic conductor, the equivalent circuit is shown in Figure 2.3(a).

The boundary conditions (2.114) can be written as

$$\begin{aligned} V(a) - V_i(0) &= Z_i(a) I_i(0) \\ V(a) - V_{dis}(0) &= Z_{dis}(a) I_{dis}(0) \\ V_i(N) - V(c) &= Z_i(c) I_i(N) \\ V_{dis}(N) - V(c) &= Z_{dis}(c) I_{dis}(N) \end{aligned} \tag{2.136}$$

Similarly, (2.136) can also be mapped. The equivalent circuit at the boundaries is shown in Figure 2.3(b). Finally, the complete equivalent circuit including the electrodes is shown in Figure 2.4.

The above equations (2.120)–(2.136) can be written in the matrix form

$$\mathbf{AX} = \mathbf{B} \tag{2.137}$$

where $\mathbf{A}$ is a $(6N+3) \times (6N+3)$ sparse matrix with elements of $Z_i(n)$, $Z_{dis}(n)$, $Z_i^{chem}(n)$, Z_i^0, $Z_i(a)$, $Z_i(c)$, $Z_{dis}(a)$ and $Z_{dis}(c)$. The matrix $\mathbf{B}$ is a $6N+3$ column vector with elements of $V(a)$ and $V(c)$. The matrix $\mathbf{X}$ is a $6N+3$ column vector with elements of $I_i(n)$, $I_{dis}(n)$, $V_i(n)$ and $V_{dis}(n)$. For arbitrary chosen $V(a)$ and $V(c)$, $\mathbf{X}$ can be solved using Gaussian elimination and the impedance Z can be calculated as

$$Z(\omega) = \frac{V(a) - V(c)}{I_{ion}(1) + I_{eon}(1) + I_{dis}(1)} \tag{2.138}$$

An example of the circuit, $\mathbf{A}$, $\mathbf{X}$ and $\mathbf{B}$ for $N = 2$ is shown in Appendix C.

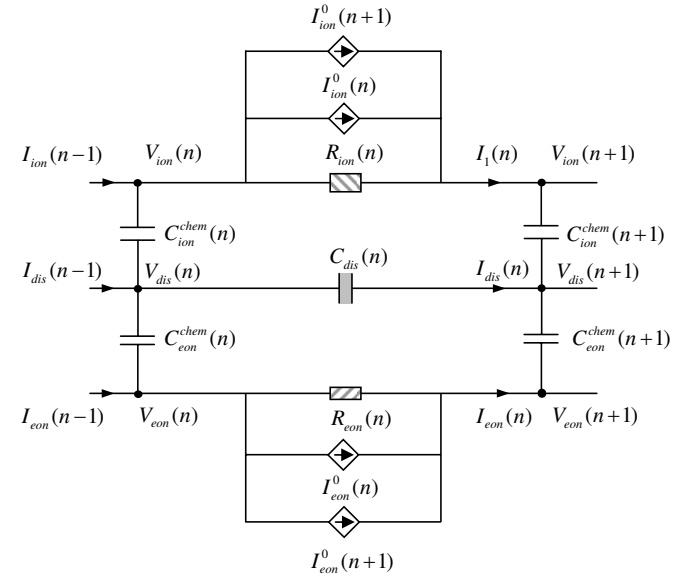

(a)

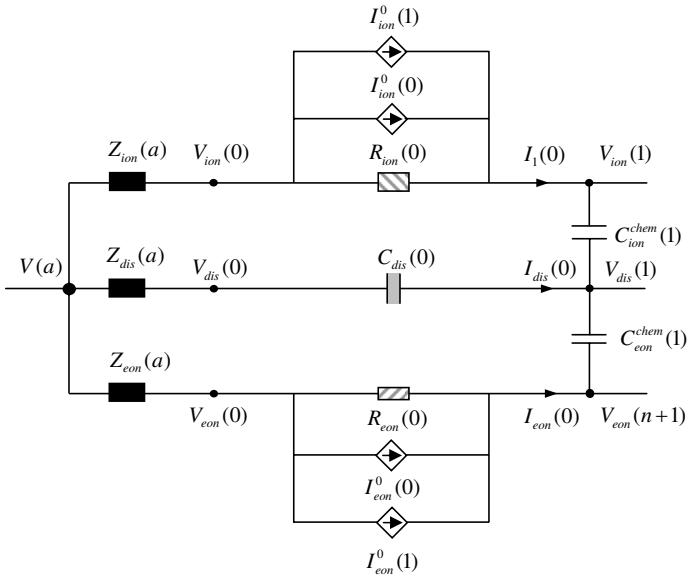

(b)

Figure 2.3: A.C. equivalent circuits for the mixed conductor under the nonequilibrium condition (a) within the electrolyte ($1 \leq n \leq N-1$) (b) at the boundary ($n = 0$).

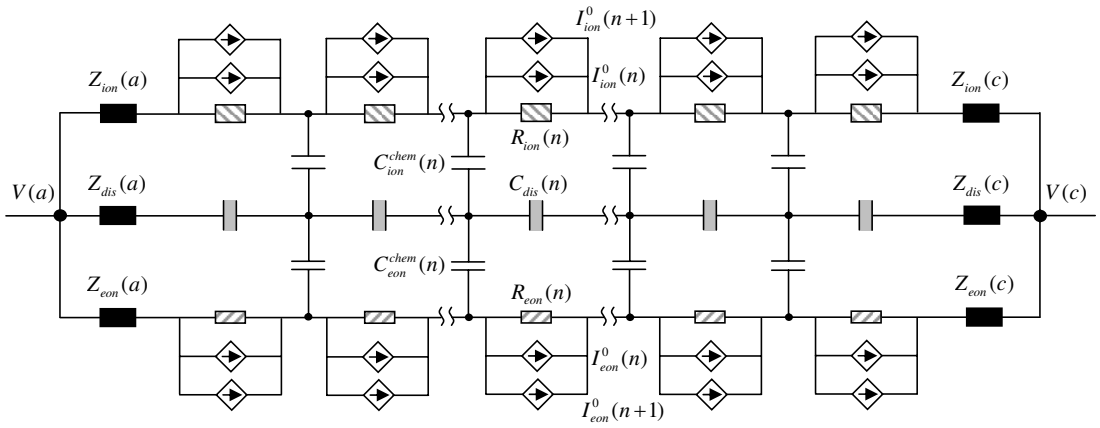

Figure 2.4: A.C. equivalent circuit for the mixed conductor including the electrodes under the nonequilibrium conditions.

2.3.3.1 System III

For the investigated system I, II and III with highly electronically conducting electrodes, Pt and BSCF, the electronic and dielectric transport at the boundaries is generally assumed to be reversible. In other words, the resistance to the electron and dielectric transport is assumed to be zero. For the ionic transport, the application of Chang-Jaffé boundary conditions will give interfacial resistors. If, however, one wishes to introduce interfacial capacitive effects, this can be done by replacing the interfacial resistors with parallel RQ circuits. This treatment is the modeling at the empirical level mentioned in Chapter 1. Although it is to be emphasized that electrodes in the most general case cannot be described by this simple representation, this model, as discussed below, yields an impedance that fits the experimental data very well. The complete system including the electrodes for system III is then represented as in Figure 2.5.

It is to be noted that, in fact, equilibrium conditions cannot be attained in a mixed conductor exposed to a chemical potential gradient because the flux in such a system will always be non-zero. With fixed partial pressures in the anode and cathode chambers (achieved via a constant flow of gases) steady-state conditions can be created, but not equilibrium. The present analysis shows that the equivalent circuit derived for a mixed conductor exposed to a uniform chemical potential (and thus equilibrium conditions), such as in the literature[33, 50] and in the following, can not be directly applied to represent the electrochemical behavior of mixed conductors exposed to chemical potential gradients.

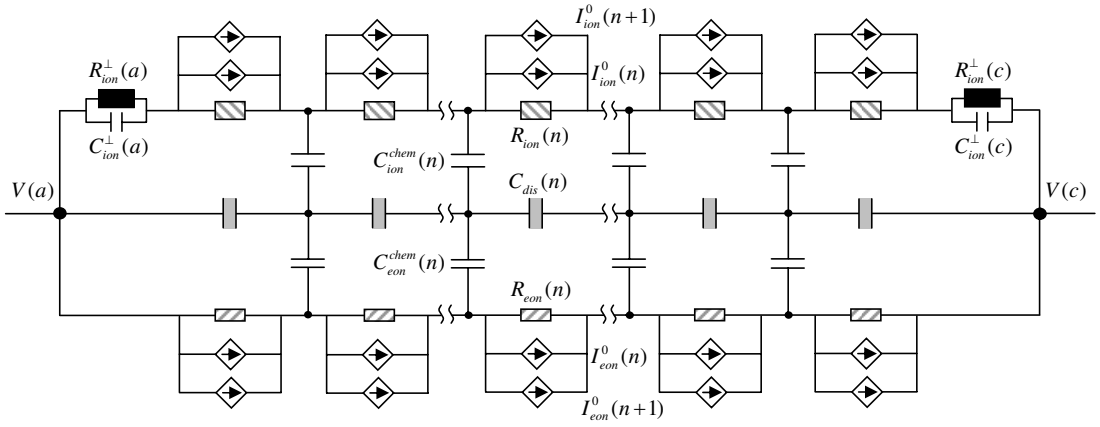

Figure 2.5: A.C. equivalent circuit for the mixed conductor of system III.

2.3.3.2 System II

In the above discussion for the nonequilibrium condition, J_i^{mass} is a non-zero constant. For the equilibrium condition $J_i^{mass} = 0$, the voltage controlled current source is zero from (2.129) and (2.135)

$$I_i^0(n) = 0 \tag{2.139}$$

(2.120) becomes

$$I_i(n) = -\frac{V_i(n+1) - V_i(n)}{Z_i(n+1)} \tag{2.140}$$

An example of the circuit, **A**, **X** and **B** for $N = 2$ under equilibrium condition is shown in Appendix C. Combining with the boundary conditions discussed above, the equivalent circuit to describe the equilibrium system is shown in Figure 2.6. It is to be noted that the elements are the same at the two boundaries since it is in equilibrium condition. This circuit has recently been discussed in the literature for a mixed conductor.[33, 50]

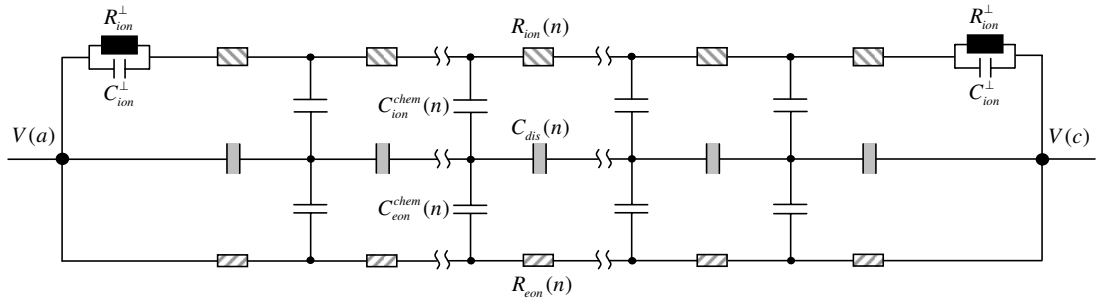

Figure 2.6: A.C. equivalent circuit for the mixed conductor of systems I and II.

Of course it is possible to calculate the whole frequency response of the whole circuit in Figure 2.6. However, it is also worthwhile looking at the simplified circuits at certain ranges of frequency limits and their corresponding physical characteristics. Depending on the magnitude of all the resistor and capacitor components in the circuit, the circuit can be separated to several subcircuits. The most popular approach is to separate the whole circuit to two subcircuits, a "low-frequency subcircuit" and a "high-frequency subcircuit." To keep the continuity of the subcircuits, the low-frequency limit of the "low-frequency subcircuit" should be equal to the D.C. limit of the whole circuit. The high-frequency limit of the "low-frequency subcircuit" should be equal to the low-frequency limit of the "high-frequency subcircuit." Finally, the high-frequency limit of the "high-frequency subcircuit" should be equal to the A.C. limit of the whole circuit.

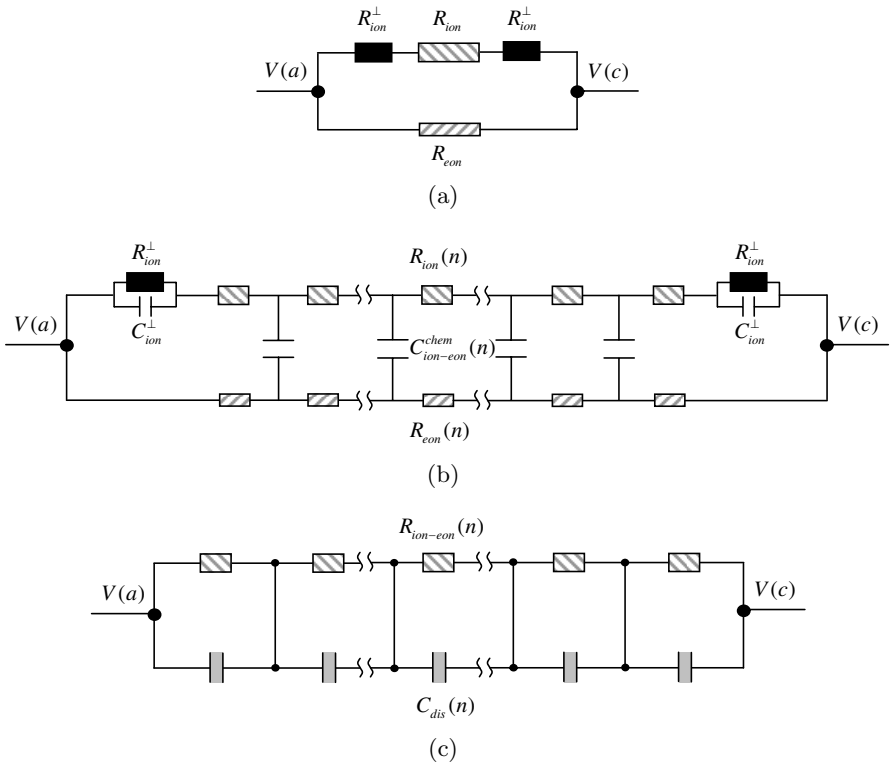

Figure 2.7: (a) D.C., (b) "low-frequency subcircuit," and (c) "high-frequency subcircuit" limits of the equivalent circuit in Figure 2.6.

The unit impedances of the components in Figure 2.6 in the Laplace domain are

$$\frac{R_i(n)}{(x_{n+1}-x_n)/A} = \left[\frac{\sigma_i(x_n)+\sigma_i(x_{n+1})}{2}\right]^{-1} \tag{2.141}$$

$$\frac{Z_{dis}(n)}{(x_{n+1}-x_n)/A} = (j\omega\varepsilon_r\varepsilon_0)^{-1} \tag{2.142}$$

$$Z_i^{chem}(n)\frac{(x_{n+1}-x_{n-1})A}{2} = \left[j\omega\frac{(z_ie)^2\,c_i(x_n)}{k_BT}\right]^{-1} \tag{2.143}$$

(1) At the D.C. limit ($\omega \to 0$). From (2.142) and (2.143), all the capacitors are effectively open. The whole circuit in Figure 2.6 is reduced to the circuit in Figure 2.7(a). The impedance of this circuit is

$$Z_0 = \left(\frac{1}{R_{ion}+2R_{ion}^{\perp}} + \frac{1}{R_{eon}}\right)^{-1} \tag{2.144}$$

with

$$R_i = \sum_n R_i(n) \tag{2.145}$$

which are the conventional resistance terms.

(2) At low frequencies, $\omega\varepsilon_r\varepsilon_0 \ll 1$. From (2.142), the capacitor $C_{dis}(n)$ is effectively open. The chemical capacitors $C_{ion}^{chem}(n)$ and $C_{eon}^{chem}(n)$ are in series and can be combined into a single chemical capacitor

$$C_{ion-eon}^{chem}(n) = \left[\frac{1}{C_{ion}^{chem}(n)} + \frac{1}{C_{eon}^{chem}(n)}\right]^{-1} \tag{2.146}$$

The resulting circuit is called the "low-frequency subcircuit" and shown in Figure 2.7(b). The low (0) and high (∞) frequency limits of this circuit are

$$Z_0^{low} = Z_0 \tag{2.147}$$

$$Z_\infty^{low} = \sum_n \left[\frac{1}{R_{ion}(n)} + \frac{1}{R_{eon}(n)}\right]^{-1} \tag{2.148}$$

It is worth noting the low-frequency limit of this "low-frequency subcircuit" is the same as the D.C. limit of the whole circuit as in Figure 2.7(a).

(3) At high frequencies, $\omega C_{ion}^{\perp} \gg 1$, $\omega\,(z_ie)^2\,c_i(x_n)/(k_BT) \gg 1$, both the capacitors $C_{ion}^{\perp}$ and $C_i^{chem}(n)$ in (2.143) are effectively shorted. The resistors $R_{ion}(n)$ and $R_{eon}(n)$ are in parallel and can be combined into a single resistor

$$R_{ion//eon}(n) = \left[\frac{1}{R_{ion}(n)} + \frac{1}{R_{eon}(n)}\right]^{-1} \tag{2.149}$$

The resulting circuit is called the "high-frequency subcircuit" and shown in Figure 2.7(c). The low(0) and high(∞) frequency limits of this circuit are

$$Z_0^{high} = Z_\infty^{low} \tag{2.150}$$

$$Z_\infty^{high} = 0 \tag{2.151}$$

It is worth noting the low-frequency limit of this "high-frequency subcircuit" is the same as the high-frequency limit of the "low-frequency subcircuit" in Figure 2.7(b).

(4) At the A.C. limit ($\omega \to \infty$), all the capacitors are effectively shorted.

$$Z_\infty = 0 \tag{2.152}$$

It is worth noting the high-frequency limit of the "high-frequency subcircuit" in Figure 2.7(c) is the same as the A.C. limit of the whole circuit. Thus the continuity of the subcircuits has been verified.

In predominately ionic conductors, $\omega e^2 c_{eon}(n)/(k_B T) \ll 1$ holds at all experimental frequencies. The circuit in Figure 2.6 is reduced to the one in Figure 2.8. Again, this circuit can be separated to a "low-frequency subcircuit" and a "high-frequency subcircuit."

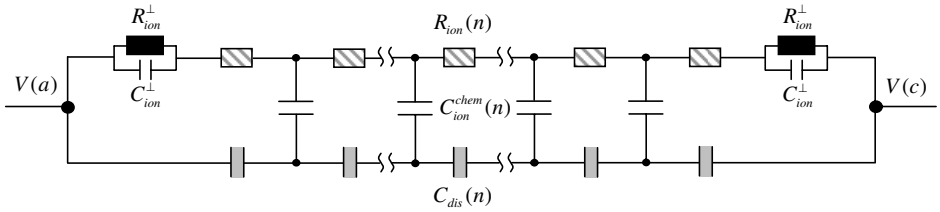

Figure 2.8: A.C. equivalent circuit for the ionic conductor of system I and II.

(1) At the D.C. limit ($\omega \to 0$), all the capacitors are effectively open. The whole circuit in Figure 2.8 is reduced to the circuit in Figure 2.9(a). The impedance of this circuit is

$$Z_0 = R_{ion} + 2R_{ion}^{\perp} \tag{2.153}$$

(2) At low frequencies, $\omega\varepsilon_r\varepsilon_0 \ll 1$, the capacitor $C_{dis}(n)$ is effectively open. The resulting circuit is called the "low-frequency subcircuit" and shown in Figure 2.9(b). The low(0) and high(∞) frequency limits of this circuit are

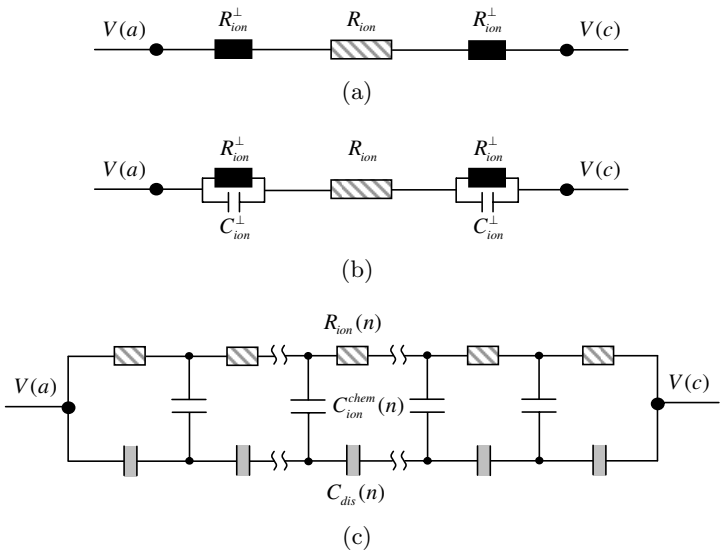

Figure 2.9: (a) DC.., (b) "low-frequency subcircuit," and (c) "high-frequency subcircuit" limits of the equivalent circuit in Figure 2.8.

$$Z_0^{low} = Z_0 \tag{2.154}$$

$$Z_\infty^{low} = R_{ion} \tag{2.155}$$

(3) At high frequencies, $\omega C_{ion}^{\perp}(n) \gg 1$, the capacitor $C_{ion}^{\perp}(n)$ is effectively shorted. The resulting circuit is called the "high-frequency subcircuit" and shown in Figure 2.9(c). The low(0) and high(∞) frequency limits of this circuit are

$$Z_0^{high} = Z_\infty^{low} \tag{2.156}$$

$$Z_\infty^{high} = 0 \tag{2.157}$$

(4) At the A.C. limit ($\omega \to \infty$), all the capacitors are effectively shorted

$$Z_\infty = 0 \tag{2.158}$$

Again, the continuity of the subcircuits has been verified.

Now we turn to the physical characteristics of the two subcircuits. Both the "high-frequency subcircuits" in Figure 2.7(c) and Figure 2.9(c) only include the contributions of the electrolyte components and thus can be characterized as "electrolyte subcircuits." If space charge regions exist at the grain boundaries, it can be shown numerically that both the two circuits will give two arcs in the Nyquist plot as shown in Figure 2.10. The one closer to the origin (high-frequency one) is the contribution from the grain interior and called the bulk or grain interior (GI) arc. The one farther away from the origin (low-frequency one) is the contribution from the space charge and called the grain boundary (GB) arc. If there is no space charge, the two arcs will be combined to a single arc.

Both the "low-frequency subcircuits" in Figure 2.7(b) and Figure 2.9(b) include contribution from both the electrolyte and electrode components. The circuit in Figure 2.9(b) will give a semicircular arc displaced from the origin in the Nyquist plot and the circuit in Figure 2.7(b) will give a half-tear-drop (Warburg) arc displaced from the origin as shown in Figure 2.10. While the "low-frequency" arc in Figure 2.10(b) can be described as the electrode arc since the electrolyte components only contribute a displacement from the origin, the arc in Figure 2.10(a) is mainly dominated by the chemical capacitance of the electrolyte as will be shown in the following discussion. It is worth noting Jamnik has obtained the similar results using a less strict approach.[51]

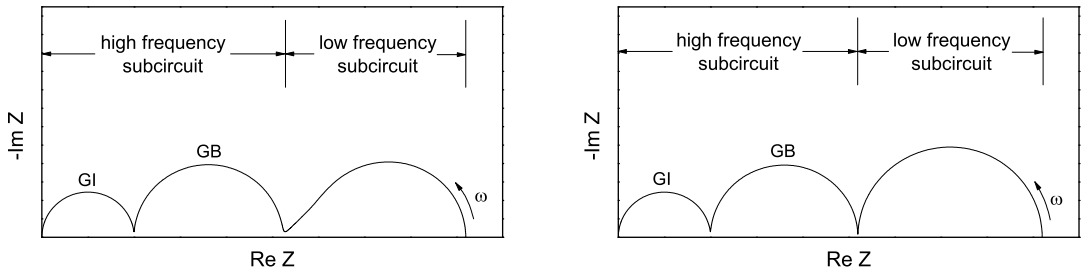

(a) (b)

Figure 2.10: Schematic Nyquist plots of the equivalent circuits in (a) Figure 2.6 for the mixed conductor and (b) Figure 2.8 for the ionic conductor respectively.

2.3.3.3 System I

For the equilibrium condition without space charge, the small-signal solution can also be simplified if electroneutrality is assumed to obey all the time. That is

$$z_{ion}ec_{ion}(x,t) + z_{eon}ec_{eon}(x,t) + z_{AD}ec_{AD} = 0 \tag{2.159}$$

For the small-signal perturbation

$$z_{ion}e\frac{\partial \Delta c_{ion}(x,t)}{\partial t} + z_{eon}e\frac{\partial \Delta c_{eon}(x,t)}{\partial t} = 0 \tag{2.160}$$

Combining this with the continuity equation, (2.12), one obtains

$$\frac{\partial \Delta J_{ion}^{charge}(x,t)}{\partial x} + \frac{\partial \Delta J_{eon}^{charge}(x,t)}{\partial x} = 0 \tag{2.161}$$

In the discrete form, this means

$$I_{ion}(n-1) - I_{ion}(n) + I_{eon}(n-1) - I_{eon}(n) = 0 \tag{2.162}$$

This result implies that any flux flowing from ionic carrier rail to the displacement rail is exactly balanced by that flowing to the displacement rail from electronic carrier rail. As a consequence, there is effectively no current flow between the carrier rails and the displacement rail (although flow between the two carrier rails remains possible). Accordingly, the elements in the circuit of Figure 2.6 can be simplified to that shown in Figure 2.11, by removing the electrical connection between the displacement rail and the two carrier rails. Doing so places $C_{ion}(n)$ and $C_{eon}(n)$ directly in series with one another (with no intervening branchpoints) and, thus, they can be combined into a single capacitance element $C_{ion-eon}^{chem}$ defined in (2.146).

For the equilibrium condition without the space charge, the carrier concentration $c_i(x)$ is constant from (2.66). If the volume elements are chosen to be equal in Figure 2.2, all the circuit elements $C_{dis}(n)$, $R_{ion}(n)$, $R_{eon}(n)$ and $C_{ion-eon}^{chem}(n)$ are equal individually.

Because of the isolated flow along the carrier and displacement rails, each of the dis-

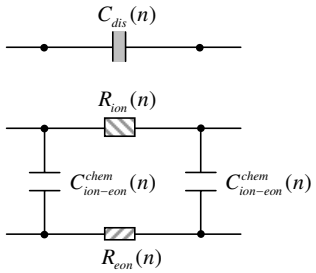

Figure 2.11: Simplified differential element of the equivalent circuit of Figure 2.6 under the additional condition of local charge neutrality.

placement capacitor elements are directly in series with one another and they can also be combined into one element

$$C_{dis} = \left[\sum_n \frac{1}{C_{dis}(n)}\right]^{-1} = \frac{\varepsilon_r \varepsilon_0 A}{L} = C_{dielec} \tag{2.163}$$

Thus, the capacitance along the displacement rail simply reduces to the conventional dielectric capacitance.

Although the resistances along the two carrier rails cannot be combined into single components, one can nevertheless define the total resistances encountered along these rails. They are given by

$$R_i = \sum_n R_i(n) = \frac{L}{\sigma_i A} \tag{2.164}$$

which are the conventional resistance terms for the two species. The resistances of the differential circuit elements are then

$$R_i(n) = \frac{R_i}{N} \tag{2.165}$$

where N is the (arbitrary) total number of differential subcircuits comprising the complete system.

One can similarly define a total chemical capacitance, C_{chem}, of the material system, which is simply the sum of all of the chemical capacitances of the differential portions of the circuit

$$C_{chem} = \sum_n C^{chem}_{ion-eon}(n) = \frac{e^2}{k_B T}\left(\frac{1}{z^2_{ion} c_{ion}} + \frac{1}{z^2_{eon} c_{eon}}\right)^{-1} AL \tag{2.166}$$

with

$$C_{ion-eon}^{chem}(n) = \frac{C_{chem}}{N} \tag{2.167}$$

describing the chemical capacitance of the element in the differential portion of the circuit. The complete circuit is shown in Figure 2.12.

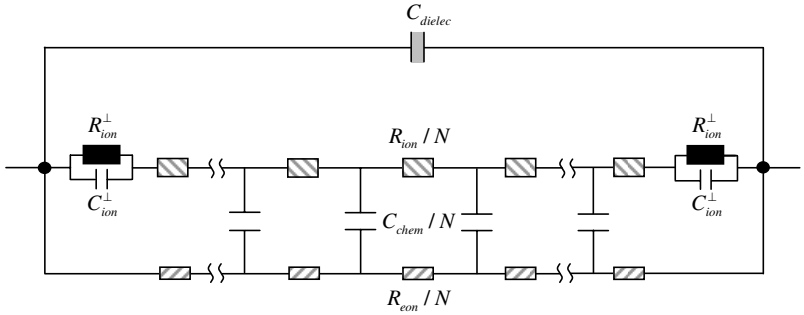

Figure 2.12: A.C. equivalent circuit for the mixed conductor of system I under the electroneutrality approximation.

Because C_{dielec} is typically small, it affects the impedance spectrum only at high frequencies, in most cases beyond the high-frequency measurement limit. For the remainder of the discussion the impact of the bulk dielectric capacitance, C_{dielec}, on the impedance response is omitted for clarity. Under these conditions, the equivalent circuit of Figure 2.12 is reduced to that given in Figure 2.13(a). This is the same circuit as in Figure 2.7(b) for the position independent circuit elements, *i.e.*, equilibrium condition without the space charge. For the pure ionic conductor, Figure 2.13(a) is reduced to that given in Figure 2.13(b). This is the same circuit as in Figure 2.9(b).

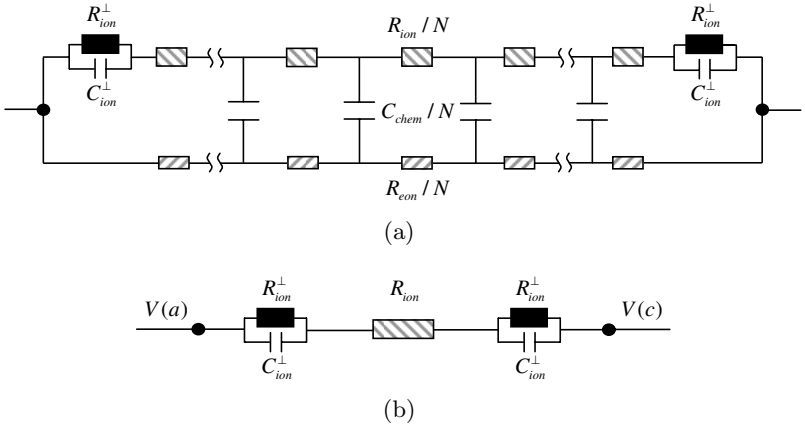

Figure 2.13: A.C. equivalent circuits for (a) the mixed conductor and (b) the ionic conductor of system I. The analytical expression for the impedance is given in (2.168)–(2.172) and (2.173) respectively.

The analytical expression for the impedance of the circuit of Figure 2.13(a) has been given by Jamnik and Maier[34] and is derived here in Appendix D. It is hereafter called the Jamnik-Maier model. It is worth noting there is a typographical omission of the term $(Z_0 - Z_\infty)$ in equation (7) of reference.[34] The impedance of Figure 2.13(a) is

$$Z(\omega) = R_\infty + (Z_0 - R_\infty) \frac{\tanh\sqrt{\frac{j\omega L^2}{4\tilde{D}}} + \frac{R_{ion}+R_{eon}}{2Z^\perp_{ion}} \tanh\sqrt{\frac{j\omega L^2}{4\tilde{D}}}}{\sqrt{\frac{j\omega L^2}{4\tilde{D}}} + \frac{R_{ion}+R_{eon}}{2Z^\perp_{ion}} \tanh\sqrt{\frac{j\omega L^2}{4\tilde{D}}}} \tag{2.168}$$

where

$$R_\infty = \frac{R_{ion}R_{eon}}{R_{ion}+R_{eon}} \tag{2.169}$$

$$\frac{1}{Z_0} = \frac{1}{R_{ion}+2Z^\perp_{ion}} + \frac{1}{R_{eon}} \tag{2.170}$$

$$Z^\perp_{ion} = \frac{R^\perp_{ion}}{1+j\omega R^\perp_{ion}C^\perp_{ion}} \tag{2.171}$$

$$\tilde{D} = \frac{L^2}{(R_{ion}+R_{eon})C_{chem}} \tag{2.172}$$

The analytical expression for the impedance of the circuit of Figure 2.13(b) is given by

$$Z(\omega) = R_{ion} + 2Z^\perp_{ion} \tag{2.173}$$

This equation can also be obtained by letting $R_{eon} \to \infty$ in (2.168)–(2.172) as expected.

Plotted in the complex plane (*i.e.*, in Nyquist form) the impedance spectra of the circuits in Figure 2.13(a) and Figure 2.13(b) have the general appearance of a single arc that is displaced from the origin (along the real axis of Z), examples of which are shown in Figure 2.14(a) and Figure 2.14(b) respectively. It is worth noting these plots have the same shapes as those of "low-frequency" arcs in Figure 2.10.

Graphical analyses of the types of spectra that result under certain limiting conditions from the impedance expressed in (2.168) have been presented by Jamnik and Maier,[34] but without analogous explicit expressions for $Z(\omega)$ or physical interpretation of the characteristic parameters of those spectra. Interpretation of the intercepts of the impedance

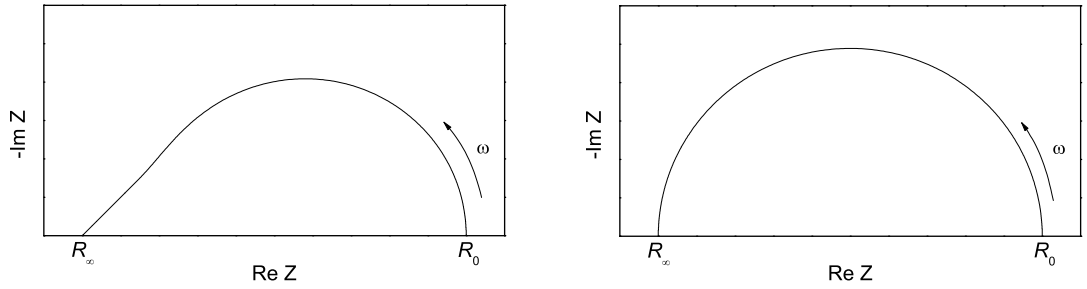

(a) (b)

Figure 2.14: Schematic Nyquist plots resulting from the circuit in Figure 2.13 for (a) the mixed conductor and (b) the ionic conductor.

spectra with the real axis, labeled R_∞ and R_0 in Figure 2.14, can be achieved by evaluation of the high and low-frequency limits of the circuit of Figure 2.13(a). At the high-frequency limit, all of the capacitors are effectively shorted, producing the circuit shown in Figure 2.15(a). The electrode resistance effectively disappears, and the impedance in this limit is $Z(\omega \to \infty) = R_\infty$. Thus, the high-frequency intercept corresponds to the total electrical resistance of the MIEC that results from adding the electronic and ionic components, R_{eon} and R_{ion}, in parallel, with

$$\frac{1}{R_\infty} = \frac{1}{R_{ion}} + \frac{1}{R_{eon}} \tag{2.174}$$

This is the same as (2.169).

At the low-frequency limit, all of the capacitors are effectively open, producing the circuit shown in Figure 2.15(b). This is the same as the one in Figure 2.7(a). The impedance in this limit, $Z(\omega \to 0) = R_0$, can be immediately determined from the circuit to obey

$$\frac{1}{R_0} = \frac{1}{R_{ion} + 2R_{ion}^{\perp}} + \frac{1}{R_{eon}} \tag{2.175}$$

This is the same as (2.144). In this case, the intercept corresponds to the electrical resistance of the system as a whole, and is the value that results from first adding the two ionic components together in series, and then adding this composite term with the electronic component together in parallel fashion.

(a) (b)

Figure 2.15: A.C. equivalent circuits representing that of Figure 2.13(a) in (a) the high-frequency limit in which all capacitors are shorted, and (b) the low-frequency limit in which all capacitors are open.

Two features of R_0 and R_∞ are noteworthy. First, in the case of a perfectly ion blocking electrode ($R^{\perp}_{ion}, Z^{\perp}_{ion} \to \infty$) with perfect reversibility for electrons ($R^{\perp}_{eon}, Z^{\perp}_{eon} = 0$), R_0 reduces to R_{eon}, which is precisely how one obtains the electronic component of the conductivity of a MIEC using blocking electrodes. Second, the difference between R_0 and R_∞ does not, in the general case, equate to the resistance of the electrodes, as it would in the case of a purely ionically conducting electrolyte. Instead, because R_0 depends on all three resistance terms of the system, further analysis, as described below, must be performed in order to extract the electrode resistance from the impedance data.

While (2.168) has been employed here for the analysis of the metal|ceria|metal system, it is noteworthy that under certain conditions, further simplifications occur. If C_{chem} is substantially larger than $C^{\perp}_{ion}$, then $C^{\perp}_{ion}$ can be ignored in the overall equivalent circuit ($Z^{\perp}_{ion} \to R^{\perp}_{ion}$) and the impedance becomes

$$Z(\omega) = R_\infty + (R_0 - R_\infty) \frac{\tanh\sqrt{\frac{j\omega L^2}{\tilde{D}}} + \frac{R_{ion}+R_{eon}}{2R^{\perp}_{ion}} \tanh\sqrt{\frac{j\omega L^2}{\tilde{D}}}}{\sqrt{\frac{j\omega L^2}{\tilde{D}}} + \frac{R_{ion}+R_{eon}}{2R^{\perp}_{ion}} \tanh\sqrt{\frac{j\omega L^2}{\tilde{D}}}} \tag{2.176}$$

The equivalent circuit of Figure 2.13(a) applies to a system in which a single step dominates the entire electrochemical reduction/oxidation reaction. In many cases, however, multiple sequential steps with differing time constants contribute to the overall process. Ideally, the impedance spectra yield detailed information regarding each of these reaction steps. In the present system, however, because $C_{chem} \gg C^{\perp}_{ion}$ (as shown below), the parallel resistor and capacitor of the electrode impedance to ion transfer can readily be approximated as a simple resistor (that is, $C^{\perp}_{ion} \sim 0$). Thus, the possible presence of additional parallel RC subcircuits that are in series with one another cannot be observed; each RC

subcircuit reduces to a resistor, and simple resistors in series cannot be individually measured. Electrode processes at the interface with a MIEC are thus inherently masked by the material's large chemical capacitance. This behavior is quite distinct from that of pure ionic conductors, in which multiple electrode arcs are routinely observed and their presence used to probe complex reaction pathways.[52]

2.4 Comparison of Empirical Equivalent Circuit Modeling and the Physical Equivalent Circuit Modeling

As discussed in Chapter 1, the Generalized Finite-Lengh Warburg (GFLW) element and ZARC element are the two most widely used elements in the empirical equivalent circuit modeling. In this section, the physical roots of these two elements will be shown in the context of the present physical equivalent circuit, Figure 2.7(b) of the mixed conductor and Figure 2.9(c) of the ionic conductor respectively.

2.4.1 Generalized Finite-Length Warburg Element

For the circuit in Figure 2.7(b), if there is *no* position dependence of the circuit elements, the impedance of the circuit is given analytically in (2.168) and simplified to (2.176). If, in addition, the resistance of the electrodes to ion transfer is high (*i.e.*, ion blocking) such that $2R_{ion}^{\perp} \gg R_{ion} + R_{eon}$, (2.176) is further reduced to

$$Z(\omega) = R_{\infty} + (R_0 - R_{\infty}) \frac{\tanh \sqrt{\frac{j\omega L^2}{4\tilde{D}}}}{\sqrt{\frac{j\omega L^2}{4\tilde{D}}}} \tag{2.177}$$

where R_{∞} is unchanged and R_0 is equal to R_{eon}. The second term of this result has the same mathematical form as the Finite-Length Warburg (FLW) impedance in section **??**. At the same time, without even resorting to the position dependence of the circuit elements, (2.176) alone will give the GFLW instead of FLW behaviors. An example is given for a set of parameters such as $R_{ion} = 3\ \Omega$, $R_{eon} = 11\ \Omega$, $R_{ion}^{\perp} = 14\ \Omega$, $C_{chem} = 4$ F. The Nyquist plot is shown schematically in Figure 2.16 along with a schematic FLW arc.

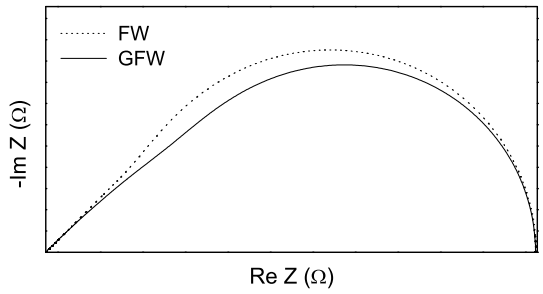

Figure 2.16: Schematic Nyquist plots of the Finite-Length Warburg (FLW) element and the Generalized Finite-Length Warburg (GFLW) element from the circuit in Figure 2.7(b).

2.4.2 ZARC Element

It is shown above that the GFLW element has its root in the equivalent circuit of the mixed conductor, Figure 2.7(b). It will be shown below that the ZARC element has its root in the equivalent circuit of the ionic conductor, specifically, Figure 2.9(c). For the circuit in Figure 2.9(c), if there is *no* position dependence of the circuit elements, the impedance can be obtained analytically when the discrete elements become continous or the number of elements N becomes infinite. In the terminology of Appendix D, the circuit in Figure 2.9(c) suggests $Z_A = Z_B = 0$, $Z_1 = R_{ion}$ and $Z_2 = Z_{dis}$. From (D.19), the impedance of the circuit is

$$Z = \frac{R_{ion} Z_{dis}}{R_{ion} + Z_{dis}} \tag{2.178}$$

with

$$R_{ion} = \frac{L}{\sigma_{ion} A} \tag{2.179}$$

$$Z_{dis} = \frac{L}{j\omega \epsilon_r \epsilon_0 A} \tag{2.180}$$

and the circuit in Figure 2.9(c) becomes the one in Figure 2.17. The Nyquist plot is shown schematically in Figure 2.18. This is the reason why a parallel RC circuit is used to model the charge carrier transport in the electrolyte in the literature.

On the other hand, if there is position dependence of the circuit elements, the impedance can only be obtained numerically. The material properties that can have position depen-

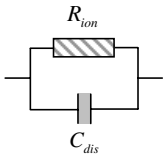

Figure 2.17: A.C. equivalent circuit simplified from Figure 2.9(c) for position independent circuit elements.

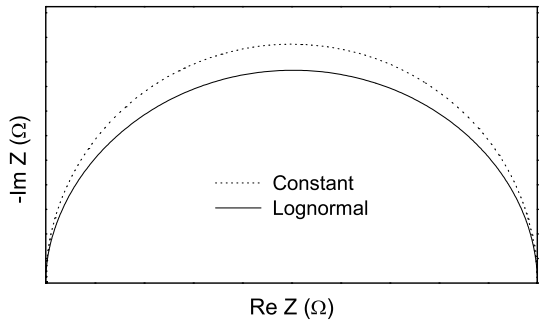

Figure 2.18: Schematic Nyquist plots of the circuit in Figure 2.9(c) with constant and lognormal distribution of concentrations.

dence are the ionic concentration c_{ion}, ionic mobility u_{ion} and dielectric constant ϵ_r. Here, the ionic concentration is taken to be an example. A number of $N = 100$ random values, representing 100 serial layers, is generated for the ionic concentration c_{ion} obeying the lognormal distribution. The simulation yields a depressed arc as schematically shown in Figure 2.18 for a set of materials parameters $T = 200$ °C, $c_{ion} = 1.83 \times 10^{-27}$ m^{-3}, $u_{ion} = 1.68 \times 10^{-12}$ m^2 V^{-1} s^{-1} and $\epsilon_r = 50$. The standard deviation of $\ln c_{ion}$ is taken to be 30%. The two arcs are scaled to the same magnitude for comparison. As discussed in section 1.3.3.6, the depressed arc can be modeled by a ZARC element with CPE. This simulation gives an example that CPE might come from the distribution of material properties in the real inhomogeneous materials.

2.4.3 Two ZARC Elements in Series

It is shown above the lognormal distribution of concentration in Figure 2.9(c) gives the depressed arc. On the other hand, if the position dependence of concentration is caused by the space charge like in Figure 1.1(c), it can be shown numerically that this leads to two arcs as those two GI and GB arcs shown in Figure 2.10. An example is given in Figure 2.19

for the same set of parameters as above, along with $\phi_0 = 0.250$ V.

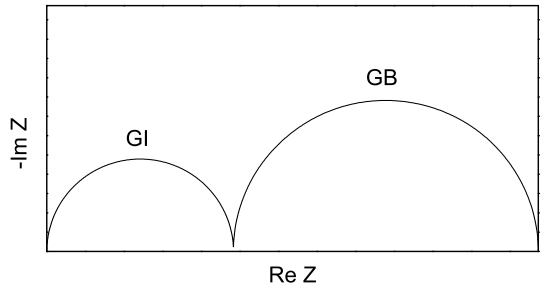

Figure 2.19: Schematic Nyquist plot of the circuit in Figure 2.9(c) with space charge.

Alternatively, the two GI and GB arcs in Figure 2.19 can be traditionally modeled by the equivalent circuit $R_{GI}Q_{GI} - R_{GB}Q_{GB}$. Constant phase elements Q_{GI} and Q_{GB} are converted to capacitances C_{GI} and C_{GB} using (1.67). If there is only mobile charge carrier such as ion, for the microstructure in Figure 1.1(b), one obtains

$$R_{GI} = \frac{1}{\sigma_{GI}} \frac{ND}{A} \tag{2.181}$$

$$R_{GB} = \frac{1}{\sigma_{GB}} \frac{N\delta_{GB}}{A} \tag{2.182}$$

$$C_{GI} = \varepsilon_r \varepsilon_0 \frac{A}{ND} \tag{2.183}$$

$$C_{GB} = \varepsilon_r \varepsilon_0 \frac{A}{N\delta_{GB}} \tag{2.184}$$

where σ_{GI} is the grain interior conductivity, σ_{GB} is the average grain boundary conductivity, D is the grain size or layer width, δ_{GB} is the grain boundary thickness, N is the number of grains or number of serial layers, A is the area and L is the length as in Figure 1.1(b). Here the dielectric constants are assumed to be the same for both GI and GB.

Since the grain size D is generally much bigger than the grain boundary width δ_{GB}, the approximation of $L \approx ND$ is used and (2.181) becomes

$$\sigma_{GI} = \frac{L}{R_{GI}A} \tag{2.185}$$

Dielectric constant ε_r can be obtained from (2.183)

$$\varepsilon_r = \frac{LC_{GI}}{A\varepsilon_0} \tag{2.186}$$

(2.182) and (2.184) leads to

$$\sigma_{GB} = \frac{\varepsilon_r \varepsilon_0}{R_{GB} C_{GB}} \tag{2.187}$$

Thus microscopic properties σ_{GI}, σ_{GB} and ε_r can be obtained from impedance measurement.

There is a simple model that relates the space charge resistance to the space charge potential.[53–55] The space charge resistance is generally written as

$$R_{SC} = \int_0^{\lambda_{SC}} \frac{1}{\sigma_{ion}(x)} \frac{dx}{A} = \int_0^{\lambda_{SC}} \frac{1}{2eu_{ion}c_{ion}(x)} \frac{dx}{A} \tag{2.188}$$

If it is assumed that the mobilities in the grain interior and space charge regions are the same, one gets

$$R_{SC} = \frac{1}{\sigma_{ion}^{\infty} A} \int_0^{\lambda_{SC}} \exp\left[\frac{2e\phi(x)}{k_B T}\right] dx \tag{2.189}$$

with

$$\sigma_{ion}^{\infty} = 2eu_{ion}c_{ion}^{\infty} \tag{2.190}$$

The space charge potential has a quadratic form as in (2.61) thus there is no analytic expression for (2.189). Since only the region very close to the origin contribute to the total resistance, $\phi(x)$ can be expanded around $x = 0$ as

$$\phi(x) \approx \phi_0 + \left.\frac{d\phi}{dx}\right|_{x=0} x = \phi_0 \left(1 - \frac{2}{\lambda_{SC}} x\right) \tag{2.191}$$

(2.189) and (2.191) lead to

$$R_{SC} = \frac{\lambda_{SC}}{\sigma_{ion}^{\infty}} \frac{1}{\frac{4e\phi_0}{k_B T} A} \left[\exp\left(\frac{2e\phi_0}{k_B T}\right) - \exp\left(-\frac{2e\phi_0}{k_B T}\right)\right] \tag{2.192}$$

This is the same result as the work of Fleig, Rodewald and Maier.[53] Actually, when (2.191) is used, the space charge potential becomes 0 at $\lambda_{SC}/2$. Changing the upper limit in (2.188) from λ_{SC} to $\lambda_{SC}/2$ gives

$$R_{SC} = \frac{\lambda_{SC}}{\sigma_{ion}^{\infty}} \frac{1}{\frac{4e\phi_0}{k_B T} A} \left[\exp\left(\frac{2e\phi_0}{k_B T} \right) - 1 \right] \tag{2.193}$$

This is the same result as the work of Guo and Maier.[54] Under typical conditions, $2e\phi_0/(k_B T) \gg 1$, both (2.192) and (2.193) become

$$R_{SC} = \frac{\lambda_{SC}}{\sigma_{ion}^{\infty} A} \frac{\exp\left(\frac{2e\phi_0}{k_B T} \right)}{\frac{4e\phi_0}{k_B T}} \tag{2.194}$$

(2.194) can be written as

$$\frac{\sigma_{ion}^{\infty}}{\sigma_{SC}} = \frac{\exp\left(\frac{2e\phi_0}{k_B T} \right)}{\frac{4e\phi_0}{k_B T}} \tag{2.195}$$

with specific space charge conductivity defined as

$$\sigma_{SC} = \frac{\lambda_{SC}}{R_{SC} A} \tag{2.196}$$

(2.195) is widely used to calculate the space charge effect.[56] It is worth noting that σ_{GB} is the same as σ_{SC} and σ_{GI} is the same as σ_{ion}^{∞}. Thus from (2.185), (2.187), (2.195) and (2.196)

$$\frac{\exp\left(\frac{2e\phi_0}{k_B T} \right)}{\frac{4e\phi_0}{k_B T}} = \frac{\frac{L}{R_{GI} A}}{\frac{\varepsilon_r \varepsilon_0}{R_{GB} C_{GB}}} \tag{2.197}$$

The numerical solution of (2.197) gives the space charge potential ϕ_0. For example, the application of this method gives a space charge potential of 0.254 V which is almost the same as 0.250 V in the physical equivalent circuit model.

Chapter 3

Experiments, Results, and Discussions

3.1 Experiments

3.1.1 Materials

Commercial $Sm_{0.15}Ce_{0.85}O_{1.925-\delta}$ (SDC15) powders were purchased from NexTech Materials. The loose powders were annealed at 950 °C in air for 5 hours in order to lower the surface area and ensure the desired sintering behavior. Pellets were uniaxially pressed at 300M Pa and then sintered at 1350 °C (systems I and III) and 1550 °C (system II) for 5 hours to obtain a relative density of over 95%. The samples used for measurement were 0.78 mm thick with a diameter of 13 mm (System I), 0.65 mm thick with a diameter of 13.08 mm (system II) and 0.64 mm thick with a diameter of 13 mm (system III), respectively.

Pt ink (Engelhard 6082) was applied to the complete surface of the pellets and fired at 900 °C for 2 hours. Cathode material $Ba_{0.5}Sr_{0.5}Co_{0.8}Fe_{0.2}O_{3-\delta}$ (BSCF) was prepared by a sol-gel method in which both EDTA and citric acid served as chelating agents.[4] The resulting powders were mixed with α-terpineol (Sigma-Aldrich) to form a paste, which was then brush-painted onto the surface of the pellets and fired at 1000 °C for 5 hours, with an electrode area of 0.71 cm^2.

Powder X-ray diffraction (XRD) data of SDC15 were collected at room temperature using a Philips PW 3040 diffractometer with CuKα radiation in the Bragg-Brentano geometry. The lattice constant of SDC15 was obtained from Rietveld refinement of the powder X-ray diffraction data, using Ni as the internal standard. The thermal expansion was taken

to be 12.1 ppm.[57] The dopant concentration c_{AD} is obtained from the nominal composition and the lattice constant. The microstructure and morphology were examined using ZEISS LEO 1550VP field-emission Scanning Electron Microscope (SEM). The average grain size of SDC15 was obtained from the mean linear intercept method. The relation between the averaging grain size D and the mean linear intercept $\bar{l}$, depends on the grain shape and grain size distribution.[58,59] For example, the proportional constant is 1.5, 1.775 and 2.25 for single size spheres, tetrakaidecahedra and cubes respectively. Generally, a reasonable choice for the grain shape is a tetrakaidecahedron and the grain size shape distribution has been estimated from both theoretical and experimental studies. A proportionality constant of 1.56 is generally used in the literature.[58] In this work, the same constant will be used such that $D = 1.56\bar{l}$.

Typical SEM pictures of SDC15 sintered at 1350 °C (surface) and 1550 °C (cross section), BSCF on SDC15 (surface) and Pt on SDC15 (surface) are shown in Figure 3.1. The mean linear intercepts are 0.5 um and 4.0 um for SDC15 sintered at 1350 °C and 1550 °C respectively.

3.1.2 Experimental Setup

The schematic experimental setup is shown in Figure 3.2(a) for systems I and II, and in Figure 3.2(b) for system III. Electrical contacts were made with silver meshes and silver wires. For system III, the pellet was sealed onto alumina tubes using an alumina-based adhesive (Aremco, Cerambond 552-VFG) with a cathode area of 0.71 cm^2. The internal resistance and inductance of the setup were measured from blank tests.

For systems I and II, two-probe A.C. impedance spectroscopy was performed using a Solartron 1260A impedance analyzer with a voltage amplitude 10–70 mV and a frequency range spanning from 10m Hz or 1m Hz to 10k – 1M Hz. The impedance was measured at 500, 550, 600 and 650 °C under atmospheres ranging from simulated air to 3% H_2O-saturated H_2. Oxygen partial pressures from 10^{-6} to 0.21 atm were obtained from mixtures of Ar and O_2; lower oxygen partial pressures were achieved using mixtures of Ar, H_2 and H_2O, assuming thermodynamic equilibrium between O_2, H_2 and H_2O. The gas flow rates were fixed using mass flow controllers (MKS Instruments) to a total flow rate of 100 sccm,

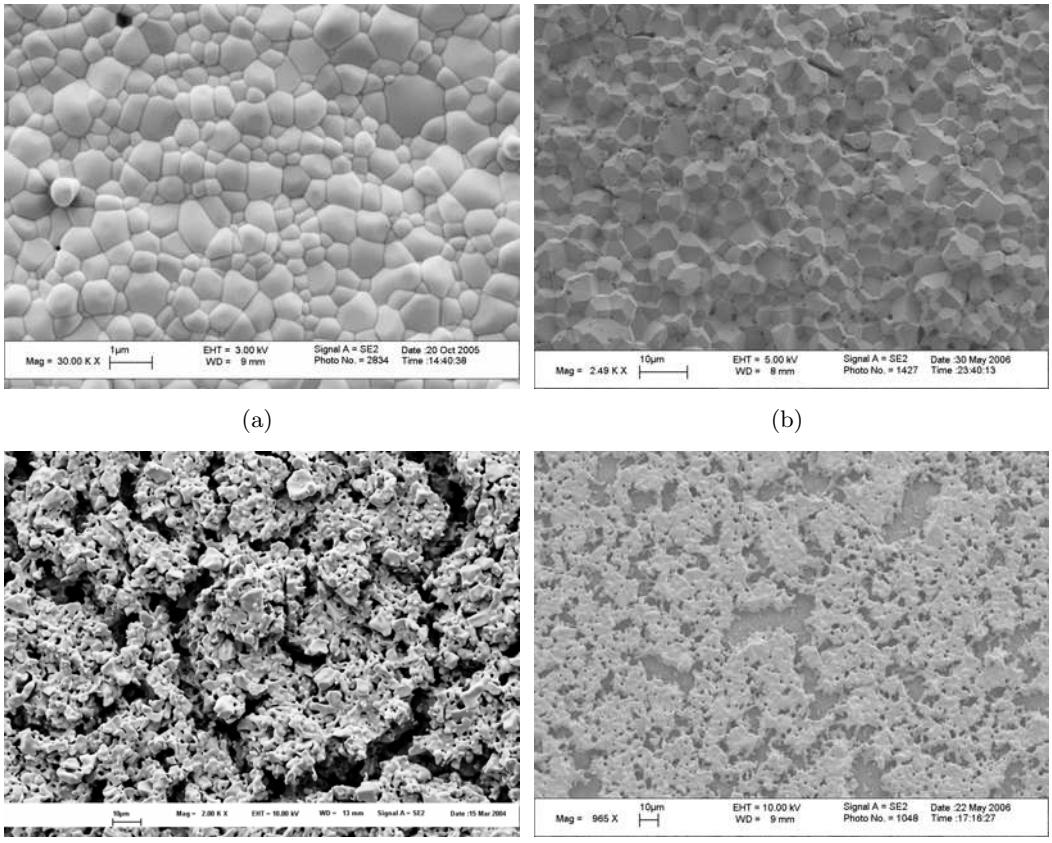

(a) (b)

(c) (d)

Figure 3.1: SEM images of (a) surface of SDC15 sintered at 1350 °C, (b) cross-section of SDC15 sintered at 1550 °C, (c) surface of BSCF on SDC15 and (d) surface of Pt on SDC15.

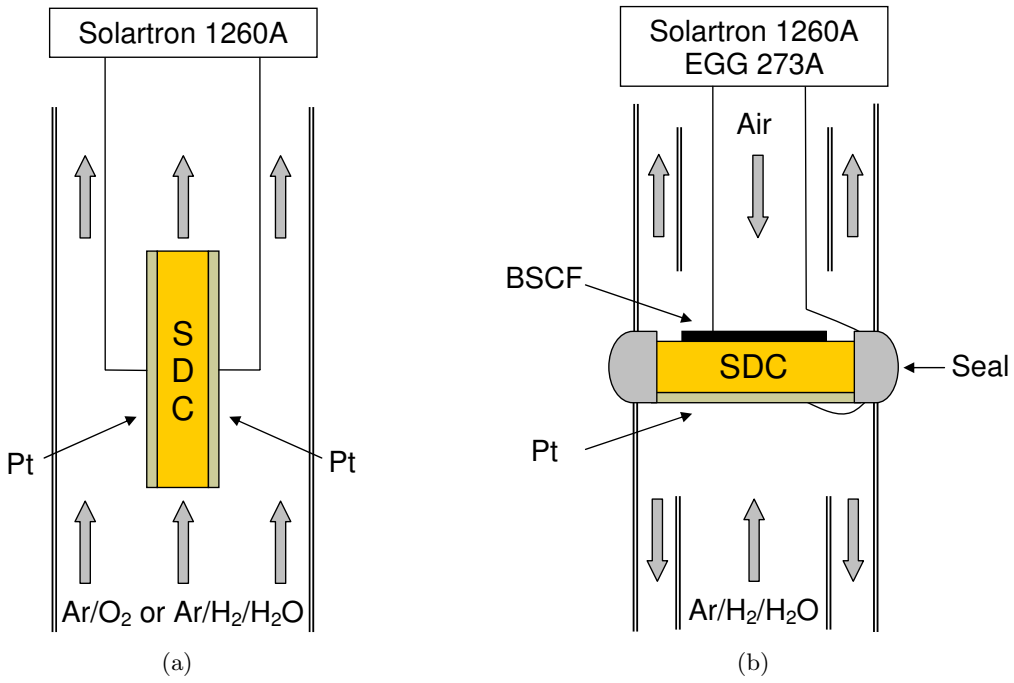

Figure 3.2: Schematics of experimental setup of three systems

Schematics of experimental setup of (a) systems I, II and (b) system III.

which, for the dimensions of the system utilized implies a linear gas flow rate of ∼0.74 cm/s. The whole system was allowed to stabilize at each condition before the final measurement. The typical stabilization time was 1 hour under high oxygen partial pressures and 5-8 hours under low oxygen partial pressures. In light of the small amplitude of the applied voltage and the small sample size relative to the overall flow rate and dimensions of the experimental apparatus, the gas composition is safely assumed to be unperturbed by the impedance measurement.

For system III, the electrochemical impedance measurement was carried out using a Solartron 1260A impedance analyzer in combination with a Princeton Applied Research EG&G 273A potentiostat/galvanostat. A small amplitude of 10 mV in the potentiostatic mode was used and data were collected over the frequency range 1m Hz – 60k Hz. A flow of 100 sccm air was supplied to the cathode side as the oxidant. Mixtures of Ar and H_2 (with Ar:H_2 ratios of 0:100, 50:50, and 20:80) saturated with 3% H_2O were supplied to the anode at a total flow rate of 50 sccm. The oxygen partial pressure in the anode chamber was calculated assuming thermodynamic equilibrium between O_2, H_2 and H_2O. Data were

collected at 550, 600 and 650 °C after stabilization for 30 minutes.

3.2 System I

3.2.1 Impedance Spectra and Data Analysis Procedures

Typical impedance spectra obtained from Pt|SDC15|Pt are presented in Figure 3.3(a) and 3.3(b). The data were collected at 600 °C at several different oxygen partial pressures. The spectra in Figure 3.3(a) reveal quite clearly that for oxygen partial pressures as low as 1.1×10^{-17} atm (at 600 °C) SDC15 is a pure ionic conductor. The high-frequency intercept with the real axis is unchanged for the three measurements, and the single arc in each spectrum has the form of a depressed, yet symmetric, semicircle. In contrast, the spectra in Figure 3.3(b) demonstrate that ceria is a mixed conductor at oxygen partial pressures of 5.5×10^{-23} atm and lower (at 600 °C). The arcs are asymmetric, exhibiting a characteristic Warburg-like shape, and the high-frequency intercept with the real axis decreases with decreasing oxygen partial pressure. The shape of the arcs in both oxidizing and reducing conditions correspond to those in Figure 2.14.

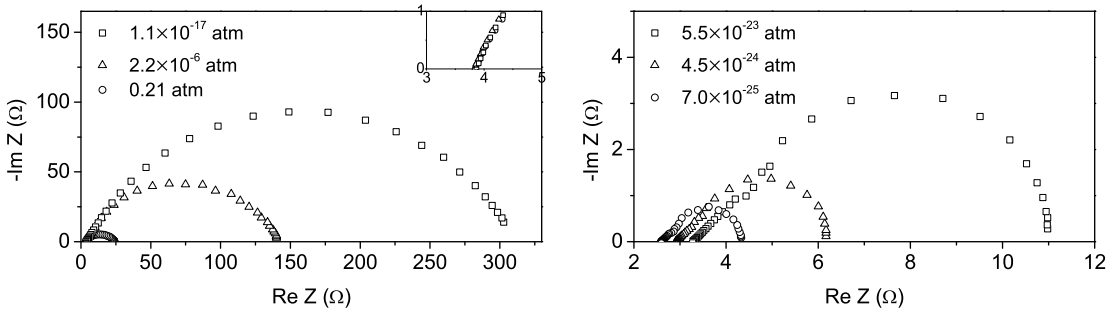

(a) (b)

Figure 3.3: Measured impedance response of Pt|SDC15|Pt at 600 °C under (a) moderately oxidizing conditions where ceria is an ionic conductor (insert shows the high-frequency portion of the data) and (b) reducing conditions where ceria is a mixed conductor.

As discussed in Chapter 2, for system I, the steady-state solution in the electrolyte is given in (2.67) and (2.68). The small-signal solution is described by the equivalent circuit is Figure 2.13(a) and the analytical expression is given by (2.168)–(2.172). For

both the steady-state and small-signal solutions, there are five independent parameters: the bulk ionic and electronic resistances, R_{ion} and R_{eon}, the interfacial resistance $R_{ion}^{\perp}$ and capacitance $C_{ion}^{\perp}$ of the electrodes to ion transfer, and the chemical capacitance C_{chem}. Since the concentration of the majority carriers c_{ion} is given from the material stoichiometry (*i.e.*, extrinsic dopant concentration), (2.56), one can use the definition of the chemical capacitance, (2.166), to evaluate the concentration of minority carriers c_{eon}. Morever, from the behavior of c_{eon} as a function of oxygen partial pressure, (2.57), K_r can be obtained and its dependence on temperature evaluated to yield ΔS_r and ΔH_r. With both the resistances and concentrations of the mobile species known, one can then establish the mobilities. In this manner, it is possible to completely characterize the thermodynamic and electrical properties of mixed ionic and electronic conductors simply from the measurement of A.C. impedance spectra.

Under oxidizing conditions, the equivalent circuit becomes the one in Figure 2.13(b) and the analytical expression of the impedance, (2.168), becomes (2.173). R_{ion} is obtained from the high-frequency intercept with the real axis. Due to the inhomogeneity of the electrode, $R_{ion} - R_{ion}^{\perp}Q_{ion}^{\perp}$ is used to fit the experimental spectra where $Q_{ion}^{\perp}$ is the constant phase element. $Q_{ion}^{\perp}$ is then converted to $C_{ion}^{\perp}$ according to (1.67). As discussed above, R_{ion} is independent of p_{O_2}, and $C_{ion}^{\perp}$ can be, to a first approximation, also taken to be independent of p_{O_2}.

Under reducing conditions, the values obtained for R_{ion} and $C_{ion}^{\perp}$ under the ionic regime were used as fixed parameters in the analysis of the experimental spectra. Thus R_{eon}, $R_{ion}^{\perp}$ and C_{chem} were the three fitting parameters. The experimental impedance spectra were fitted to (2.168) using *ZView* (Scribner Associated). It must be emphasized that such a procedure works well for a material such as ceria in which both the electrolytic and mixed conducting regimes are experimentally accessible. Alternative strategies may be required if only data from the mixed conducting regime are available.

3.2.2 Derived Results

The oxygen partial pressure dependence of the total electrical conductivity of SDC15 (as determined from the high-frequency intercept) at 500, 550, 600 and 650 °C is shown in

Figure 3.4(a). At moderate oxygen partial pressures, the conductivity is predominantly ionic and remains constant, whereas at low oxygen partial pressures, the conductivity is primarily electronic, rising as p_{O_2} decreases. The experimental data of Figure 3.4(a) are well described by the defect chemistry model $\sigma_T = \sigma_{ion} + \sigma^0_{eon} p_{O_2}^{-1/4}$, (1.12), yielding both σ_{ion} and σ^0_{eon}. The Arrhenius plots for these two parameters are shown in Figure 3.4(b). As discussed in Chapter 1, the activation energy obtained for σ_{ion}, 0.67 ± 0.01 eV, is the oxygen ion migration enthalpy, whereas that obtained for σ^0_{eon}, 2.31 ± 0.02 eV, includes both the electron migration enthalpy and the reduction enthalpy.

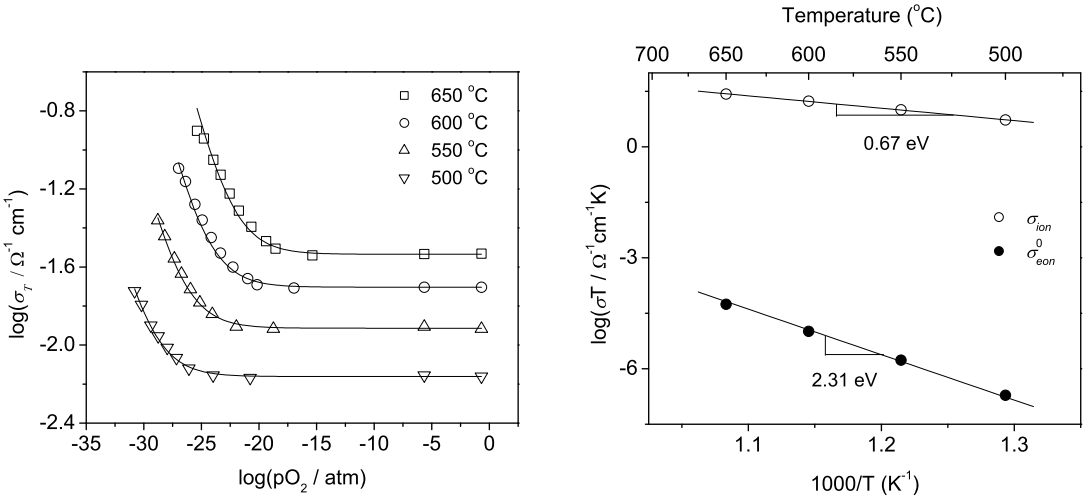

(a) (b)

Figure 3.4: (a) Total electrical conductivity of SDC15 at 500, 550, 600 and 650 °C as a function of oxygen partial pressure. Solid lines show the fit to $\sigma_T = \sigma_{ion} + \sigma^0_{eon} p_{O_2}^{-1/4}$. (b) Ionic conductivity, σ_{ion}, and oxygen partial pressure independent term in the electronic conductivity, σ^0_{eon}, of SDC15 as functions of temperature, plotted in Arrhenius form.

Turning to the physical parameters determined from direct fits of the impedance spectra obtained under mixed conducting conditions to $Z(\omega)$ as given in (2.168), it is important to first establish whether or not the data are well described by the Jamnik-Maier formalism. As evidenced from Figure 3.5, comparisons of the measured and fitted data at 600 °C and p_{O_2}=5.5×10^{-23} atm, the fit to the Jamnik-Maier model is very good.

While in the previous discussion, the electronic resistance R_{eon} or electronic conductivity σ_{eon} was obtained from the high-frequency intercept with the real axis of the impedance

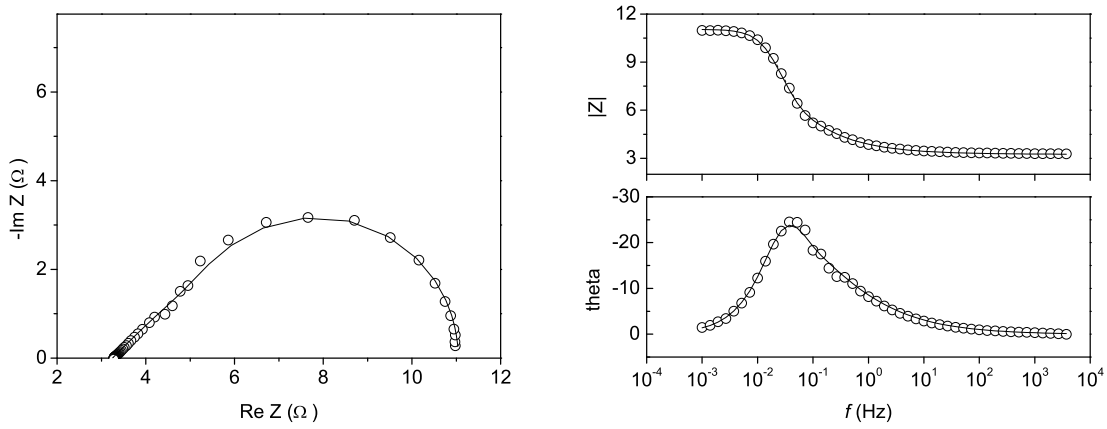

(a) (b)

Figure 3.5: Comparison of the measured and fitted impedance obtained from the Pt|SDC|Pt system at 600 °C and an oxygen partial pressure of 5.5×10^{-23} atm. The fit is to (2.168) of the main text. (a) Nyquist representation, and (b) Bode-Bode representation.

spectra only, R_{eon} is also one of the fitting parameters from the direct fits of the impedance spectra obtained under mixed conducting conditions to $Z(\omega)$. Similarly, the fit of electronic conductivity σ_{eon} to the $\sigma_{eon} = \sigma^0_{eon} p_{O_2}^{-1/4}$ will also give σ^0_{eon}. σ^0_{eon} obtained in this way is shown in Figure 3.6 along with the values obtained from the high-frequency intercept. The values obtained by the two methods are similar but the direct fitting method gives a slightly higher activation energy of 2.44 ± 0.03 eV than 2.31 ± 0.02 eV from the high-frequency intercept method. The values from the direct fitting method will be used in the following discussions.

The interfacial capacitance $C^{\perp}_{ion}$ under oxidizing conditions and chemical capacitance C_{chem} under reducing conditions are shown in Figure 3.7(a) and Figure 3.7(b) respectively. As expected from (2.166), the behavior of C_{chem} is dominated by the concentration of electronic carriers. Furthermore, this parameter is, under all conditions examined, far greater than $C^{\perp}_{ion}$, and $C^{\perp}_{ion}$ as measured within the electrolytic regime is indeed largely independent of p_{O_2}. Because $C_{chem} \gg C^{\perp}_{ion}$, analyses performed in which $C^{\perp}_{ion}$ was omitted from the equivalent circuit, *i.e.*, using (2.176), had negligible impact on the quality of the fits and the derived values for the other parameters. Thus, the assumption of a constant $C^{\perp}_{ion}$ (independent of p_{O_2}), even if in error, would introduce negligible errors to the other

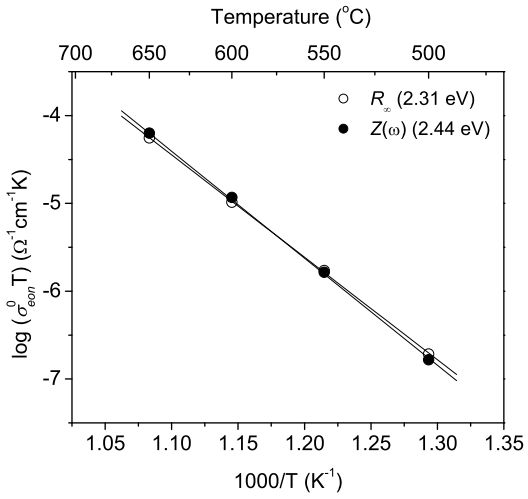

Figure 3.6: Oxygen partial pressure independent term in the electronic conductivity, σ^0_{eon}, obtained from the high-frequency intercept of the impedance spectra and fitting of the whole impedance spectra, as a function of temperature plotted in Arrhenius form.

terms.

The electronic defect concentration c_{eon}, Figure 3.8(a), behaves as expected on the basis of the defect chemistry model. In particular, for the two lower temperature measurements, c_{eon} obeys a clear $-1/4$ power law dependence on oxygen partial pressure over the entire p_{O_2} range examined. At higher temperatures, the electronic defect concentration begins to deviate from the expected p_{O_2} dependence as the oxygen partial pressure is lowered. Under these conditions, the concentration of oxygen vacancies generated by the reduction reaction, (1.1), becomes significant and the oxygen vacancy concentration can no longer be treated as constant. To ensure that the approximation $c_{ion} = c_{AD}/2$ is adequately obeyed, further analysis is restricted to the region in which the electronic defect concentration is less than one-fifth of the (extrinsic) oxygen vacancy concentration. Taking this restriction into account and fitting c_{eon} to (2.68), one obtains the equilibrium constant, K_r, as a function of temperature, Figure 3.8(b). From these data the reduction entropy ΔS_r and enthalpy ΔH_r are derived to be $(1.18 \pm 0.05) \times 10^{-3}$ eV/K and 4.18 ± 0.05 eV, respectively.

From the conductivities and charge carrier concentrations, Figure 3.6 and Figure 3.8(a) respectively, one can obtain both the ionic and electronic mobilities, and these are presented in Figure 3.9 along with available literature data.[2,3] The activation energies are 0.67 ± 0.01

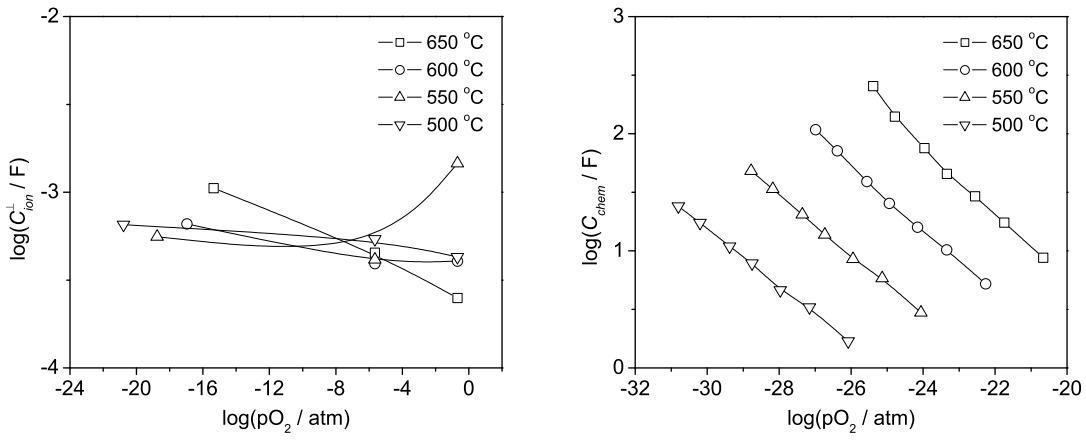

(a) (b)

Figure 3.7: (a)Interfacial capacitance $C_{ion}^{\perp}$, and (b) chemical capacitance C_{chem} of SDC15 as functions of oxygen partial pressure as determined from the measured impedance spectra with temperatures as indicated. Solid lines are a guide for the eyes.

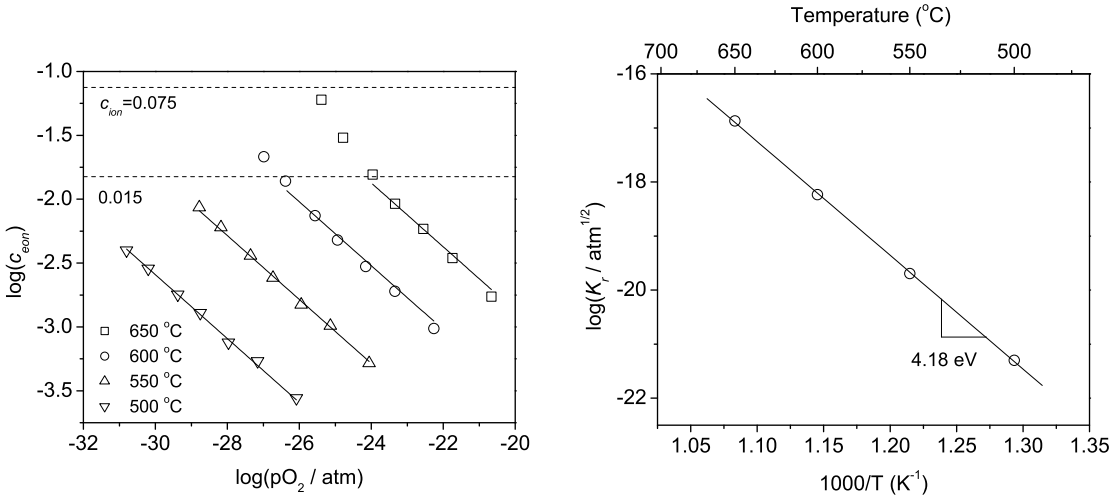

(a) (b)

Figure 3.8: (a) Electron concentration in SDC15 as a function of oxygen partial pressure as determined from the measured impedance spectra with temperatures as indicated. Solid lines are fits of the data to $c_{eon} = (2K_r/c_{AD})^{1/2} p_{O_2}^{-1/4}$. Upper dashed line corresponds to the extrinsic vacancy concentration due to acceptor doping. Lower dashed line corresponds to an electron concentration beyond which the approximation $2c_{ion} = c_{AD} \gg c_{eon}$ is no longer valid. (b) Equilibrium constant for the reduction of SDC15 (1.1) as a function of temperature.

eV and 0.35 ± 0.03 eV for ions and electrons respectively. The results clearly demonstrate that the mixed conducting behavior of doped ceria results from the very high mobility of electronic defects, which are present in much lower concentrations than the ionic defects.

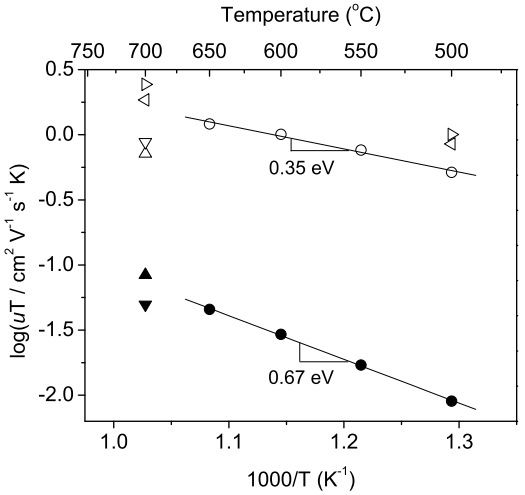

Figure 3.9: Ionic and electronic mobilities as a function of temperature plotted in Arrhenius form. Open symbols are for electronic mobility, whereas closed symbols are for ionic mobility. Symbols ○ and ● are for SDC15 from the current work. Symbol ▷ is for $Gd_{0.1}Ce_{0.9}O_{1.95-\delta}$ (GDC10) from reference.[2] Symbol ◁ is for $Gd_{0.2}Ce_{0.8}O_{1.9-\delta}$ (GDC20) from reference.[2] Symbols △ and ▲ are for GDC10 from reference.[3] Symbols ▽ and ▼ are for GDC20 from reference.[3]

The oxygen partial pressure dependence of $1/\rho^{\perp}_{\mathrm{Pt}}$ in the two regimes is summarized in Figure 3.10(b) and 3.10(c). Under the more oxidizing conditions of the ionic regime, the slope of log $1/\rho^{\perp}_{\mathrm{Pt}}$ vs. log p_{O_2} changes, even changing sign, decreasing from 0.19 at 650 °C to −0.11 at 500 °C. In contrast, under more reducing conditions, a $-1/4$ power law dependence is observed. Fitting the area specific electrode polarization resistivity to $1/\rho^{\perp}_{\mathrm{Pt}} = 1/\rho^{\perp}_{\mathrm{Pt},0} p_{O_2}^{-1/4}$, yields an associated activation energy for the electrode process of 2.75 ± 0.11 eV, Figure 3.10(d). It is noteworthy that Sprague *et al.* similarly observed a $p_{O_2}^{-1/4}$ dependence for the Pt electrode conductivity on mixed conducting $(Gd_{0.98}Ca_{0.02})_2Ti_2O_7$ in CO/CO_2 atmospheres, however, a $p_{O_2}^{-1/6}$ dependence was obtained from $(Gd_{0.9}Ca_{0.1})_2Ti_2O_7$.[60]

Overall, the quality of the fits of the data to the Jamnik-Maier model, (2.168), presented here are significantly better than those reported by Atkinson *et al.* in their study of $Pt|Gd_{0.1}Ce_{0.9}O_{1.95-\delta}$(GDC10)|Pt.[61] These researchers investigated ceria under air and

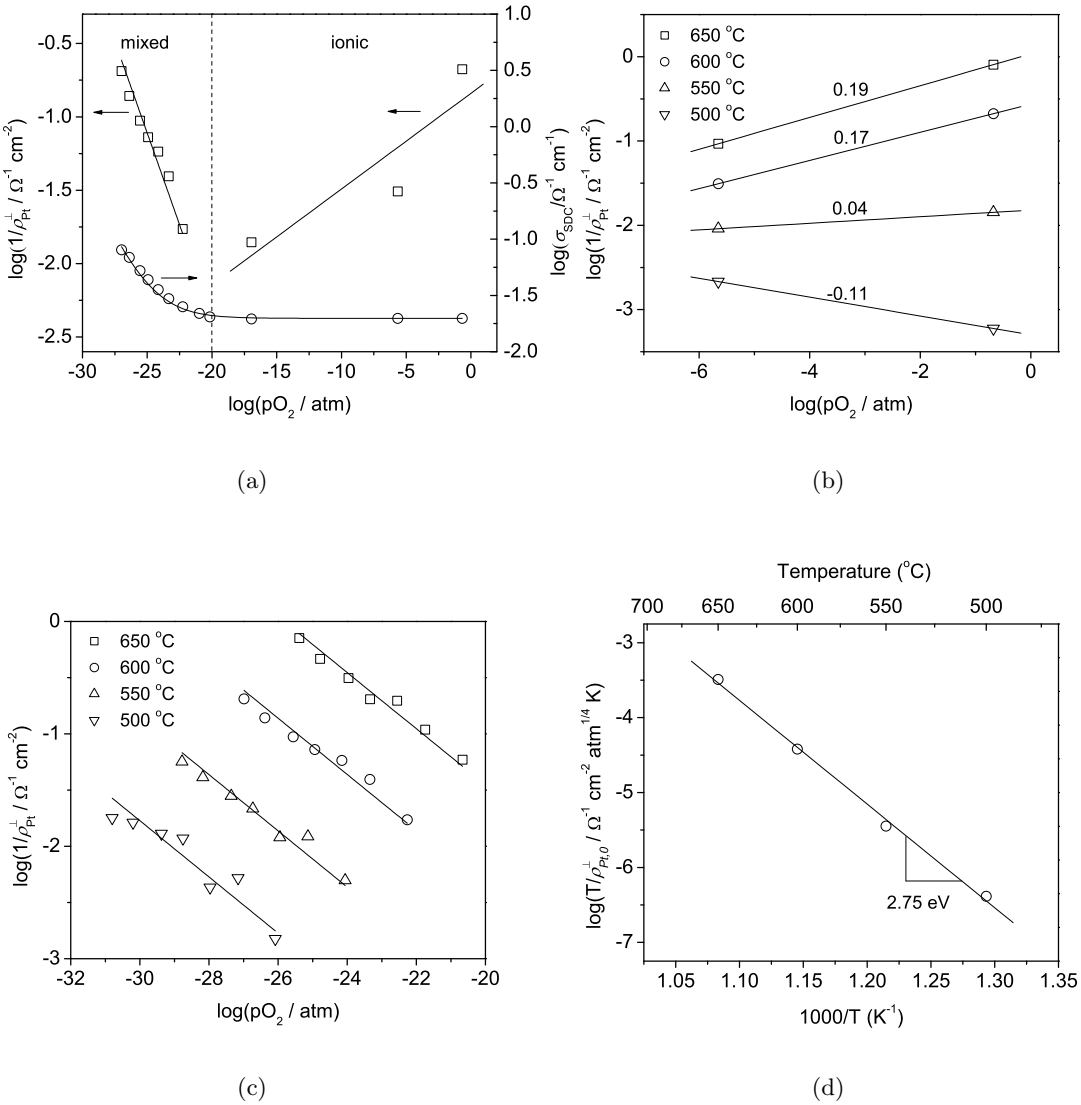

Figure 3.10: (a) Comparison of the electrolyte conductivity and inverse of the electrode area specific polarization resistivity in Pt|SDC15|Pt at 600 °C as a function of oxygen partial pressure. Solid lines show the best fits to equations given below. (b) Area specific electrode polarization conductivity of Pt|SDC15|Pt as a function of oxygen partial pressure and temperature in the pure ionic region. Solid lines are linear regression fits to the data, with the slopes as indicated. (c) Area specific electrode polarization conductivity of Pt|SDC15|Pt as a function of oxygen partial pressure and temperature in the mixed conducting region. Solid lines show the fits to $1/\rho^{\perp}_{\mathrm{Pt}} = 1/\rho^{\perp}_{\mathrm{Pt},0} p_{O_2}^{-1/4}$. (d) Inverse of the oxygen partial pressure independent term in the electrode specific resistivity of the Pt|SDC15|Pt system as a function of temperature. Data plotted in Arrhenius form.

under hydrogen, with the stated goal of evaluating the validity of the Jamnik-Maier model. In addition, sample thickness was varied so as to manipulate C_{chem} according to (2.166). The general observations of those authors are consistent with the results presented here. Under the electrolytic regime, the electrode arc of the Pt|GDC10|Pt system was found to be semicircular in shape whereas it exhibited a half-tear-drop shape under reducing conditions. Furthermore, the derived electrode resistivity under reducing conditions reported by Atkinson is reasonably comparable to that measured here ($\sim$30 Ω cm^2 vs. $\sim$84 Ω cm^2 in the present study at T $\sim$500 °C and a 10% H_2 atmosphere). The poorer quality of the fit of their data to the Jamnik-Maier model is (as pointed out by those authors) most likely due to the fact that several materials parameters for GDC10 were taken from the literature rather than being adjusted to improve the fit, a procedure which would not have been justified given the limited data. Moreover, most of the measurements of Atkinson were performed at relatively low temperatures at which complications due to grain boundary effects arise and the electrode resistance can become excessively large. While quantitative results could not be obtained because of these shortcomings, the qualitative features reported for Pt|GDC10|Pt are entirely in agreement with the observations made here on the Pt|SDC15|Pt system. Finally, it is noteworthy that Jasinski *et al.* similarly obtained asymmetric low-frequency arcs from mixed conducting, undoped ceria placed between gold electrodes.[62] Overall, the present analysis is the first demonstration that detailed quantitative thermodynamic and electrochemical properties can be obtained from the fitting of impedance spectra to physically based models.

3.3 System II

It is generally observed that the impedance spectra change with materials processing conditions such as sintering temperature and time. For example, the impedance spectra collected at around 250 °C in air for SDC15 sintered at different temperatures (1350, 1450 and 1550 °C) and time (5, 15 and 25 hours) are shown in Figure 3.11. Apparently, there are three arcs corresponding to the grain interior, grain boundary and electrode arcs respectively as shown in Figure 2.10. It can be seen that the grain boundary arc increases with sintering

time for samples sintered at 1350 and 1450 °C while it decreases with sintering time for the sample sintered at 1550 °C. Sample sintered at 1350 °C for 5 hours (system I) has the smallest arc while the sample sintered at 1550 °C for 5 hours (system II) has the largest arc. As discussed in Chapter 2, the grain boundary arc is caused by the space charge effect. Thus the samples in systems I and II represent the smallest and the largest space charge effect respectively and that is why these two samples were selected for the current study. While it is still not clear how the processing conditions influence the space charge effect mechanistically, the current investigation is a first step toward this understanding. From the viewpoint of application of ceria in fuel cells, the total conductivity, including both the grain interior and grain boundary, is the determining factor. The higher the total conductivity, the higher the power density. The total conductivity of the sample in system I is four times that of the sample in system II at 600 °C, *i.e.*, the fuel cell operating temperature. Thus the study of space charge effect also has significant technical consequence.

3.3.1 Impedance Spectra and Data Analysis Procedures

Typical impedance spectra obtained from system II are presented in Figure 3.12. The data were collected at 600 °C at several different oxygen partial pressures. Compared with spectra from system I, Figure 3.3, it is immediately noticeable that the low-frequency arcs have the similar behaviors in both systems, *i.e.*, symmetrically depressed arc in oxidizing conditions and asymmetrical Warburg arc in reducing conditions. The difference is that an additional depressed arc appears at higher frequencies in both oxidizing and reducing conditions. This arc corresponds to the high-frequency space charge arc in Figure 2.10. Also compared with Figure 2.10, the grain interior arc is not observed in the present work. This is due to the inductance effect of the experimental setup. As mentioned before, the inductance is measured from blank tests and an inductor with this inductance value is put in series with the circuits used below. For the space charge arc in Figure 3.12(b), the high-frequency intercept with the real axis decreases with decreasing oxygen partial pressure, suggesting mixed conducting behavior. It is also worth noting that this space charge arc becomes smaller with decreasing oxygen partial pressure, just like the low-frequency arc.

As discussed in Chapter 2, for system II, the steady-state solution in the electrolyte is

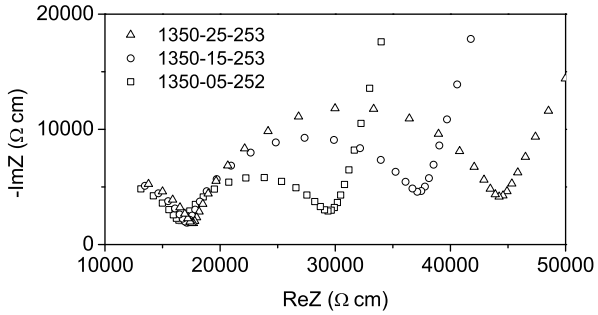

(a)

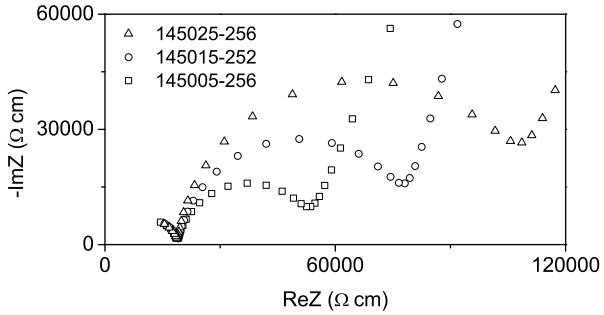

(b)

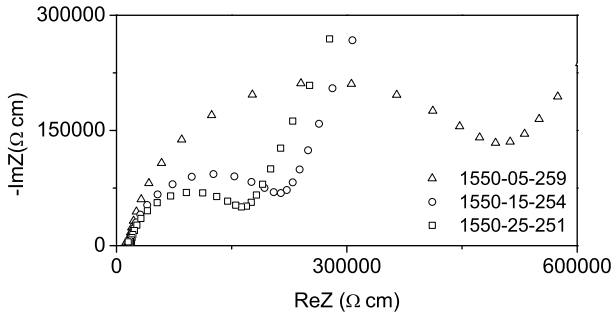

(c)

Figure 3.11: Impedance spectra collected at around 250 °C in air for SDC15 sintered at different temperatures (1350, 1450 and 1550 °C) and time (5, 15 and 25 hours). The first number in the notation gives the sintering temperature, the second number gives the sintering time and the third number gives the measurement temperature.

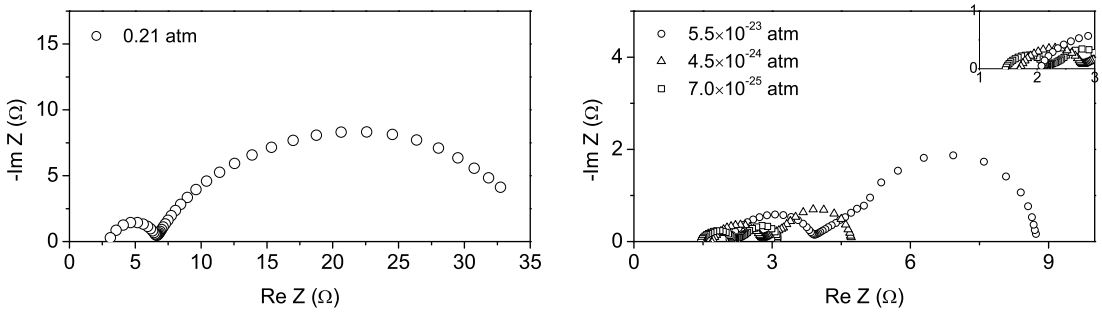

(a) (b)

Figure 3.12: Measured impedance response of Pt|SDC15|Pt at 600 °C under (a) air and (b) reducing conditions where ceria is a mixed conductor.

given in (2.56) and (2.57) for grain interior region, along with (2.63) and (2.64) for space charge region. The small-signal solution is described by the equivalent circuit is Figure 2.6 and there is only numerical solution to the impedance. For both the steady-state and small-signal solutions, the relevant eight parameters are ionic concentration c_{ion}^{∞}, electronic concentration c_{eon}^{∞}, ionic mobility u_{ion}, electronic mobility u_{eon}, space charge potential ϕ_0, dielectric constant ϵ_r, interfacial electrode resistance $R_{ion}^{\perp}$ and interfacial capacitance $C_{ion}^{\perp}$. Again, c_{ion}^{∞} is immediately given from c_{AD}, (2.56).

Under oxidizing conditions, two different methods were used to fit the impedance spectra. In the first method, similar to system I, the impedance spectra were fitted by an empirical equivalent circuit $R_{GI} - R_{GB}Q_{GB} - R_{ion}^{\perp}Q_{ion}^{\perp}$. This is called the Empirical Equivalent Circuit (EEC) method. The ionic conductivity σ_{ion}^{∞} and hence ionic mobility u_{ion} can be obtained from R_{GI}. The space charge potential ϕ_0 is obtained from (2.197). Interfacial capacitance is obtained from $R_{ion}^{\perp}$ and $Q_{ion}^{\perp}$. Alternatively, the equivalent circuit in Figure 2.6 can also be used to fit the whole spectra. This is called the Physical Equivalent Circuit (PEC) method. Also similar to system I, due to the inhomogeneity of the electrode, $C_{ion}^{\perp}$ in Figure 2.6 is first replaced by the constant phase element $Q_{ion}^{\perp}$ and then converted to $C_{ion}^{\perp}$ according to (1.67). The fitting parameters are u_{ion}, ϕ_0, ϵ_r, $R_{ion}^{\perp}$ and $Q_{ion}^{\perp}$.

Under reducing conditions, the values obtained for u_{ion} and $C_{ion}^{\perp}$ in oxidizing conditions from PEC method and u_{eon} from system I are used as fixed parameters in the analysis of the experimental spectra. Thus there are three fitting parameters—c_{eon}^{∞}, ϕ_0 and $R_{ion}^{\perp}$.

The volume elements were built as follows. The space charge region of width λ_{SC} was divided to 100 uniform elements and the grain interior region of width $D - 2\lambda_{SC}$ was divided intto 200 uniform elements. Then the 400 elements were repeated N times. N is the number of serial layers and is related to D by $L = ND$. The convergence has been found for this choice of elements. The calculation of the impedance, *i.e.*, the solution of the matrix equation (2.137), was obtained using the sparse matrix direct solver SuperLU 3.0.[63] The fitting was performed by the Levenberg-Marquardt program levmar 2.1.3.[18] Both SuperLU and levmar were incorporated into the main program written in C.

3.3.2 Derived Results

A comparison of experimental and fitted spectra in air by the two methods, EEC and PEC, is given in Figure 3.13. The Arrhenius plots of ionic conductivities obtained from these two methods are shown in Figure 3.14(a) along with data from the sample without the space charge, system I. For system II, the ionic conductivities are slightly higher using the EEC than using PEC. The activation energies are 0.66 ± 0.01 eV and 0.65 ± 0.01 eV respectively. The conductivity from PEC in system II is comparable to that of system I and the activation energies are 0.67 ± 0.01 and 0.65 ± 0.01 eV respectively. The space charge potentials obtained using these two methods are shown in Figure 3.14(b). The space charge potentials obtained by the two methods are close to each other. Finally, the temperature dependence of dielectric constants is shown in Figure 3.15. The values are very close to 11 given in the literature.[5]

The comparison of measured and fitted impedance spectra using the PEC model at 600 °C and 5.5×10^{-23} atm, under reducing conditions, is shown in Figure 3.16. Again, the fit is reasonably good. However, there is still some difference between the experimental and fitted spectra. First, the fitted high-frequency arc is asymmetric while the experimental high-frequency arc is symmetric. Second, there appears to be some mismatch at the high-frequency region of the Warburg arc. Although for simplicity, both the space charge potentials ϕ_0 and the grain sizes D are taken to be the same among different grains or serial layers, some distribution might exist for these two parameters and this can explain the difference between the measured and fitted spectra. Some simple simulations can be

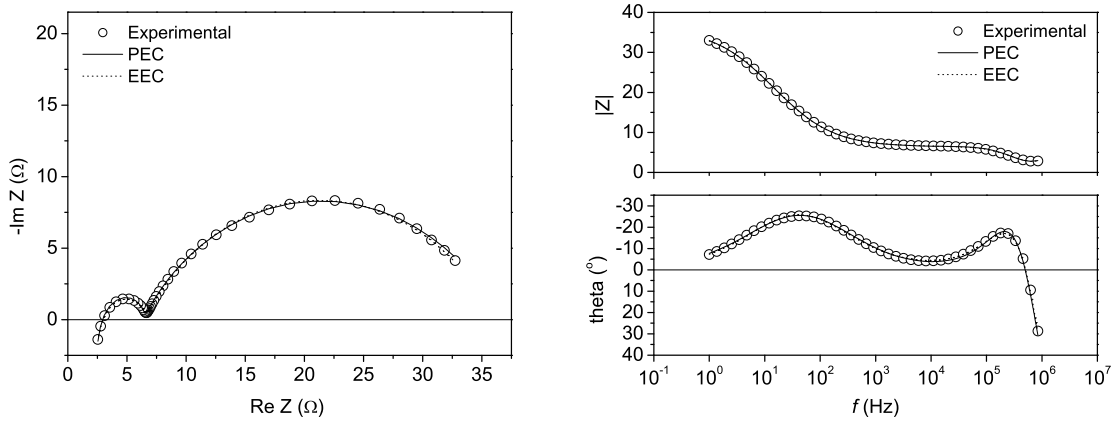

(a) (b)

Figure 3.13: Comparison of the measured and fitted impedance obtained from the Pt|SDC|Pt system at 600 °C in air. The dotted line is the fit to the Empirical Equivalent Circuit (EEC) model $R_{GI} - R_{GB}Q_{GB} - R^{\perp}_{ion}Q^{\perp}_{ion}$ and the solid line is the fit to the Physical Equivalent Circuit (PEC) respectively. (a) Nyquist representation, and (b) Bode-Bode representation.

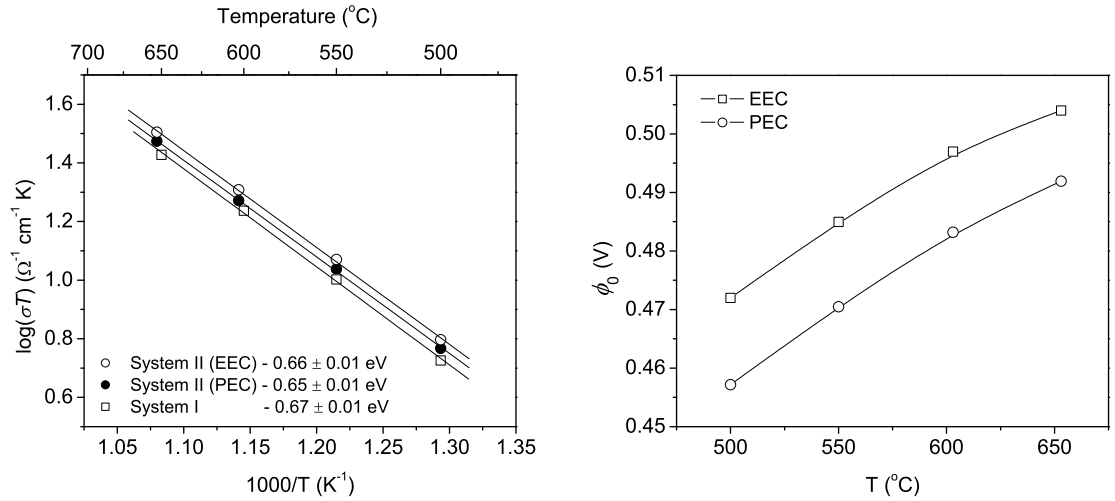

(a) (b)

Figure 3.14: (a) Arrhenius plot of ionic conductivities using EEC and PEC methods for system II, along with data for system I. (b) Space charge potentials in air ϕ_0 using EEC and PEC methods for system II. Solid lines in (b) are a guide for the eyes.

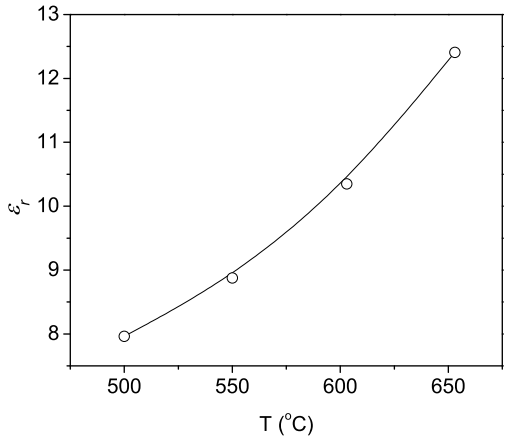

Figure 3.15: Temperature dependence of dielectric constants of ceria in system II by the PEC model. The solid line is a guide for the eyes.

performed to elaborate this. First, a simulation was performed for a space charge potential of 0.46 V for 100 uniform serial layers. Thus the layer width is 6.5 um. Second, the space charge potential was assumed to obey the lognormal distribution with a standard deviation of 10% of the logarithm of the average value. In other words, 100 random numbers obeying the lognormal distribution were generated for the average value of 0.46 V. The serial layer width was kept the same for all layers. Third, the grain size was assumed to be obeying the lognormal distribution with a standard deviation of 30% of the average value. Again, 100 random numbers obeying the lognormal distribution were generated for the average value of 6.5 um. The calculated impedance spectra are shown in Figure 3.17 for comparison. It is obvious that the space charge potential has a larger influence than the grain size. For the space charge potential, the distribution causes some frequency dispersion in both arcs and every arc seems to be separated to two smaller arcs. For the grain size distribution, there is almost no difference in the Warburg arc while the grain boundary arc appears to be more symmetrical. If both the space charge potential and grain size distribution are considered, the difference between the experimental and fitted spectra can be accounted for. Finally, at high temperatures and low oxygen partial pressures, there is a lot of noise in the experimental spectra, which makes the fitting difficult. Thus these spectra are not used.

The dependence of the space charge potential ϕ_0 under reducing conditions is shown in

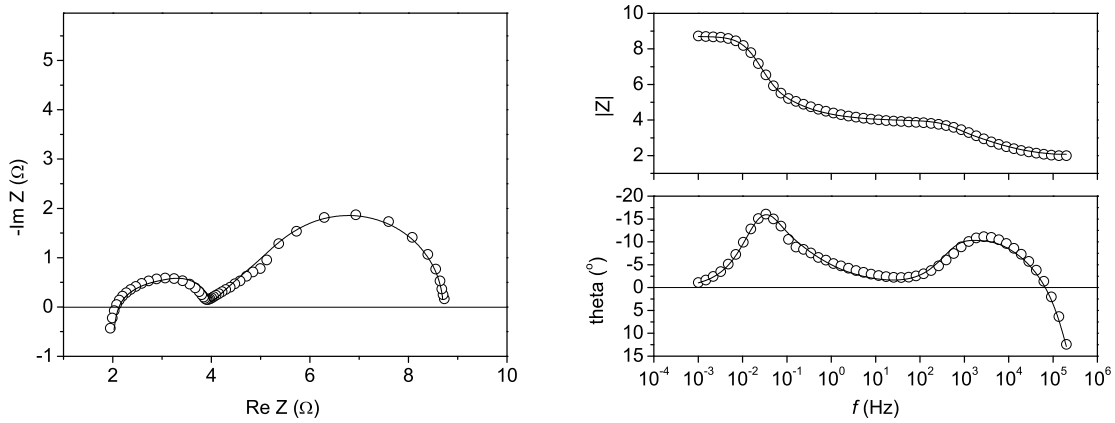

(a) (b)

Figure 3.16: Comparisons of the measured and fit impedance obtained from the Pt|SDC|Pt system at 600 °C and an oxygen partial pressure of 5.5×10^{-23} atm. The fit is to the PEC model. (a) Nyquist representation, and (b) Bode-Bode representation.

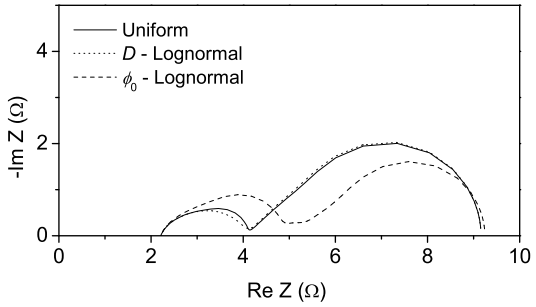

Figure 3.17: Simulation of the effect of the lognormal distribution of the space charge potential and grain size.

Figure 3.18. The space charge potential increases with increasing oxygen partial pressure. The values are comparable to those under oxidizing conditions.

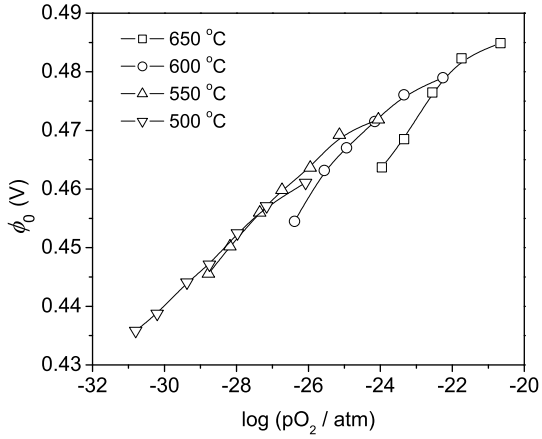

Figure 3.18: Space charge potentials as a function of oxygen partial pressure and temperature in the mixed conducting region. The solid line is a guide for the eyes.

The dependence of electronic concentration c_{eon}^{∞} on the oxygen partial pressure is shown in Figure 3.19(a) in closed symbols. Like the system I (open symbols), c_{eon}^{∞} obeys a clear $-1/4$ power law dependence on oxygen partial pressure over the entire p_{O_2} range examined. Fitting c_{eon}^{∞} to (2.57), one obtains the equilibrium constant, K_r, as a function of temperature, Figure 3.19(b). From these data, the reduction entropy ΔS_r and enthalpy ΔH_r are derived to be $(1.25 \pm 0.03)\times 10^{-3}$ eV/K and 4.24 ± 0.03 eV, respectively. The reduction entropy ΔS_r and enthalpy ΔH_r of system I are 1.18×10^{-3} eV/K and 4.18 eV respectively. Coincidentally, the experimental conditions with very noisy impedance spectra are also those above the lower dashed line in Figure 3.19(a).

Turning to the electrode behavior, the oxygen partial pressure dependence of the electrode polarization "conductivity" (inverse of $1/\rho_{\mathrm{Pt}}^{\perp}$), $\rho_{\mathrm{Pt}}^{\perp} = R_{ion}^{\perp} A$, is shown in Figure 3.20(a) in closed symbols. Again, the data from system I are also shown in open symbols for comparison. It can be seen at all investigated tempertures, a $-1/4$ power law dependence is clearly observed. Fitting the area specific electrode resistivity to $1/\rho_{\mathrm{Pt}}^{\perp} = 1/\rho_{\mathrm{Pt},0}^{\perp} p_{O_2}^{-1/4}$ yields an associated activation energy for the electrode process of 2.40 ± 0.06 eV, Figure 3.20(b).

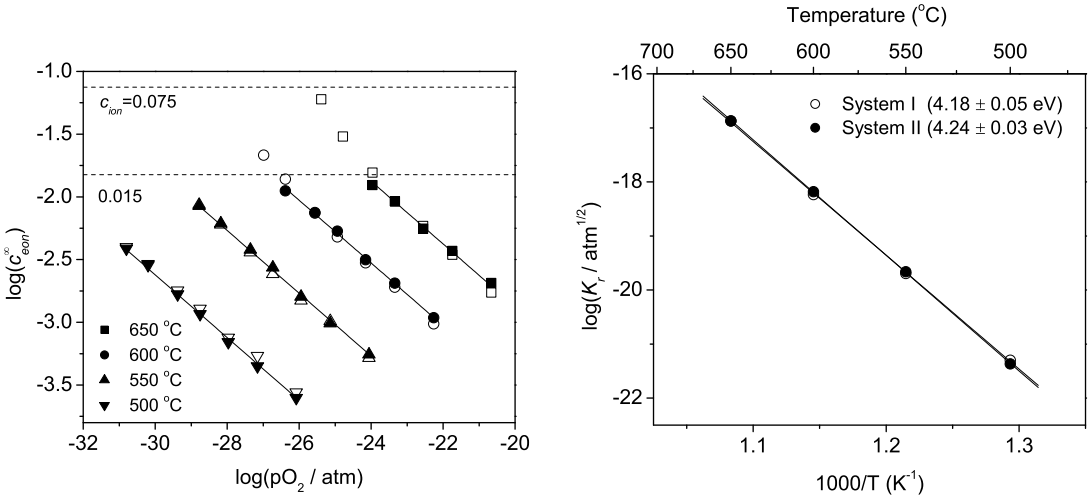

(a) (b)

Figure 3.19: (a) Electron concentration in SDC15 as a function of oxygen partial pressure as determined from the measured impedance spectra with temperatures as indicated. Closed and open symbols are for system II and system I respectively. Solid lines are fits of the data to $c^{\infty}_{eon} = (2K_r/c_{AD})^{1/2}\, p_{O_2}^{-1/4}$. Upper dashed line corresponds to the extrinsic vacancy concentration due to acceptor doping. Lower dashed line corresponds to an electron concentration beyond which the approximation $2c^{\infty}_{ion} = c_{AD} \gg c^{\infty}_{eon}$ is no longer valid. (b) Equilibrium constant for the reduction of SDC15 as a function of temperature. Closed and open symbols are for system II and system I respectively.

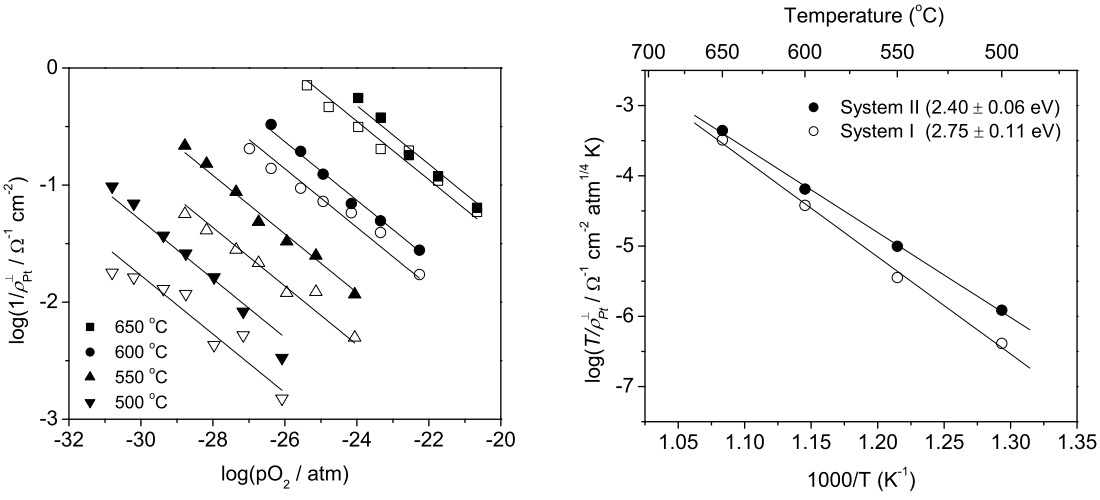

(a) (b)

Figure 3.20: (a) Area specific electrode polarization conductivity of Pt|SDC15|Pt as a function of oxygen partial pressure and temperature in the mixed conducting region. Closed and open symbols are for system II and system I respectively. Solid lines show the fits to $1/\rho^{\perp}_{\mathrm{Pt}} = 1/\rho^{\perp}_{\mathrm{Pt},0} p_{O_2}^{-1/4}$. (d) Inverse of the oxygen partial pressure independent term in the electrode specific resistivity of the Pt|SDC15|Pt system as a function of temperature. Closed and open symbols are for system II and system I respectively. Data plotted in Arrhenius form.

3.4 System III

3.4.1 Impedance Spectra and Data Analysis Procedures

Typical impedance spectra obtained from system III are presented in Figure 3.21. The data were collected at 600 °C at several different oxygen partial pressures. Under oxidizing conditions, Figure 3.21(a), there is only one depressed arc as in Figure 3.3(a) of system I. Under reducing conditions, Figure 3.21(b), there are a small arc and a Warburg arc overlapped with each other. The fact that there are two arcs resembles that in Figure 3.12(b) of system II. However, the additional small arc is not due to the space charge because space charge arc is not observable here as in Figure 3.21(a). Since in the present system two electrodes are different, it is hypothesized that the additional arc is due to the BSCF cathode. The impedance spectrum of BSCF|SDC15|BSCF at 600 °C in air is shown in Figure 3.22, exhibiting a similar shape and magnitude as those of the small arc in Figure 3.12(b).

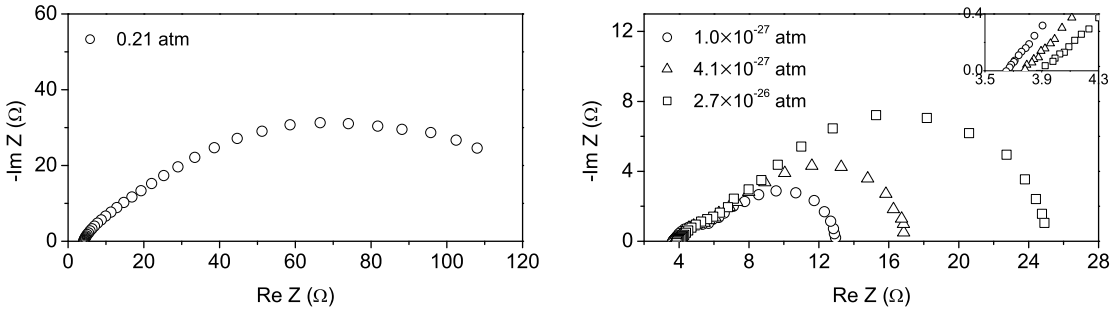

(a) (b)

Figure 3.21: Measured impedance responses of BSCF|SDC15|Pt at 600 °C under (a) air and (b) reducing conditions.

As discussed in Chapter 2, for system III, the steady-state solution is given in (2.35) for the ionic concentration and (2.40) for the electronic concentration. The steady-state open circuit voltage is given by (2.95). The small-signal solution is described by the equivalent circuit is Figure 2.5 and there is only numerical solution to the impedance. For both the steady-state and small-signal solutions, the relevant twelve parameters are the ionic concentration c_{ion}, equilibrium constant K_r, ionic mobility u_{ion}, electronic mobility u_{eon}, open circuit voltage V_{oc}, interfacial oxygen partial pressures $p_{O_2}(0)$ and $p_{O_2}(L)$, interfacial an-

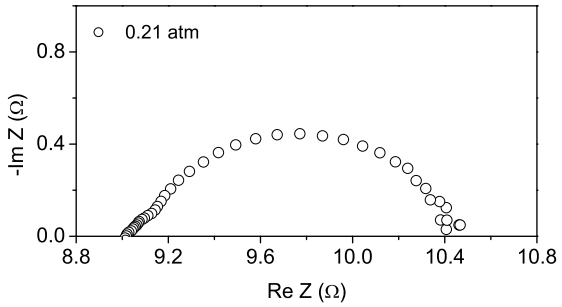

Figure 3.22: Measured impedance responses of BSCF|SDC15|BSCF under air.

ode resistance $R^{\perp}_{ion}(a)$, interfacial cathode resistance $R^{\perp}_{ion}(c)$, interfacial anode capacitance $C^{\perp}_{ion}(a)$, interfacial cathode capacitance $C^{\perp}_{ion}(c)$ and effective conducting area A. A was listed here because the electrode area 0.71 cm^2 is smaller than the electrolyte area 1.33 cm^2. c_{ion} is given from c_{AD}, (2.35). Since the BSCF electrode resistance in Figure 3.22 is small, it is assumed here the oxygen partial pressure drop across the cathode is negligible. In other words, $p_{O_2}(L) = p_{O_2}(c)$. $p_{O_2}(0)$ and $p_{O_2}(L)$ are related to V_{oc} by (2.95).

Under oxidizing conditions, as in system I, R_{ion} was obtained from the high-frequency intercept of the real axis. The effective conducting area is calculated based on the present R_{ion} and the ionic conductivity from system I. The calculated areas are 0.84, 0.78 and 0.69 cm^2 respectively. Since c_{ion} is known, u_{ion} can be obtained.

Under reducing conditions, the values obtained for u_{ion} in oxidizing conditions, along with $C^{\perp}_{ion}(a)$, u_{eon} and K_r from system I were also used as fixed parameters in the analysis of the experimental spectra. Thus there are four fitting parameters—$R^{\perp}_{ion}(a)$, $R^{\perp}_{ion}(c)$, $C^{\perp}_{ion}(c)$ and A.

The volume elements were taken to be uniform and the number of elements was chosen to be 2000 in this work. Convergence has been found for this number. The calculation of the impedance, *i.e.*, the solution of the matrix equation (2.137), was obtained using the sparse matrix direct solver UMFPACK 4.6.[64–67] The fitting was performed by the Levenberg-Marquardt program levmar 2.1.3.[18] Both UMFPACK and levmar were incorporated into the main program written in C.

3.4.2 Derived Results

The comparison of experimental and fitted spectra is given in Figure 3.16 when the H_2 concentration is "100%" with 3% H_2O saturation in the anode and oxygen partial pressure is 0.21 atm in the cathode. The fit is reasonably good. Although the difference could come from multiple sources, the most important contribution is believed to be due to the asymmetry of the electrodes, *i.e.*, the cathode area is smaller than those of the electrolyte and the anode. The experimental open circuit voltages, calculated oxygen partial pressures and all of the fitting results are given in Table 3.1.

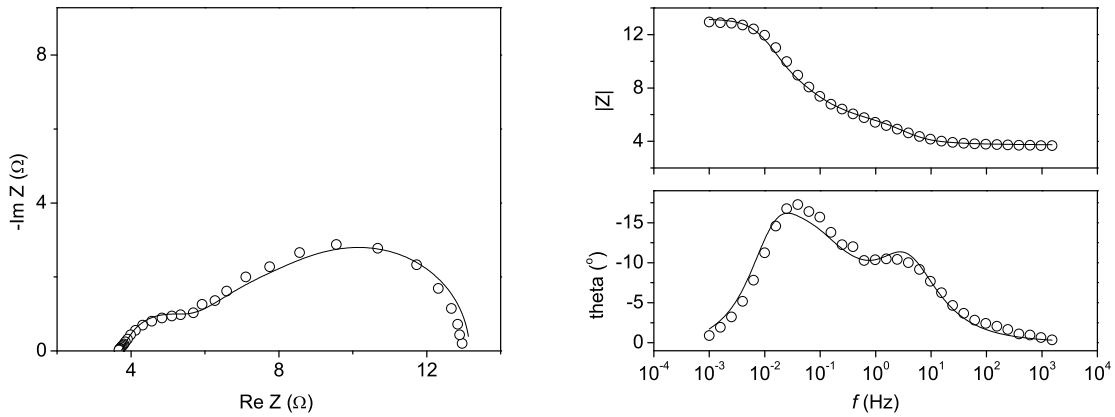

(a) (b)

Figure 3.23: Comparison of the measured and fit impedance obtained from the BSCF|SDC15|Pt system at 600 °C when the H_2 concentration is "100%" with 3% H_2O saturation in the anode and oxygen partial pressure is 0.21 atm in the cathode. (a) Nyquist representation, and (b) Bode-Bode representation.

Table 3.1: Experimental open circuit voltages, calculated oxygen partial pressures, and fitting results

T	V_{oc}	Anode	$p_{O_2}(a)$	$p_{O_2}(0)$	A	$R^{\perp}_{ion}(c)$	$C^{\perp}_{ion}(c)$	$R^{\perp}_{ion}(a)$
°C	V	H_2, %	atm	atm	cm^2	Ω	F	Ω
550	0.911	50	6.634E-29	6.330E-24	0.73	2.009	0.0573	65.024
550	0.928	100	1.661E-29	1.473E-24	0.74	2.322	0.0530	46.416
600	0.854	20	2.747E-26	2.526E-21	0.77	0.685	0.0427	44.561
600	0.881	50	4.117E-27	5.211E-22	0.79	0.973	0.0445	27.788
600	0.899	100	1.031E-27	1.363E-22	0.80	1.143	0.0457	19.196
650	0.824	20	1.096E-24	8.841E-20	0.86	0.201	0.0348	19.937
650	0.851	50	1.643E-25	2.208E-20	0.87	0.257	0.0437	12.421
650	0.867	100	4.113E-26	5.922E-21	0.89	0.294	0.0423	8.884

Nernst, theoretical and experimental voltage values as a function of temperatures for the experiments with "100%" H_2 at the anode are presented in Figure 3.24. As discussed in section 2.2.2, the theoretical potentials are lower than Nernst values at all temperatures due to the mixed conduction at high temperatures under reducing atmospheres. The higher the temperature, the more the mixed conduction and thus the greater the difference. The experimental voltages values are smaller than theoretical ones due to the contributions of electrode polarizations. Similar results were obtained for the experiments with "50%" and "20%" H_2 at the anode.

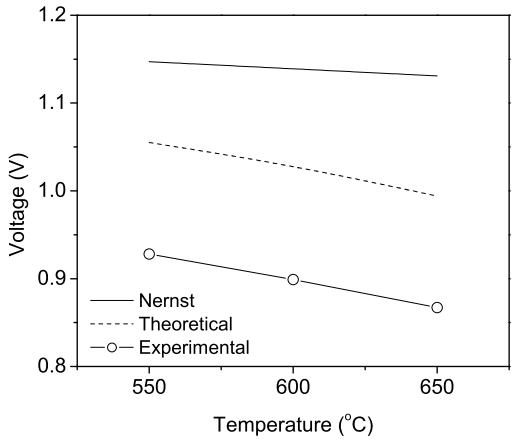

Figure 3.24: Nernst, theoretical and experimental voltage values as a function of temperatures. The cathode gas is 100 sccm air and the anode gas is 50 sccm H_2 saturated with 3% H_2O.

For the oxygen partial pressure gradient, there is a large oxygen partial pressure drop (5 orders of magnitude) across the anode, from $p_{O_2}(0)$ to $p_{O_2}(a)$. The oxygen partial pressure at the anode|electrolyte interface, $p_{O_2}(0)$, is higher when the oxygen partial pressure at the anode chamber $p_{O_2}(a)$ is higher. The oxygen partial pressure profile inside the electrolyte is obtained from (2.48). The oxygen potential profile across the whole sample is shown in Figure 3.25 at 600 °C when the H_2 concentration is "100 %" with 3 % H_2O saturation in the anode and oxygen partial pressure is 0.21 atm in the cathode. Because the thickness of the electrodes is much smaller than the thickness of the electrolyte, a seemingly sharp change appears at the interfaces.

In Table 3.1, the effective conducting areas increase with reducing anode oxygen partial pressure and the values are comparable to those obtained under oxidizing conditions. The

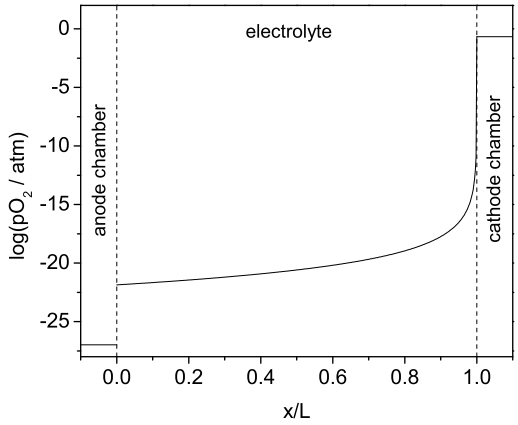

Figure 3.25: Oxygen potential profile of the BSCF|SDC15|Pt system at 600 °C when the H_2 concentration is "100%" with 3% H_2O saturation in the anode and oxygen partial pressure is 0.21 atm in the cathode.

values of interfacial cathode resistance $R^{\perp}_{ion}(c)$ and capacitance $C^{\perp}_{ion}(c)$ are also comparable to those in BSCF|SDC|BSCF under oxidizing conditions (not shown). It is not the goal of this work to investigate the performance of BSCF but from our preliminary work on BSCF|SDC15|BSCF, it is found that the polarization resistance of BSCF|ceria interface decreases with increasing oxygen partial pressures. Thus it is interesting to note that $R^{\perp}_{ion}(c)$ increases with decreasing anode oxygen partial pressures in the present work. Since the cathode oxygen partial pressure is fixed to be 0.21 atm, the decreasing anode oxygen partial pressure would lead to the decrease of the interfacial oxygen partial pressure $p_{O_2}(L)$, although $p_{O_2}(L)$ is approximated to 0.21 atm for simplicity. The decreasing $p_{O_2}(L)$ would increase $R^{\perp}_{ion}(c)$ as expected. An interesting point about this observation is the anode will becomes worse when the cathode becomes better. In principle it is possible to fit $p_{O_2}(L)$ directly instead of fixing it to be the same as $p_{O_2}(c)$, *i.e.*, 0.21 atm. It was found that the fitted value of $p_{O_2}(L)$ is around 0.4 atm, slightly higher than 0.21 atm. While it does not make physical sense to have $p_{O_2}(L)$ larger than $p_{O_2}(c)$, it nevertheless suggests that $p_{O_2}(L)$ is close to $p_{O_2}(c)$. Along with the small $R^{\perp}_{ion}(c)$ and reasonably good fitting shown above, $p_{O_2}(L)$ can be safely assumed to be the same as $p_{O_2}(c)$.

A direct comparison of the anode polarization resistance $R^{\perp}_{ion}(a)$ at the Pt|SDC15 interface obtained here with that of Pt|SDC15|Pt cells measured under uniform chemical environments, *i.e.*, system I, is presented in Figure 3.26, shown as the inverse of area spe-

cific polarization resistance $\rho^{\perp}_{\mathrm{Pt}} = R^{\perp}_{ion}(a)A$ vs. oxygen partial pressure in log-log form. As mentioned above, there is a large oxygen partial pressure drop across the anode, thus $\rho^{\perp}_{\mathrm{Pt}}$ is plotted against both $p_{O_2}(0)$ (upper-half filled symbols) and $p_{O_2}(a)$ (right-half filled symbols). The values for Pt|SDC15|Pt cells measured under uniform chemical environments are in open symbols. It is immediately evident that the area specific polarization resistances from the two sets of measurements both exhibit a $p_{O_2}^{-1/4}$ dependence. Furthermore, it is found that $\rho^{\perp}_{\mathrm{Pt}}$ is between the corresponding values in Pt|SDC15|Pt cells measured under uniform chemical environments at $p_{O_2}(a)$ and $p_{O_2}(0)$.

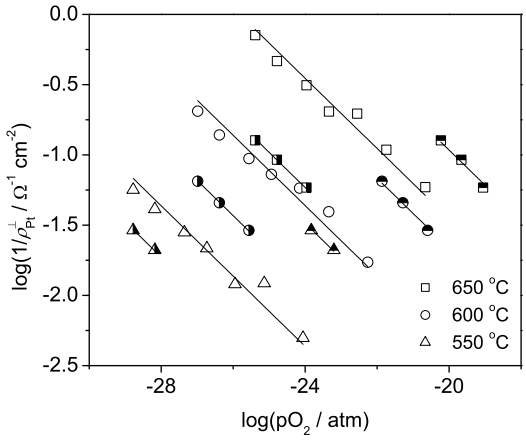

Figure 3.26: Area specific electrode resistivity of Pt|SDC15 interface of BSCF|SDC15|Pt system as a function of oxygen partial pressure and temperature. Open symbols are for system I. Upper-half and right-half filled symbols are plotted against $p_{O_2}(0)$ and $p_{O_2}(a)$ respectively. Solid lines show the fits to $1/\rho^{\perp}_{\mathrm{Pt}} = 1/\rho^{\perp}_{\mathrm{Pt},0} p_{O_2}^{-1/4}$.

3.5 Discussions

3.5.1 Properties of Ceria

The thermodynamic properties measured here for SDC15 by electrochemical methods are in good agreement with those of related materials obtained by thermogravimetric methods. In particular, Kobayashi *et al.*[68] measured ΔS_r and ΔH_r of both $Sm_{0.1}Ce_{0.9}O_{2-\delta}$ (SDC10) and $Sm_{0.2}Ce_{0.8}O_{2-\delta}$ (SDC20). The reported enthalpies are 4.15 eV and 3.99 eV for SDC10 and SDC20, respectively, and the entropies 1.10×10^{-3} eV/K and 1.13×10^{-3} eV/K, respectively. If one assumes a linear dependence of reduction enthalpy and entropy on the dopant level,

then one interpolates values of 4.07 eV and 1.12×10^{-3} eV/K, respectively. These values are very close to 4.18 eV and 1.18×10^{-3} eV/K for system I and 4.24 eV and 1.25×10^{-3} eV/K for system II respectively, determined in this work. These values are listed in Table 3.2 for comparison. Given that the transport equations are derived under the assumption that the processes are not far from equilibrium, agreement between the methods is expected.

Table 3.2: Reduction enthalpies and entropies

Substance	ΔH_r(eV)	$\Delta S_r(\times10^{-3}$ eV/K)
$Sm_{0.1}Ce_{0.9}O_{2-\delta}$ (SDC10)[68]	4.15	1.10
$Sm_{0.2}Ce_{0.8}O_{2-\delta}$ (SDC20)[68]	3.99	1.13
$Sm_{0.15}Ce_{0.85}O_{2-\delta}$ (SDC15)*	4.07	1.12
$Sm_{0.15}Ce_{0.85}O_{2-\delta}$ (SDC15) (System I)	4.18	1.18
$Sm_{0.15}Ce_{0.85}O_{2-\delta}$ (SDC15) (System II)	4.24	1.25

*Interpolated from SDC10 and SDC20.

The mobilities determined here for both ions and electrons in SDC15 are also in good agreement with literature values for related materials, Figure 3.9, as are the corresponding activation energies, Table 3.3. Specifically, the ionic mobility for SDC15 falls, in the present study, between 10^{-5} and 10^{-4} cm^2 V^{-1} s^{-1}) with an activation energy of 0.67 eV. The activation energy for electron motion, 0.35 eV, is two times smaller than for ions, and the absolute mobilities approximately one order of magnitude greater. The relatively low electronic mobility is consistent with the usual interpretation that electron motion in ceria occurs via a small polaron activated hopping process.[69]

Table 3.3: Activation energies for ionic and electronic mobility, and for σ_e^0

Substance	ΔH_i(eV)	ΔH_e(eV)	ΔH_{e0}(eV)
$Sm_{0.15}Ce_{0.85}O_{2-\delta}$ (SDC15) (System I)	0.67	0.35	2.44
$Sm_{0.15}Ce_{0.85}O_{2-\delta}$ (SDC15) (System II)	0.65	-	-
$Sm_{0.2}Ce_{0.8}O_{2-\delta}$ (SDC20)[10]	0.68*	-	2.30*
$Sm_{0.2}Ce_{0.8}O_{2-\delta}$ (SDC20)[70]	-	-	2.22
$Gd_{0.1}Ce_{0.9}O_{2-\delta}$ (GDC10)[2]	0.64	0.25	-
$Gd_{0.2}Ce_{0.8}O_{2-\delta}$ (GDC20)[3]	0.71	0.52	-

*Fitted with given σ_i and σ_e^0 in reference.[10]

Up to now, the investigation of grain boundary behavior of MIECs have mainly been limited to the oxidizing conditions, *i.e.*, the MIEC being a pure ionic conductor. In the studies of space charge regions of ceria under oxidizing conditions, it is generally found that space charge potential increases with increasing temperatures.[71] The same temperature de-

pendence has been observed in Figure 3.14(b). The values of space charge potential ϕ_0 at 500 °C in oxidizing conditions for ceria with different compositions are listed in Table 3.4 for comparison. The space charge potential ϕ_0 obtained from system II at 500 °C using Empirical Equivalent Circuit modeling is around 0.47 V while ϕ_0 is around 0.46 V using the Physical Equivalent Circuit modeling (PEC). Both of these two values fall into the range of literature values. It is worth mentioning all the literature values were obtained using the Empirical Equivalent Circuit (EEC) modeling. It is also worth noting that it is generally found that the space charge effect becomes smaller with increasing dopant concentration, which roughly agrees with the low value of ϕ_0 here. Under reducing conditions, the space charge potential decreases with decreasing oxygen partial pressures as shown in Figure 3.18 and the values of space charge potentials are comparable to those obtained in oxidizing conditions. Considering the various approximations of the present model, such as one-dimensional transport and Mott-Schottky space charge model *etc.*, no mechanistic explanation of the temperature and oxygen partial pressure dependence of the space charge potential has been given at this stage. There is also no literature values available for the space charge potential of ceria under reducing conditions.

Table 3.4: Space charge potential ϕ_0 at 500 °C under oxidizing conditions

Substance	ϕ_0(eV)
$Gd_{0.0005}Ce_{0.9995}O_{2-\delta}$ [72]	∼0.7
$Y_{0.02}Ce_{0.98}O_{2-\delta}$ (YDC02) [71]	∼0.5
$Sm_{0.15}Ce_{0.85}O_{2-\delta}$ (SDC15) (System II, EEC)	∼0.47
$Sm_{0.15}Ce_{0.85}O_{2-\delta}$ (SDC15) (System II, PEC)	∼0.46
$Y_{0.2}Ce_{0.8}O_{2-\delta}$ (YDC20) [71]	∼0.4

Overall, the correspondence between literature values of both the thermodynamic and transport properties of SDC15 and the values measured here by A.C. impedance spectroscopy provides strong validation of the physical equivalent circuit model for the impedance response of mixed conductors.

3.5.2 Electrochemistry of the Pt|Ceria System

Two possible electrochemical reactions can be considered to take place on Pt under the experimental conditions employed in this work. Under moderately oxidizing atmospheres

(oxygen partial pressures of 10^{-6} to 1 atm), the oxidation/reduction of oxygen can be described globally via reaction (3.1)

$$1/2O_2 + 2e^- \leftrightarrow O^{2-} \tag{3.1}$$

Under more reducing conditions, achieved via introduction of hydrogen to the sample atmosphere, oxidation/reduction could, in principle, also occur via reaction (3.1), and then be followed by gas phase reaction between H_2 and O_2 to maintain overall equilibrium between the three gaseous species (H_2, O_2 and H_2O). However, more likely is the reaction directly involving all three species, reaction (3.2)

$$H_2 + O^{2-} \leftrightarrow H_2O + 2e^- \tag{3.2}$$

These two sets of conditions (moderate and reducing atmospheres) and corresponding electrochemical reactions, (3.1) and (3.2) respectively, are considered separately.

The kinetics and mechanistic pathways of reaction (3.1) have been studied extensively in the Pt|YSZ|Pt system.[73] There is general consensus that the overall reaction rate is limited by the rate of arrival of oxygen atoms to the reaction sites at the Pt|YSZ interface. According to the model proposed by Mizusaki *et al.*,[74] at high temperatures and low oxygen partial pressures, the surface diffusion of absorbed oxygen atoms on Pt is the rate limiting step and gives rise to a characteristic p_{O_2} dependence of the electrode resistance, obeying a $p_{O_2}^{-1/2}$ dependence at low oxygen partial pressures and a $p_{O_2}^{1/2}$ dependence at high oxygen partial pressures. Thus, the electrode "conductivity" first increases then decreases, taking on a peak value at some intermediate pressure, $p^*_{O_2}$, which corresponds to the pressure at which the Pt coverage by oxygen atoms is 1/2. The position of the peak is temperature dependent, moving to lower p_{O_2} values as temperature is decreased.[74, 75] At low temperatures, the surface diffusion of oxygen becomes exceedingly slow and dissociative adsorption of oxygen directly at the reaction sites becomes the rate-limiting step, resulting in an electrode resistance that is independent of p_{O_2}. A transition between these two types of behavior is evident at intermediate temperatures.[74] A related model has been proposed by Robertson and Michaels[76] and discussed further by Adler.[73] In this case, both surface diffusion

and dissociative adsorption simultaneously control the overall kinetics at all temperatures, and there is no single rate-limiting step for the behavior of the electrode. An explicit p_{O_2} dependence for the electrode properties has not been derived for this model.

Because SDC15 as measured here behaves as a pure ionic conductor at moderate oxygen partial pressures, it is likely that the electrochemical reduction of O_2 in the Pt|SDC15|Pt system occurs by a mechanism similar to that of the Pt|YSZ|Pt system. Although the limited data precludes definitive conclusions, the trend evident in Figure 3.10(b), that of a decreasing slope with decreasing temperature, is consistent with the model described above. The data imply that $p^*_{O_2}$ is greater than 0.21 atm at 650 °C and less than 10^{-6} atm at 500 °C, not unreasonable values in comparison to those reported for YSZ.[77] In addition, the SDC system examined here is similar to YSZ[75, 78] in that both show only one electrode-related arc with symmetric, semicircular appearance in their respective impedance spectra, further supporting the conclusion that the mechanisms must be similar. That the absolute magnitude of the area specific electrode resistance measured here, approximately 5 Ω cm^2 at 600 °C, is much lower than that reported for Pt|YSZ,[75, 78] approximately 500 Ω cm^2, is likely due to differences in Pt microstructure that influence the diffusion length and density of reaction sites. More importantly, it likely due to the higher ionic conductivity of ceria compared to that of YSZ at this temperature.

Alternatively, one cannot rule out the possibility that the charge transfer reaction, in which adsorbed oxygen atoms on the Pt surface react with electrons and form oxygen ions on the electrolyte surface, is the rate limiting step. Such a mechanism was proposed much earlier from study of polarization phenomenon on Pt|ceria in particular by Wang and Nowick.[79, 80] In this case, a slope of 1/4 is expected at low oxygen partial pressure in a log-log plot of $1/\rho^{\perp}_{\mathrm{Pt}}$ vs. p_{O_2} that gradually shifts to a value of $-1/4$ at high oxygen partial pressure. As pointed out by Mizusaki *et al.*[74] the data presented by Wang and Nowick have not been collected over a sufficiently wide oxygen partial pressure range to distinguish between slopes of $\pm 1/2$ from those of $\pm 1/4$ and conclusively support the charge transfer model. The model that includes adsorption, diffusion and charge transfer was investigated by Mitterdorfer and Gauckler.[81] The authors conclude that above 800 °C and high p_{O_2}, charge transfer is in competition with surface diffusion. With decreased temperature or lower p_{O_2}, the reaction

is limited by adsorption and surface diffusion. Thus, we propose that diffusion/dissociative adsorption of oxygen are the rate limiting steps in the Pt|SDC15|Pt system under oxygen atmospheres, much as is widely accepted for Pt|YSZ|Pt.

In comparison to the behavior of O_2 on Pt, the electrochemistry of the H_2-H_2O system is quite complex because many more active species can be involved in the electrochemical oxidation steps. As a consequence, no real consensus as to the reaction pathway has emerged in the literature, even for Pt|YSZ|Pt. While Mizusaki *et al.*,[82] who observed only one electrode-related arc in their impedance spectra, have suggested that OH group transfer across the Pt|YSZ is rate limiting, several other groups have argued that multiple, serial steps are necessary to describe the reaction on the basis of the observation of multiple (2-3) electrode related responses by impedance spectroscopy. In particular, a high-frequency arc has been attributed to the charge transfer step and a low-frequency arc to hydrogen dissociative adsorption on the Pt surface.[52] As noted in section 2.3.3.3, it is not possible to detect by impedance spectroscopy serial reaction steps at the electrode-sample interface for a sample that is a mixed ionic and electronic conductor with a large value of C_{chem}. Thus, it is not possible to directly establish whether Pt|SDC15|Pt exhibits a single or a multistep mechanism. Nevertheless, from the p_{O_2} dependent behavior of $\rho^{\perp}_{\mathrm{Pt}}$ measured here, Figure 3.10(c), we can immediately conclude that electro-oxidation of hydrogen on Pt|ceria occurs by a fundamentally different mechanism than it does on Pt|zirconia. Indeed, in the case of Pt|YSZ, there is no reason to expect a direct dependence of $\rho^{\perp}_{\mathrm{Pt}}$ on p_{O_2} in the presence of H_2. Instead, because adsorbed hydrogen atoms and hydroxyl groups are presumed to participate in the reaction mechanism, dependencies on p_{H_2} or p_{H_2O} are typically probed (which only depend indirectly on p_{O_2} via the gas phase equilibrium).

The observation here of a power law of $p_{O_2}^{-1/4}$ suggests that the electrode reactions are correlated to the electronic conductivity of mixed conducting ceria, which exhibits precisely the same dependence on oxygen partial pressure. Furthermore, the activation energies of $1/\rho^{\perp}_{\mathrm{Pt},0}$, 2.75 ± 0.11 eV for system I and 2.40 ± 0.06 eV for system II, are very similar to that measured for electronic conductivity of SDC15, 2.44 ± 0.03 eV. Based on these observations we propose that the electrochemical reaction 3.2 can occur via two parallel paths on oxygen ion conducting materials, Figure 3.27. In the first path, dissociative hydrogen

desorption occurs on the Pt surface, followed by migration of protons to the Pt|oxide interface and subsequent electrochemical reaction. In the second path, hydrogen desorption occurs directly on the oxide surface which subsequently reacts electrochemically with oxygen, giving up electrons which are then transported through the oxide to the Pt. Given the very low electronic conductivity of zirconia, the second pathway is not available for this electrolyte and the reaction is taken to occur via the first path, with the exact rate-limiting step yet to be determined. In the case of ceria, we propose that although the first path is probably fast, the second path is faster. That is, we propose that the electrochemical reaction occurs directly on the ceria surface (*i.e.*, that ceria is electrochemically active), and that the reaction is limited by the rate of removal of electrons from the reaction sites (*i.e.*, electronic conductivity).

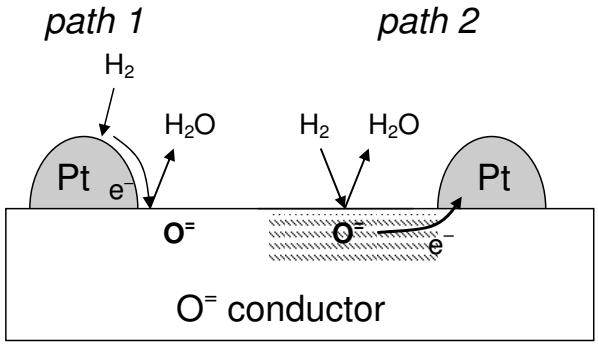

Figure 3.27: Schematic diagram showing the hydrogen electro-oxidation pathways (left) on Pt|YSZ and (right) Pt|SDC.

3.6 Summary and Conclusions

A rigorous derivation of the A.C. impedance of mixed conducting materials has been presented for both equilibrium and nonequilibrium conditions.

Using p_{O_2}|Pt|$Sm_{0.15}Ce_{0.85}O_{1.925-\delta}$(1350 °C)|Pt|$p_{O_2}$ (system I) and p_{O_2}|Pt|$Sm_{0.15}Ce_{0.85}O_{1.925-\delta}$(1550 °C)|Pt|$p_{O_2}$ (system II) as model systems, it is demonstrated that the impedance data yield a broad range of electrical and electrochemical properties of the mixed conductors. In particular, the concentration of free electron carriers, the mobilities and activation energies for both ion and electron transport, the space charge potential, and the entropy and enthalpy of reduction of Ce^{4+} to Ce^{3+} have all been measured. The values

are in good agreement with what would be expected based on the reported properties of Sm and Gd doped ceria with differing compositions. The oxygen electro-reduction reaction on Pt|$Sm_{0.15}Ce_{0.85}O_{1.925-\delta}$ has not been extensively studied here, but the data nevertheless suggest that a mechanism similar to that on Pt|YSZ is operative. Specifically, the data are consistent with a model in which oxygen surface diffusion to reaction sites is rate limiting. The hydrogen electro-oxidation reaction, in contrast, occurs by a mechanism quite distinct from that on YSZ. Here the electrode "conductivity" is found to obey a $-1/4$ power law dependence on oxygen partial pressure, $1/\rho^{\perp}_{\mathrm{Pt}} = 1/\rho^{\perp}_{\mathrm{Pt},0} p_{O_2}^{-1/4}$, with an activation energy for $1/\rho^{\perp}_{\mathrm{Pt},0}$ that is almost identical to that measured for the electronic conductivity. Accordingly, it is postulated that ceria is electrochemically active for hydrogen oxidation, with the reaction occurring directly on the ceria surface and limited by the rate of removal of electrons from the reaction sites.

Using $p_{O_2}(c)|Ba_{0.5}Sr_{0.5}Co_{0.8}Fe_{0.2}O_{3-\delta}|Sm_{0.15}Ce_{0.85}O_{2-\delta}(1350\,^{\circ}\mathrm{C})|\mathrm{Pt}|p_{O_2}(a)$ (system III) as the model system, it is demonstrated that the combination of OCV and impedance measurements yield valuable information at both the anode and cathode interfaces. It is suggested that the same electro-oxidation mechanism as that of system I and II is occurring at the Pt|ceria interface, whereas the resistance to the electro-reduction at the $Ba_{0.5}Sr_{0.5}Co_{0.8}Fe_{0.2}O_{3-\delta}$|ceria is negligible.

Appendix A

Dielectric and Chemical Capacitances

The chemical capacitance has certain similarities to conventional dielectric capacitance. While the latter is a measure of the ability of the system to store electrical energy in the form of polarized electric dipoles, the former is a measure of the ability of the system to store chemical energy in the form of changes in stoichiometry in response to changes of ambient partial pressures. The analogy is made more explicit as follows.

For a parallel plate capacitor with area A and length L, the conventional dielectric capacitance is

$$C_{dielec} = \frac{\partial q}{\partial \Delta\phi} = \frac{AD_{dis}}{EL} = \frac{A\varepsilon_r\varepsilon_0}{L} \tag{A.1}$$

where $D_{dis} = \varepsilon_r\varepsilon_0 E$ is the electrical displacement and E is the electrical field.

In the case of chemical capacitance, the stored charge due to species i is

$$q_i = z_i e c_i AL \tag{A.2}$$

The voltage drop across the capacitor is μ_i^*, defined previously from (2.5) and (2.10)

$$\mu_i^* = \frac{\mu_i^0}{z_i e} + \frac{k_B T}{z_i e} \ln \frac{c_i}{c_i^0} \tag{A.3}$$

Defining the capacitance in analogy to (A.1) as $\partial q_i / \partial \mu_i^*$ and evaluating this quantity yields

$$C_i^{chem} = \frac{\partial q_i}{\partial \mu_i^*} = \frac{(z_i e)^2}{k_B T} c_i AL \tag{A.4}$$

which, as implied by (2.128), is the total chemical capacitance associated with species i.

Appendix B

Estimates of Electrical and Chemical Capacitances

The system is $Sm_{0.15}Ce_{0.85}O_{2-\delta}$ (SDC15) with the following physical parameters.

- Vacuum permittivity $\varepsilon_0 = 8.8542 \times 10^{-12}$ F m^{-1}
- Boltzmann constant $k_B = 1.38 \times 10^{-23}$ J K^{-1}
- Relative permittivity (dielectric constant) $\varepsilon_r \approx 10$
- Sample area $A \approx 10^{-4}$ m^{-2}
- Sample length $L \approx 10^{-3}$ m
- The total grain boundary thickness $L_{GB} = 10^{-6}$ m
- Lattice constant $a_0 = 5.47$ Å
- Temperature $T = 600$ °C
- The number of electrical charge of oxygen vacancies $z_{ion} = 2$
- The number of electrical charge of electrons $z_{eon} = 1$
- Oxygen vacancy concentration c_{ion}

$$c_{ion} = \frac{n_{ion}}{a_0^3} = \frac{4 \times 0.075}{5.47^3 \times 10^{-30}} = 1.83 \times 10^{27} \text{ m}^{-3} \tag{B.1}$$

- Electron concentration c_{eon} can be taken as 1% of oxygen vacancy concentration for 0.5% H_2 saturated with 3% H_2O at 600 °C

$$c_{eon} = 1.83 \times 10^{25} \text{ m}^{-3} \tag{B.2}$$

B.1 Grain Interior Capacitance

The total grain interior thickness is approximated by the sample length

$$C_{GI} \approx \varepsilon_r \varepsilon_0 \frac{A}{L} \approx 10 \times 8.8542 \times 10^{-12} \times \frac{10^{-4}}{10^{-3}} \approx 10^{-11} \text{ F} \tag{B.3}$$

B.2 Grain Boundary Capacitance

The total grain boundary thickness is approximated to be 1 um

$$C_{GB} = \varepsilon \varepsilon_0 \frac{A}{L_{GB}} = 10 \times 8.8542 \times 10^{-12} \times \frac{10^{-4}}{10^{-6}} \approx 10^{-8} \text{ F} \tag{B.4}$$

At 600 °C, generally neither grain interior (GI) nor grain boundary (GB) arc is observable in the impedance spectra. The fitting for impedance spectrum circuit taken at 200 °C gives 10^{-11} and 10^{-8} F respectively for GI or GB using $R_{GI}C_{GI} - R_{GB}C_{GB}$ circuit. Since dielectric constant is not a strong function of temperatures, the experiment agrees with the estimate.

B.3 Interfacial Capacitance

Oxygen vacancy concentration in the interface can be roughly taken as the same as in the sample, thus the Debye screening length

$$L_D = \sqrt{\frac{\varepsilon \varepsilon_0 k_B T}{e^2 z_{ion}^2 c_{ion}}} = \sqrt{\frac{10 \times 8.8542 \times 10^{-12} \times 1.38 \times 10^{-23} \times 873}{(1.6 \times 10^{-19})^2 \times 2^2 \times 1.83 \times 10^{27}}} = 0.7 \text{ Å} \tag{B.5}$$

The interfacial capacitance is then

$$C_{ion}^{\perp} = \varepsilon\varepsilon_0 \frac{A}{L_D} = 10 \times 8.8542 \times 10^{-12} \times \frac{10^{-4}}{0.7 \times 10^{-10}} \approx 10^{-4} \text{ F} \tag{B.6}$$

The fitting of the impedance spectrum taken at 600 °C in air gives 10^{-4} F using $R_{ion}^{\perp} C_{ion}^{\perp}$ circuit which agrees with the estimate.

B.4 Chemical Capacitance

The chemical capacitance is determined by both the ionic and electronic concentration

$$\begin{aligned} C_{chem} &= \frac{e^2}{k_B T} AL \left(\frac{1}{z_{ion}^2 c_{ion}} + \frac{1}{z_{eon}^2 c_{eon}} \right)^{-1} \\ &= \frac{(1.6 \times 10^{-19})^2}{1.38 \times 10^{-23} \times 873} \times 10^{-4} \times 10^{-3} \times \left(\frac{1}{2^2 \times 1.83 \times 10^{27}} + \frac{1}{1.83 \times 10^{25}} \right)^{-1} \\ &\approx 4 \text{ F} \end{aligned} \tag{B.7}$$

The fitting of the impedance spectrum at 600 °C in 0.5% H_2 saturated with 3% H_2O gives 4 F using the Jamnik-Maier model.

Appendix C

Example Matrices

The equivalent circuits for the nonequilibrium and equilibrium conditions when $N = 2$ are shown in Figure C.1. The corresponding matrices ($\mathbf{A}^{neq}$ and $\mathbf{A}^{eq}$) and vectors ($\mathbf{X}$ and $\mathbf{B}$) are given in the next page.

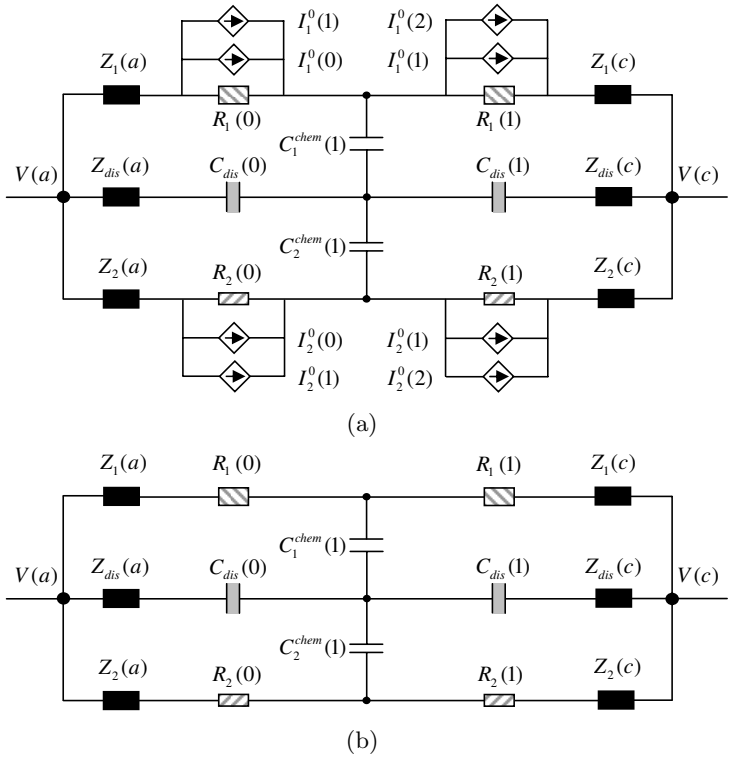

Figure C.1: (a) Nonequilibrium and (b) equilibrium equivalent circuit for $N = 2$.

$$\mathbf{A}^{neq} = \begin{pmatrix}
-1 & 0 & 0 & 0 & 0 & 0 & 0 & 0 & 0 & -Z_1(a) & 0 & 0 & 0 & 0 & 0 \\
Z_1(0)+Z_1^0 & Z_1(0)-Z_1^0 & 0 & 0 & 0 & 0 & -Z_1(0) & -Z_1(0) & 0 & -Z_1(0)Z_1^0 & 0 & 0 & 0 & 0 & 0 \\
0 & Z_1(1)+Z_1^0 & Z_1(1)-Z_1^0 & 0 & 0 & 0 & 0 & -Z_1(1) & -Z_1(1) & 0 & -Z_1(1)Z_1^0 & 0 & 0 & 0 & 0 \\
0 & 0 & 1 & 0 & 0 & 0 & 0 & 0 & 0 & 0 & -Z_1(c) & 0 & 0 & 0 & 0 \\
0 & 0 & 0 & -1 & 0 & 0 & 0 & 0 & 0 & 0 & 0 & -Z_2(a) & 0 & 0 & 0 \\
0 & 0 & 0 & Z_2(0)+Z_2^0 & Z_2(0)-Z_2^0 & 0 & 0 & 0 & 0 & 0 & 0 & -Z_2(0)Z_2^0 & 0 & 0 & 0 \\
0 & 0 & 0 & 0 & Z_2(1)+Z_2^0 & Z_2(1)-Z_2^0 & 0 & 0 & 0 & 0 & 0 & 0 & -Z_2(1)Z_2^0 & 0 & 0 \\
0 & 0 & 0 & 0 & 0 & 1 & 0 & 0 & 0 & 0 & 0 & 0 & -Z_2(c) & 0 & 0 \\
0 & 0 & 0 & 0 & 0 & 0 & -1 & 0 & 0 & 0 & 0 & 0 & 0 & -Z_{dis}(a) & 0 \\
0 & 0 & 0 & 0 & 0 & 0 & 1 & -1 & 0 & 0 & 0 & 0 & 0 & -Z_3(0) & 0 \\
0 & 0 & 0 & 0 & 0 & 0 & 0 & 1 & -1 & 0 & 0 & 0 & 0 & 0 & -Z_3(1) \\
0 & 0 & 0 & 0 & 0 & 0 & 0 & 0 & 1 & 0 & 0 & 0 & 0 & 0 & -Z_{dis}(c) \\
1 & 0 & 0 & 0 & 0 & 0 & 0 & -1 & 0 & -Z_1^{chem}(1) & Z_1^{chem}(1) & 0 & 0 & 0 & 0 \\
0 & 0 & 0 & 0 & 0 & 0 & 0 & 0 & 0 & 1 & -1 & 1 & -1 & 1 & -1 \\
0 & 0 & 0 & 0 & 1 & 0 & 0 & -1 & 0 & 0 & 0 & -Z_2^{chem}(1) & Z_2^{chem}(1) & 0 & 0
\end{pmatrix}$$

$$\mathbf{A}^{eq} = \begin{pmatrix}
-1 & 0 & 0 & 0 & 0 & 0 & 0 & 0 & 0 & -Z_1(a) & 0 & 0 & 0 & 0 & 0 \\
1 & -1 & 0 & 0 & 0 & 0 & 0 & 0 & 0 & -Z_1(0) & 0 & 0 & 0 & 0 & 0 \\
0 & 1 & -1 & 0 & 0 & 0 & 0 & 0 & 0 & 0 & -Z_1(1) & 0 & 0 & 0 & 0 \\
0 & 0 & 1 & 0 & 0 & 0 & 0 & 0 & 0 & 0 & -Z_1(c) & 0 & 0 & 0 & 0 \\
0 & 0 & 0 & -1 & 0 & 0 & 0 & 0 & 0 & 0 & 0 & -Z_2(a) & 0 & 0 & 0 \\
0 & 0 & 0 & 1 & -1 & 0 & 0 & 0 & 0 & 0 & 0 & -Z_2(0) & 0 & 0 & 0 \\
0 & 0 & 0 & 0 & 1 & -1 & 0 & 0 & 0 & 0 & 0 & 0 & -Z_2(1) & 0 & 0 \\
0 & 0 & 0 & 0 & 0 & 1 & 0 & 0 & 0 & 0 & 0 & 0 & -Z_2(c) & 0 & 0 \\
0 & 0 & 0 & 0 & 0 & 0 & -1 & 0 & 0 & 0 & 0 & 0 & 0 & -Z_{dis}(a) & 0 \\
0 & 0 & 0 & 0 & 0 & 0 & 1 & -1 & 0 & 0 & 0 & 0 & 0 & -Z_3(0) & 0 \\
0 & 0 & 0 & 0 & 0 & 0 & 0 & 1 & -1 & 0 & 0 & 0 & 0 & 0 & -Z_3(1) \\
0 & 0 & 0 & 0 & 0 & 0 & 0 & 0 & 1 & 0 & 0 & 0 & 0 & 0 & -Z_{dis}(c) \\
1 & 0 & 0 & 0 & 0 & 0 & 0 & -1 & 0 & -Z_1^{chem}(1) & Z_1^{chem}(1) & 0 & 0 & 0 & 0 \\
0 & 0 & 0 & 0 & 0 & 0 & 0 & 0 & 0 & 1 & -1 & 1 & -1 & 1 & -1 \\
0 & 0 & 0 & 0 & 1 & 0 & 0 & -1 & 0 & 0 & 0 & -Z_2^{chem}(1) & Z_2^{chem}(1) & 0 & 0
\end{pmatrix}$$

$$\mathbf{X} = \begin{pmatrix} V_1(0) & V_1(1) & V_1(2) & V_2(0) & V_2(1) & V_2(2) & V_{dis}(0) & V_{dis}(1) & V_{dis}(2) & I_1(0) & I_1(1) & I_2(0) & I_2(1) & I_{dis}(0) & I_{dis}(1) \end{pmatrix}^{-1}$$

$$\mathbf{B} = \begin{pmatrix} -V(a) & 0 & 0 & V(c) & -V(a) & 0 & 0 & V(c) & -V(a) & 0 & 0 & V(c) & 0 & 0 & 0 \end{pmatrix}^{-1}$$

Appendix D

Analytical Impedance Calculation

The impedance of the general electrode|MIEC|electrode system represented in Figure 2.13(a) of the main text can be evaluated by first recasting the circuit from one composed of R and C to one composed of elements with arbitrary impedance in Figure D.1. Here, V_a and V_b are the input and output voltages respectively. I is the total current. $V_1(x)$ and $I_1(x)$ are the voltage and current for the branch point in rail 1. $V_2(x)$ and $I_2(x)$ are the voltage and current for the branch point in rail 2. Z_A and Z_B are the terminal impedances corresponding to the impedance of the electrode|MIEC in rails 1 and 2 respectively. Z_1 and Z_2 are the impedances in rails 1 and 2 respectively whereas Z_3 is the impedance between rail 1 and 2.

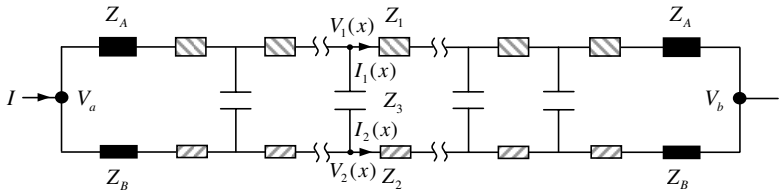

Figure D.1: Generalized circuit.

Z_1, Z_2 and Z_3 are defined respectively as

$$Z_1 = Z_1^T \frac{\Delta x}{L} \tag{D.1}$$

$$Z_2 = Z_2^T \frac{\Delta x}{L} \tag{D.2}$$

$$Z_3 = Z_3^T \frac{L}{\Delta x} \tag{D.3}$$

where Z_1^T, Z_2^T and Z_3^T are the total impedance of three components. When $N{=}L/\Delta x$

reaches infinity, $\Delta x \to 0$ and the discretized circuit in Figure D.1 becomes a continuous one. Ohm's law implies

$$\frac{dV_1(x)}{dx} = -\frac{Z_1^T}{L} I_1(x) \tag{D.4}$$

$$\frac{dV_2(x)}{dx} = -\frac{Z_2^T}{L} I_2(x) \tag{D.5}$$

Kirchhoff's law implies

$$-\frac{dI_1(x)}{dx} = \frac{dI_2(x)}{dx} = \frac{V_1(x) - V_2(x)}{Z_3^T L} \tag{D.6}$$

$$I = I_1(x) + I_2(x) \tag{D.7}$$

The boundary conditions are

$$V_a - V_1(0) = Z_A I_1(0) \tag{D.8}$$

$$V_a - V_2(0) = Z_B I_2(0) \tag{D.9}$$

$$V_1(L) - V_b = Z_A I_1(L) \tag{D.10}$$

$$V_2(L) - V_b = Z_B I_2(L) \tag{D.11}$$

$$V_a - V_b = ZI \tag{D.12}$$

where Z is the total impedance. From (D.4)–(D.7), one obtains

$$Z_3^T L^2 I_1'' - \left(Z_1^T + Z_2^T\right) I_1 + Z_2^T I = 0 \tag{D.13}$$

The solution to (D.13) is

$$I_1(x) = \frac{Z_2^T}{Z_1^T + Z_2^T} I + C_1 e^{kx} + C_2 e^{-kx} \tag{D.14}$$

with

$$k = \frac{1}{L}\sqrt{\frac{Z_1^T + Z_2^T}{Z_3^T}} \tag{D.15}$$

and C_1 and C_2 are two unknowns. The solutions to other parameters are

$$I_2(x) = \frac{Z_1^T}{Z_1^T + Z_2^T} I - C_1 e^{kx} - C_2 e^{-kx} \tag{D.16}$$

$$V_1(x) = -\frac{Z_1^T Z_2^T}{Z_1^T + Z_2^T} \frac{x}{L} I - \frac{C_1 Z_1^T}{kL} e^{kx} + \frac{C_2 Z_1^T}{kL} e^{-kx} \tag{D.17}$$

$$V_2(x) = -\frac{Z_1^T Z_2^T}{Z_1^T + Z_2^T} \frac{x}{L} I + \frac{C_1 Z_2^T}{kL} e^{kx} - \frac{C_2 Z_2^T}{kL} e^{-kx} \tag{D.18}$$

Applying boundary conditions (D.8)–(D.12), one obtains

$$Z = \frac{Z_1^T Z_2^T}{Z_1^T + Z_2^T} + \frac{2}{Z_1^T + Z_2^T} \frac{kLZ_AZ_B(Z_1^T + Z_2^T) + \left[(Z_2^T)^2 Z_A + (Z_1^T)^2 Z_B\right] \tanh(\frac{kL}{2})}{kL(Z_A + Z_B) + (Z_1^T + Z_2^T) \tanh(\frac{kL}{2})} \tag{D.19}$$

For the circuit in Figure 2.13(a), the corresponding circuit elements are

$$Z_A = Z_{ion}^{\perp} \tag{D.20}$$

$$Z_B = 0 \tag{D.21}$$

$$Z_1 = R_{ion}/N \tag{D.22}$$

$$Z_2 = R_{eon}/N \tag{D.23}$$

$$Z_3 = (j\omega C_{chem}/N)^{-1} \tag{D.24}$$

Thus one obtains

$$Z_1^T = R_{ion} \tag{D.25}$$

$$Z_2^T = R_{eon} \tag{D.26}$$

$$Z_3^T = 1/(j\omega C_{chem}) \tag{D.27}$$

The argument of the hyperbolic tangent in (D.15) can be evaluated

$$k = \sqrt{\frac{(R_{ion} + R_{eon}) j\omega C_{chem}}{L^2}} = \sqrt{\frac{j\omega}{\tilde{D}}} \tag{D.28}$$

with

$$\tilde{D} = \frac{L^2}{(R_{ion} + R_{eon}) C_{chem}} \tag{D.29}$$

Plugging (D.20), (D.21) and (D.25)–(D.29) into (D.19) then yields

$$Z(\omega) = R_\infty + (Z_0 - R_\infty) \frac{\tanh\sqrt{\frac{j\omega L^2}{4\tilde{D}}} + \frac{R_{ion}+R_{eon}}{2Z^\perp_{ion}} \tanh\sqrt{\frac{j\omega L^2}{4\tilde{D}}}}{\sqrt{\frac{j\omega L^2}{4\tilde{D}}} + \frac{R_{ion}+R_{eon}}{2Z^\perp_{ion}} \tanh\sqrt{\frac{j\omega L^2}{4\tilde{D}}}} \tag{D.30}$$

with

$$\frac{1}{Z_0} = \frac{1}{R_{ion} + 2Z^\perp_{ion}} + \frac{1}{R_{eon}} \tag{D.31}$$

and

$$R_\infty = \frac{R_{ion}R_{eon}}{R_{ion} + R_{eon}} \tag{D.32}$$

(D.30) differs from Equation (7) given in reference[34] by the term $(Z_0 - Z_\infty)$ which has apparently been omitted from that paper due to a typographical misprint.

Appendix E

High-Surface-Area Ceria Aerogel

Abstract

Ceria (CeO_2) aerogels with high surface area and high porosity have been prepared. Ce-methoxyethoxide diluted in excess methoxyethanol was slowly hydrolyzed to yield a gel, which was then supercritically dried in CO_2. Both as-synthesized and annealed aerogels were examined by X-ray powder diffraction, infrared spectroscopy, scanning electron microscopy and BET surface area and pore size analyses. Thermal analysis of the as-synthesized gel showed it to contain only ∼5 wt% residual organics which were removed by 300 °C under oxygen. The unheated ceria aerogel was crystalline and exhibited a specific surface area of 349 m^2/g with average pore diameter of ∼21.2 nm and 90% porosity. Heat treatment led to a reduction of porosity and pore size, as would be expected, but the extremely narrow pore size distribution of the aerogel was retained.

E.1 Introduction

The mesoporous nanoarchitecture of aerogels leads to high-performance materials for catalysis and electrocatalysis. While the importance of high surface area has been well appreciated by researchers, the ability to manage the pore-solid architecture to support electrochemical reactions and achieve facile mass transport of products and reactants has not been widely considered.[83,84] Early indications are that the use of aerogels in a nanoscopic building-block approach is extremely promising; for example, considerable improvement in the performance of electrodes for electro-oxidation of methanol in proton-exchange membrane fuel cells (PEMFCs) has already been demonstrated.[85] Aerogels are highly porous (open porosity with large pore volume) three dimensional networks with an extremely large inner surface that is easily accessible to reactants.[86–88] Aerogel preparation procedure combines the flexibility and advantages of the sol-gel process in terms of control of the composition, homogeneity and retention of the textural properties of the wet gel.

The present paper extends aerogel synthesis to cerium oxide, a material of significant industrial importance. Ceria-based materials find application in a wide range of processes; for example, they serve as additives or promoters for fluid catalytic cracking, ammoxidation and dehydrogenation processes[89–92] and as supports for automotive three-way catalysts. Because of the low redox potential of the Ce^{4+}–Ce^{3+} couple, ceria can release oxygen during fuel-rich conditions and uptake oxygen in fuel-lean conditions, key for optimal performance of automotive catalytic converters. Ceria has also been used as an oxygen ion conducting electrolyte for solid oxide fuel cells.[93,94] More recently, it has been shown that ceria has the ability to resist carbon deposition, and can be utilized in solid oxide fuel cell (SOFC) anodes, either for indirect or direct electrochemical oxidation of hydrocarbon fuels such as methanol or methane.[95,96]

The synthesis of pure ceria aerogels has received little attention, although the potential of aerogels to have tremendous positive impact on catalysis has been increasingly recognized.[86–88] We are aware of only one publication on the topic,[97] if one uses the standard definition of an aerogel as a material prepared by sol-gel synthesis followed by supercritical drying to remove the solvent.[86–88] In that work supercritical methanol (240 °C, 80 bar)

was employed to dry a ceria alcogel derived from Ce-acetylacetonate. The surface area of the amorphous product ranged from 65 to 104 m^2/g and no other characterization of the aerogel was presented. Routes that lead to materials with higher surface area and higher crystallinity, both of which are important for developing the desired catalytic and electrochemical properties, are clearly desirable.

Given the importance of ceria in catalysis, high surface area CeO_2 has indeed been pursued by a variety of chemical synthesis routes.[98–105] Resultant surface areas have typically been $\sim$100 m^2/g, and in limited cases as high as $\sim$200 m^2/g. Moreover, such materials tend to exhibit a broad pore size distribution. Most recently, surfactant templated synthesis has been attempted.[106–109] This route is promising in that it yields materials with high surface area (as high as $\sim$245 m^2/g).[108] However, the pore size and size distribution are not optimally suited for catalysis. In particular, the pores in surfactant templated materials tend to be small and are often assembled in a one-dimensional arrangement rather than an interconnected, three-dimensional structure. Moreover, there are reports that mesopores in these materials can be blocked upon deposition of metallic catalyst particles.[106] These features can impede diffusion of the reactant and by-product gases and prevent effective catalysis.

In this work we report the synthesis and characterization of high-surface-area ceria aerogels prepared by cold (CO_2) supercritical drying. The synthesis process is complete in a matter of hours and it is possible, by appropriate heat treatment, to control the crystallite size of the fluorite phase that comprises the solid network as well as the pore structure of the aerogel. This synthetic approach enables one to consider ceria aerogel as a building block with tailored morphology for catalytic and electrochemical applications. In contrast to other approaches, aerogel materials can furthermore be obtained as monoliths and thus, in principle, porosity and surface area are not compromised in post synthesis processing of loose powders. The key to the success of the method reported here is the identification of a chemical system incorporating cerium precursor, solvent, and chelating agent which allows for controlled hydrolysis and condensation of the ceria phase, without rapid precipitation.

E.2 Experimental

Ceria aerogel synthesis involved, as is conventional, two steps: gel synthesis and supercritical drying. Gel synthesis was achieved by dilution of the precursor, Ce-methoxy ethoxide in methoxyethanol (18–20 w/w%, Alfa Aesar, USA), with solvent (2-methoxy ethanol, Alfa Aesar, USA). The solution was then modified with acetyl acetone (Avocado, USA) and hydrolyzed with water, to yield a transparent, light brown gel, similar in color to the cerium precursor compound. The time for gelation could be varied from instant to several days by changing the ratio of precursor : solvent : acetyl acetone : water. Aerogels with the highest surface area were obtained for the molar ratio 1 : 8 : 0.5 : 8, in which case gel formation occurred within an hour, yielding a monolithic, self-supporting material. After gelation, the sample, typically ∼2 gm, was aged for 3 days in a closed container. In order to improve the miscibility of the liquid within the pores of the gel with the super critical drying medium (liquid CO_2), an intermediate solvent exchange with acetone was performed. The monolithic gel was fractured into small pieces to facilitate fast solvent exchange and then immersed in acetone for three days, over the course of which the solvent was exchanged with fresh acetone three times. During solvent exchange the morphology of the gel remained intact. The modified gel was then placed in a critical point dryer (Quorum Technologies E3000, specimen chamber: horizontal, 30.1 mm internal diameter and 82 mm long). The acetone in the gel was exchanged with liquid CO_2 at 10 °C by rinsing 10 or more times over a period of more than four hours. The carbon dioxide solvent was eliminated by heating past the critical point of liquid CO_2 (45 °C, ∼82 bar) and slowly releasing the resulting CO_2 gas (<20 mL/sec). The quantity of liquid CO_2 utilized for the supercritical drying process was approximately 300 mL/gm of gel precursor, which corresponds to ∼750 mL CO_2 per gm of CeO_2 samples prepared using excess water for hydrolysis in the initial synthesis steps.

The as-synthesized aerogel was obtained in the form of monolithic pieces, up to 8 mm × 6 mm × 2 mm in size, along with fine powder. The sample retained its light brown color, suggesting that some of the coordinating/chelating organic groups which are responsible for the color of the precursor (in which all Ce is in the 4+ oxidation state) were still present in the aerogel. Portions of the as-prepared aerogel were annealed in air at 300 °C and at 600

°C, in both cases for 2 hours. Annealing induced a color change to pale yellow, indicating complete removal of the organic groups. Cerium likely exists in the 4+ oxidation state at all stages of sample preparation, irrespective of the sample color.

Several techniques were used to characterize the properties of the resultant material. Thermo gravimetric (TG) and differential scanning calorimetry (DSC) analyses were carried out in flowing oxygen (Netzsch thermo analyser STA 449C) from 25 to 1,000 °C at a heating rate of 10 °C/min. Infrared (FTIR) spectra were recorded using a Nicolet Magna 860 IR spectrometer over the wave number range 4000 to 400 cm^{-1}. Powder X-ray diffraction (XRD) data were collected at room temperature on the aerogel samples using a Philips (PW 3040) diffractometer with Cu K_α radiation in the Bragg-Brentano geometry. Grain/particle size measurements were made by applying the Scherrer equation to the FWHM of the (111) peak, after accounting for instrument broadening using silicon as a standard. The aerogel microstructure and morphology were studied by a LEO 1550VP Field Emission SEM.

Specific surface area and pore size distribution were determined using a Micromeritics surface area analyzer (ASAP 2010). Nitrogen adsorption/desorption isotherms were obtained at 77 K after outgassing the samples at 120 °C for 2 hours. Surface area was calculated using the BET method.[110] Pore size distribution was determined by applying the BJH method[111] to the desorption branch of the isotherm. It has been shown that nitrogen adsorption and desorption (NAD) analysis of compliant porous materials such as aerogels is significantly influenced by the equilibration time, and possible compliance of the sample.[112,113] In particular, both insufficient equilibration and contraction of the sample due to capillary forces will yield measured pore volumes that are less than the actual values. Evidence for insufficient equilibration is apparent in the isotherm data in the form of adsorption and desorption branches that are strongly shifted from one another, and for compliant gels in the form of a continued increase in nitrogen adsorption beyond the apparent saturation point. For the present NAD analysis of ceria aerogels, equilibration was considered to be reached when the first derivative of the pressure was less than 0.01% of the average pressure over a specified time interval which was 10 seconds for the present study. The maximum volume adsorbed between points was set to be 50 cm^3/g.

E.3 Results and Discussion

Thermal analysis of the as-synthesized aerogel (Figure E.1) revealed weight-loss steps. The first step, over the temperature range 150–200 °C is assigned to desorption of water adsorbed on the aerogel surface. The second step, with peak weight loss occurring at ∼280 °C and accounting for ∼5 wt%, is taken to be due to the burn-off of the residual organic chelating agent, acetyl acetone. Exothermic peaks accompany both weight loss steps.

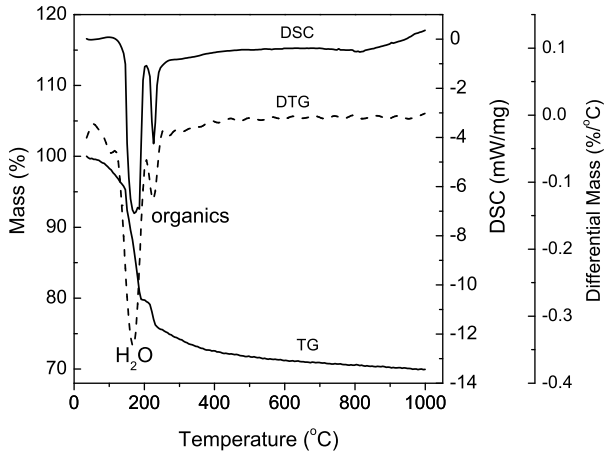

Figure E.1: Thermalgravimetric and differential scanning calorimetry curves of as-synthesized CeO_2 aerogel obtained under flowing O_2 at a heating rate of 10 °C/min.

The presence of residual organics and hydroxyl ions/water, in the as-synthesized gel is confirmed by the FTIR spectrum. Figure E.2, curve (a), shows a strong C=O stretching peak at ∼1600 cm^{-1}, several C-H bands, and a weak O-H stretching band at ∼3400 cm^{-1}. After heat-treatment at 300 °C, curve (b), the intensities of the peaks due to the organics are substantially reduced, while treatment at 600 °C eliminates all peaks except that due to Ce-O stretching at ∼500 cm^{-1}, curve (c). These observations are in general agreement with the thermal analysis. The high intensity at 300 °C of the IR peak corresponding to O-H stretching is attributed to the rapid adsorption of atmospheric H_2O onto the ceria aerogel surface after removal of the chelating organic groups.

As-synthesized, the CeO_2 aerogel shows very broad and weak diffraction peaks that can be attributed to the cubic fluorite phase of ceria, Figure E.3. Upon annealing, these peaks sharpen considerably, as would be expected for the growth in the crystallite size with heat

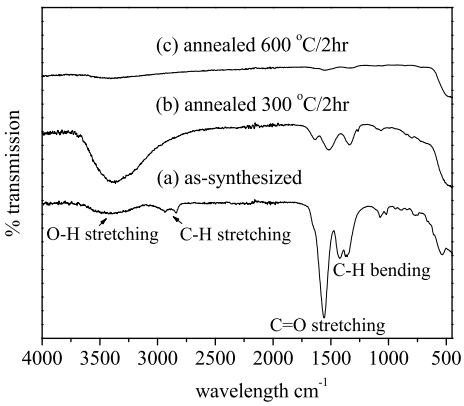

Figure E.2: FTIR spectra collected from ceria aerogel, heat treated as indicated.

treatment.

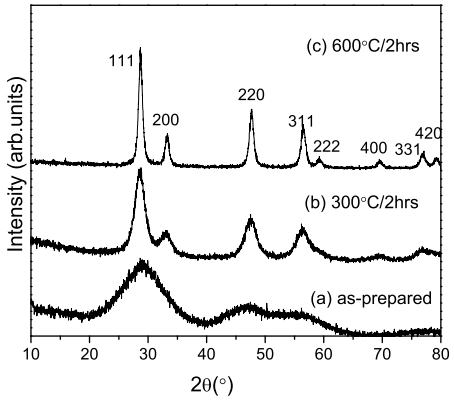

Figure E.3: X-ray diffraction patterns of CeO_2 aerogel, heat-treated as indicated.

The morphology of the as-synthesized aerogel is highly porous and extremely uniform, as evidenced both by electron microscopy (Figure E.4), and nitrogen adsorption studies (Figures E.5 and E.6) and Table E.1. The aerogel exhibits an adsorption isotherm of type IV (IUPAC classification) with a marked hysteresis loop of H1 type (Figure E.5a). Type IV isotherms are characteristic of mesoporous materials.[110] The hysteresis loop of type H1 is usually associated with agglomerates or compacts of uniform spheres, which have a narrow pore size distribution and open tubular pores with circular or polygonal sections. While hysteresis between the adsorption and desorption branches is evident, its magnitude is sufficiently small as to confirm that nitrogen adsorption equilibration has been reached. Furthermore, the adsorption reaches a clear saturation value, particularly for the annealed samples, indicating corrections for compliancy need not be applied. In any case,

should equilibration and compliancy influence the results, the pore volumes reported here correspond to a lower bound.

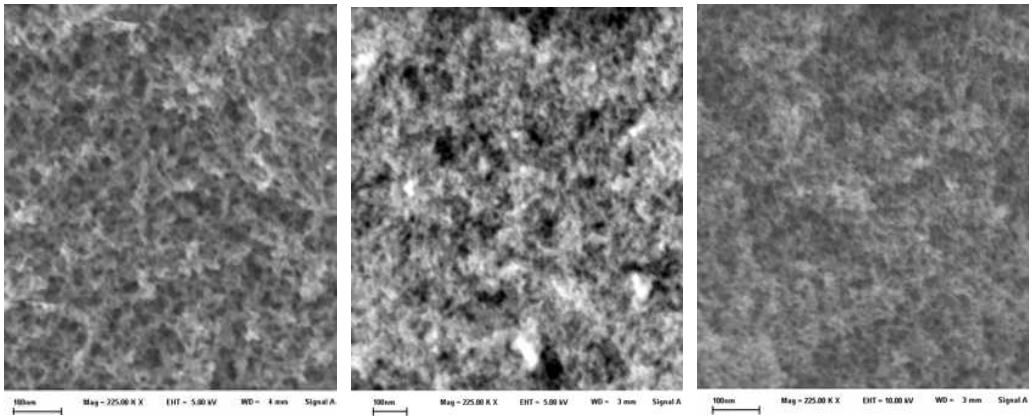

(a) (b) (c)

Figure E.4: Pore size distribution in (a) as-prepared, (b) 300 °C/2hr annealed and (c) 600 °C/2hr annealed CeO_2 aerogel.

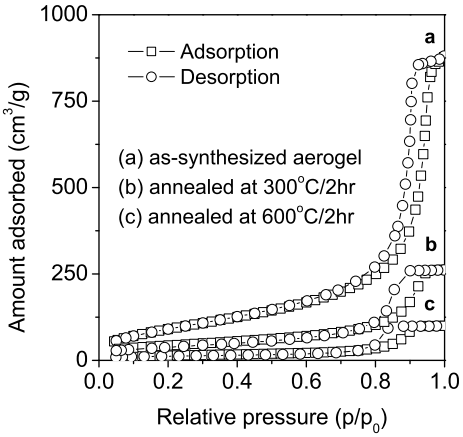

Figure E.5: Nitrogen adsorption isotherms at 77 K of (a) as-prepared, (b) 300 °C/2hr annealed and (c) 600 °C/2hr annealed CeO_2 aerogel.

The narrowness of the pore diameter distribution, which has a maximum at 21.2 nm, is further evident in Figure E.6a. The as-prepared aerogel has a large surface area of 349 m^2/g and, the large pore size (>10 nm) is well suited for facile mass transport. Moreover, the pores are randomly connected in a three-dimensional network (Figure E.5), which is further anticipated to promote gas diffusion through the aerogel structure.

Heat treatment reduces the porosity and increases the average grain size (Table E.1).

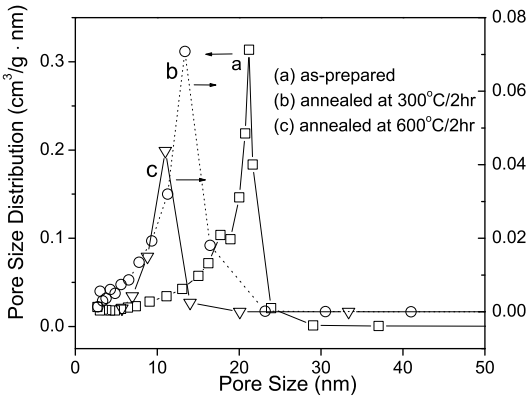

Figure E.6: Pore size distribution in (a) as-prepared, (b) 300 °C/2hr annealed and (c) 600 °C/2hr annealed CeO_2 aerogel.

Table E.1: Microstructural properties of ceria aerogel

CeO_2 Aerogel	X-ray grain size nm	BET surf. area m^2/g	Ave. pore diameter nm	Most freq. pore diameter nm	Pore vol. cm^3/g	Porosity %
As-prepared	<2	349	14.3	21.2	1.33	90
300°C/2hr	4.8	155	11.5	13.4	0.40	80
600°C/2hr	15.9	49	10.4	11.0	0.15	51

However, the overall morphology of the aerogel remains unchanged, consisting of nanocale grains with interconnected, mesoscale porosity (Figure E.5). Furthermore, the type of isotherm and hysteresis are also unchanged by the heat treatment; the pore size remains large and the distribution remains extremely narrow. The overall reduction in porosity is evident from the sharp decrease in the amount of nitrogen adsorbed (Figure E.5). Quantitatively, the specific surface area decreases from 349 to 49 m^2/g, the porosity from 90% to 51% and the average pore diameter from 14.3 to 10.4 nm upon annealing at 600 °C, while the maximum in the pore size distribution shifts from 21.2 to 11.0 nm. The average grain or particle size, which is related to the aerogel wall thickness, increases from a value that cannot be reliably determined by X-ray diffraction, smaller than 2 nm to almost 16 nm upon heat treatment.

Implementation of aerogels in high temperature catalysis requires that high surface area and porosity be maintained for long time periods. Thermally stable structures can be pursued by introduction of zirconia via incorporation of zirconium precursor compounds in

the gel solution, which has been shown to mitigate loss of porosity.[114]

E.4 Conclusions

We have successfully synthesized ceria aerogels. The material exhibits high surface area, large pore volume, mesoporosity and a narrow pore size distribution. To date only one other synthetic route to ceria aerogels has appeared in the literature.[97] In that work a maximum surface area of 104 m^2/g was obtained, which is much lower than the value of 349 m^2/g achieved here for as-synthesized gels. Also, using our synthetic route, the fluorite phase is already apparent before any thermal treatment. Even for aerogels in which residual organics have been removed via heat treatment at 300 °C, the surface area remains at the high value of 155 m^2/g. In terms of fuel cell anodes, no particular surface area, porosity or pore size targets have been established. Nevertheless, the materials fabricated in this study appear well suited to electrode function. In particular, the narrow distribution of large pore diameters and tuneable porosity lend themselves to optimized electrocatalysis. Furthermore, the route is readily adapted for the preparation of bulk ceria aerogels (although no particular efforts were made in the present study to retain monolithic structures) and also for zirconia incorporation through cogelation of Ce-alkoxide and Zr-alkoxide, which can result in thermally stable structures for high temperature applications.

E.5 Acknowledgements

The authors thank Professor George Rossman and Dr. Ma Chi for assistance with FTIR spectroscopy and electron microscopy, respectively.

Appendix F

Proton Conduction in Mg-Doped $La_2Zr_2O_7$ Pyrochlore Oxide

Abstract

Undoped and Mg-doped $La_2Zr_2O_7$ with a pyrochlore structure were prepared by a combined EDTA-citrate complexing method. $La_2Zr_{2-x}Mg_xO_7$ was single phase up to $x = 0.2$ and lattice parameters increase with Mg doping. Proton conduction in Mg-doped $La_2Zr_2O_7$ pyrochlore oxide was studied by A.C. impedance spectroscopy. Both grain interior and specific grain boundary conductivities were extracted from impedance data by using the brick layer model. An isotope effect under H_2O- or D_2O- containing atmospheres was observed, indicating that protons (or deuterons) are the mobile species. The isotope effect was discussed on the basis of a statistical mechanical transition state theory.

F.1 Introduction

Since the discovery of high-temperature proton conduction in a $SrCeO_3$-based system,[115] many attempts have been made to find new oxides which show high proton conductivity at high temperatures because of their potential applications such as fuel cells and hydrogen sensors. Proton incorporation into such materials has been generally recognized to occur by a two-step process.[116–118] The first step is the creation of oxygen vacancies. The second step, the exposure of the material to H_2O or H_2 containing atmospheres, leads to the occupation of previously vacant oxygen sites by hydroxyl groups.

Up to now, most efforts have been devoted to perovskite-based oxides like simple perovskites ABO_3 (A=II; B=IV—Roman numericals represent the valences) and complex perovskites $A_2(B'B'')O_6$ (A=II; B′=III; B″=V)and $A_3(B'B''_2)O_9$ (A=II; B′=II; B″=V).[116–118] The acceptor-doping in simple perovskites such as Yb-doped SrCeO3 or nonstoichiometry of B site cations in complex perovskites such as $Ba_3(Ca_{1.18}Nb_{1.82})O_{9-\delta}$ will introduce oxygen vacancies. Subsequent exposure to hydrogen containing atmospheres leads to proton incorporation. On the other hand, the proton conduction in fluorite-based oxides has been less studied compared to the extensive investigation of fluorite-based oxides as oxygen ion conductors. Pyrochlore oxide $A_2B_2O_7$ (A=III; B=IV) has a fluorite-based structure.[119] For a fluorite structure, there are four cations and eight oxygen ions in the unit cell. The cations A and B in pyrochlore structure have a significant size difference and they are completely ordered at the cation sites of the fluorite structure. Furthermore, the anion sites of the fluorite structure are ordered into three different sites; six equivalent oxygen sites, one differing oxygen site, and one structurally empty site. The structural oxygen vacancy and possible acceptor doping at A or B site make pyrochlore oxide also candidates for proton conduction.

Recently, it was reported by Shimura *et al.*[120] and Omata *et al.*[121] that doped $La_2Zr_2O_7$ with a pyrochlore-type structure is a promising material for high-temperature proton conductor. Shimura *et al.*[120] found $La_2Zr_{1.8}Y_{0.2}O_{7-\delta}$ has the highest conductivity among the $Ln_2Zr_{1.8}Y_{0.2}O_{7-\delta}$ (Ln=La, Nd, Gd, Sm), around 3×10^{-4} S/cm at 600 °C in wet hydrogen. Omata *et al.*[121] found the solubility limit of $La_2Zr_{2-x}Ca_xO_{7-\delta}$ is around 0.015 and

$La_2Zr_{1.985}Ca_{0.015}O_{7-\delta}$ has a conductivity of 1.0×10^{-4} S/cm at 600 °C in wet hydrogen.

In the pyrochlore structure, Zr site is approximately surrounded by six oxygen ions. According to Shannon's ionic radius,[122] Mg^{2+} (VI, 0.72 Å—Roman numericals represent the coordination number) is a better dopant than both Y^{3+} (VI, 0.89 Å) and Ca^{2+} (VI, 1.00 Å) to Zr^{4+} (VI, 0.72 Å). Furthermore, according to Pauling's electronegativity scale,[123] Zr has an electronegativity of 1.33. Compared with Y(1.22) and Ca(1.00), Mg has a similar scale of 1.31 to Zr. Based on the ionic radius and electronegativity, we expect the solubility of Mg at Zr site will be higher than Y and Ca. The increased doping will be able to provide more oxygen vacancies for proton incorporation. In the present study, proton conduction of grain interiors and grain boundaries of undoped and Mg-doped $La_2Zr_2O_7$ was investigated. The conductivity isotope effect under H_2O or D_2O containing atmospheres was discussed on the basis of a statistical mechanical transition state theory.

F.2 Experimental

F.2.1 Sample Preparation

Starting materials La_2O_3 99.9%, MgO 99.95%, $ZrO(NO_3)_2{\cdot}xH_2O$ (x was determined by thermogravimetric analysis), nitric acid (ACS, 70%), $NH_3{\cdot}H_2O$ (ACS, 28.0–30.0%) and ethylene eiamine tetraacetic acid (EDTA, ACS, 99.4+ %) were purchased from Alfa Aesar. Hydrogen peroxide 30 % aqueous solution and citric acid monohydrate were obtained from Fisher Chemical and Mallinckrodt respectively. $La_2Zr_{2-x}Mg_xO_7$ was synthesized by a combined EDTA-citrate complexing route.[124] Briefly, La_2O_3 and MgO were first dissolved in nitric acid and $ZrO(NO_3)_2$ was dissolved in H_2O_2 water solution at 150 °C. Two solutions were mixed together and EDTA-ammonia solution and citric acid solution were added sequentially in a ratio of La : EDTA : citric acid of 1 : 4 : 8. The obtained whole solution was continuously stirred at 80 °C until gelation occurred. The obtained gel was first dried at 200 °C, then pre-fired at 400 °C and finally calcined at different temperatures from 700 to 1100 °C. The powders calcined at 900 °C were first uniaxially pre-pressed at 65 MPa, then cold isostatically pressed at 220 MPa for 5 mins. The green pellets were finally sintered at 1550 °C for 12 hrs. Densities were determined by simple measurements of pellet dimensions

and weight after polishing the surfaces.

F.2.2 X-ray Diffraction

The X-ray diffraction (XRD) analyses were carried out at room temperature in a Siemens D-500 diffractometer with Cu Kα radiation. Intensities were obtained in the 2θ range between 20° and 90° with a step of 0.02° and a measuring time of 3 s at each point. Because the diffraction peaks of Si standard overlap with those of samples, nickel powders with particle sizes around 50 um were used as the internal standard. Full With at Half Maximums (FWHMs) of the peaks were obtained using Origin program (OriginLab Corp.). The instrument broadening was approximated by the FWHM of (111) peak of Si powders around 100 um. The particle sizes of the sample powders were calculated by Scherrer method using FWHMs of (222) peak. The crystalline structures were refined by using Rietica program with Rietveld method.

F.2.3 Nitrogen Adsorption

The specific surface area was measured by nitrogen adsorption at 77 K using the BET (Brunauer-Emmett-Teller) equation. The experiments were performed on Micromeritics Gemini 2360 surface area analyzer. Prior to measurement, the samples were outgassed at 120 °C overnight with flowing nitrogen using FlowPrep 060 degasser.

F.2.4 Impedance Spectroscopy

The Pt ink (Engelhard 6082) was applied to both sides of the 95% dense pellets and fired at 900 °C for 2 hours. Two probe impedance spectroscopy was performed by Solartron 1260 impedance analyzer with an amplitude 30 mV and frequency range from 0.1 to 10 M Hz. The atmospheres were 3% H_2O- saturated or D_2O-saturated argon. Impedance data were fit to an equivalent circuit model $(R_1Q_1)(R_2Q_2)$ using the least-squares refinement program of *ZView* (Scribner Associates Inc.). R is resistance and Q is constant phase element.

F.3 Results and Discussion

F.3.1 $La_2Zr_2O_7$

F.3.1.1 XRD Characterization

XRD patterns of pure $La_2Zr_2O_7$ (Figure F.1) show that there is indication of pyrochlore phase formation at 700 °C. Pure cubic pyrochlore phase is formed at 800 °C. The peaks become sharper with increasing calcination temperature which means both the crystallinity and particle sizes increase from 800 to 1100 °C. Particle sizes of powders can be estimated from XRD patterns by applying the Scherrer equation. First, the X-ray diffraction peaks were found to be better fitted to Lorentzian rather than Gaussian profiles. Second, for Lorentzian peaks, peak broadening Γ_{sample} caused by the particle size effect can be obtained by

$$\Gamma_{sample} = \Gamma_{total} - \Gamma_{instrument} \tag{F.1}$$

where Γ_{total} and $\Gamma_{instrument}$ are the measured total broadening and instrument broadening respectively. The Scherrer equation is given as

$$D_{Scherrer} = \frac{0.9\lambda}{\Gamma_{sample}\cos\theta} \tag{F.2}$$

where λ is X-ray wavelength and θ is diffraction angle for peak (222). The calculated XRD particle sizes $D_{Scherrer}$ of powders calcined at different temperatures are listed in Table F.1. The table shows a growth of particles from 0.05 um to 0.17 um when the calcination temperature increases from 800 to 1100 °C.

Table F.1: Specific surface areas and particle sizes calculated by the XRD and BET methods of $La_2Zr_2O_7$ powders calcined at different temperatures

Temperature (°C)	$D_{Scherrer}$ by XRD (um)	Specific Surface Area (SSA) (m^2/g)	D_{BET} by BET (um)
800	0.05	18.1	0.06
900	0.06	13.0	0.08
1000	0.10	8.9	0.11
1100	0.17	6.3	0.16

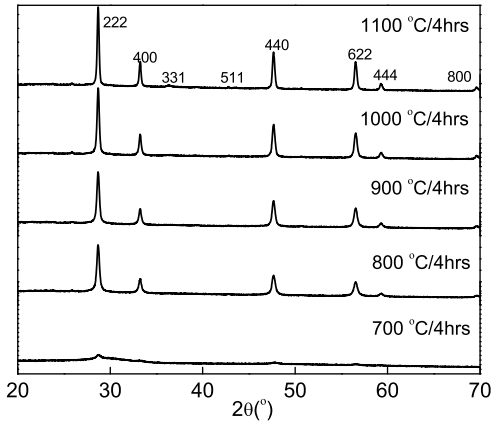

Figure F.1: X-ray powder diffraction patterns of $La_2Zr_2O_7$ calcined at given temperatures for 4 hrs.

F.3.1.2 BET Characterization

In Table F.1, the surface areas of pure $La_2Zr_2O_7$ powders decrease with increasing calcination temperatures as expected. Assuming the particles are spherical, the specific surface area (SSA) can be used to estimate the particle sizes by the following formula

$$SSA = \frac{\frac{V}{4\pi(D_{BET}/2)^3/3} \cdot 4\pi(D_{BET}/2)^2}{\rho V} \Rightarrow D_{BET} = \frac{6}{\rho \cdot SSA} \tag{F.3}$$

where ρ is density, V is volume of powders, and D_{BET} is BET particle size. The BET particle sizes D_{BET} of powders calcined at different temperatures are also listed in Table F.1 for comparison with XRD particle sizes. The particle sizes calculated by the two different methods correspond to each other within experimental errors. This shows that particles are approximately spherical and not agglomerated.

F.3.2 $La_2Zr_{2-x}Mg_xO_{7-\delta}$ (x = 0.1 to 0.4)

F.3.2.1 XRD Characterization of $La_2Zr_{2-x}Mg_xO_{7-\delta}$ (x = 0.1 to 0.4)

XRD patterns of Mg-doped $La_2Zr_2O_7$ (Figure F.2) show that $La_2Zr_{2-x}Mg_xO_{7-\delta}$ remains to be single cubic pyrochlore phase up to $x = 0.3$. When x is increased to 0.4, a second phase appears and it is identified to be monoclinic zirconium oxide. The Rietveld refinement results with Ni as the internal standard are reported for $x = 0$ to 0.3 in Figure F.3. Lattice constants increase with doping level x from $x = 0$ to 0.2 because the ionic radius of Mg^{2+}

is larger than that of Zr^{4+} ($r_{Zr^{4+}}$(VI)=0.72 Å, $r_{Mg^{2+}}$(VI)=0.72 Å; $r_{Zr^{4+}}$(VIII)=0.84 Å, $r_{Mg^{2+}}$(VIII)=0.89 Å—Roman numericals represent the coordination number).

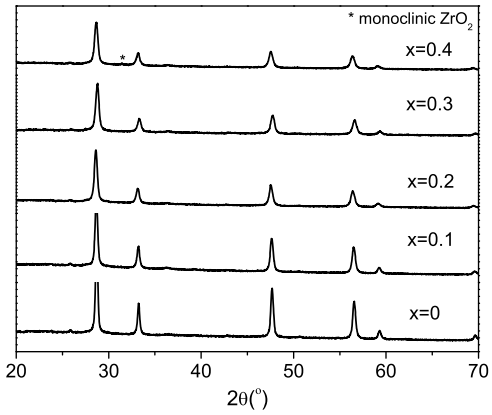

Figure F.2: X-ray powder diffraction patterns of $La_2Zr_{2-x}Mg_xO_{7-\delta}$ (x = 0, 0.1, 0.2, 0.3, 0.4).

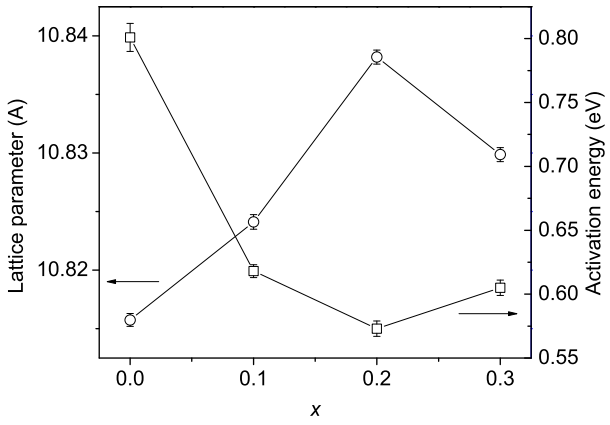

Figure F.3: Lattice parameter and activation energy of grain interior conductivity of $La_2Zr_{2-x}Mg_xO_{7-\delta}$ as a function of Mg doping level.

However, lattice constants decrease when x is increased to 0.3 and the value lies somewhere between that of $x = 0.1$ sample and that of $x = 0.2$ sample. If Mg^{2+} can totally dissolve in $La_2Zr_{2-x}Mg_xO_{7-\delta}$ for $x = 0.3$, it is expected the lattice constant would follow the increasing trend from $x = 0$ to 0.2 and it would be higher than that of $x = 0.2$ sample. This observation implies actually $La_2Zr_{1.7}Mg_{0.3}O_{7-\delta}$ may not be pure although it appears to be single phase in XRD pattern. Thus the solubility of Mg in $La_2Zr_{2-x}Mg_xO_{7-\delta}$ is expected to be only up to $x = 0.2$.

F.3.2.2 Conductivity Measurement of $La_2Zr_{1.9}Mg_{0.1}O_{7-\delta}$

Ionic conductivities of $La_2Zr_{2-x}Mg_xO_{7-\delta}$ were measured by A.C. impedance spectroscopy. Briefly, an A.C. voltage perturbation is applied to the sample and since grain interiors and grain boundaries have different time constants for the response to the voltage so they can be separated in the frequency domain. The advantage of this method is that in many cases, resistances due to grain interiors and grain boundaries can be obtained independently. In order to convert the measured resistances to the real conductivities, one needs to know the geometry of grain interiors and grain boundaries such as the average grain size and the average grain boundary thickness. Following the procedures for calculating grain interior and grain boundary conductivities from the "brick layer model",[125] the true grain boundary conductivity (so-called specific grain boundary conductivity) can be obtained in the absence of microstructural investigations. In this paper, the grain interior conductivities were obtained by applying the dimensions of the pellets to the measured grain interior resistances. The specific grain boundary conductivities were obtained by applying the "brick layer model."

The temperature dependences of grain interior conductivity under H_2O- and D_2O-saturated argon were plotted as Arrhenius plots in Figure F.4. It is obvious that the grain interior conductivity in H_2O saturated argon is higher than that in D_2O saturated argon. The Arrhenius plots of grain boundary and specific grain boundary conductivities (not shown) give the similar behavior, indicating that protons (or deuterons) are the mobile species. The results of detailed analyses of the pre-exponential factors and activation energies are given in Table F.2.

Table F.2: The values of two parameters quantifying the isotope effect

	Grain interior (GI)	Specific GB (SGB)
$E_a(D_2O)$ - $E_a(D_2O)$, eV	0.03 ± 0.01	0.05 ± 0.01
$A(H_2O)/A(D_2O)$	1.04 ± 0.13	0.78 ± 0.14

For proton conductors, the conductivity measured in H_2O saturated atmospheres is higher that measured in D_2O saturated atmospheres. This phenomenon is usually called the isotope effect. Isotope effect of proton conductivity of various proton conducting perovskites has been observed[126,127] and reviewed by Nowick *et al.*[128] In most cases, the activation

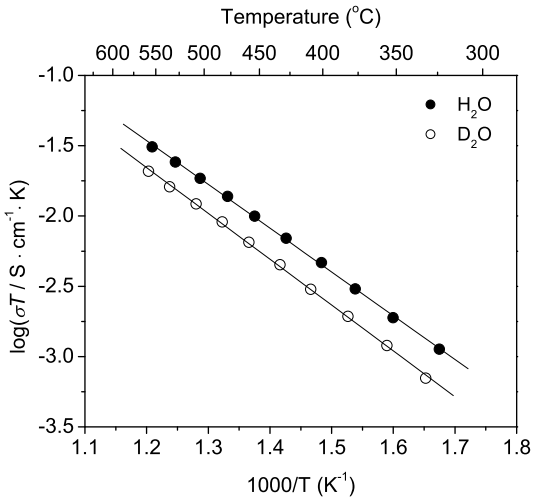

Figure F.4: Temperature dependence of grain interior conductivity of $La_2Zr_{1.9}Mg_{0.1}O_{7-\delta}$ in H_2O-saturated and D_2O-saturated argon.

energy difference is between 0.02 and 0.06 eV while pre-exponential factor ratio A_H/A_D is generally < 1. In this paper, $La_2Zr_{1.9}Mg_{0.1}O_{7-\delta}$ was chosen to investigate the isotope effect and isotope exchange effect in proton conductivity. Both activation energy difference and pre-exponential factor ratio of the isotope effect were discussed on the form of a statistical mechanical transition state theory similar to Bell's semi-classical theory.[129]

The migration of H from one oxygen ion to another one can be written as

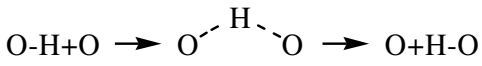

The potential energy surface along the reaction coordinate is plotted in Figure F.5.

According to transition state theory,[130] rate constant can be expressed as

$$r = \frac{k_B T}{h} \frac{q_t(OHO) q_r(OHO) q_v(OHO)}{q_t(OH) q_r(OH) q_v(OH) q_t(O)} \exp\left(-\frac{E_0}{k_B T}\right) = A \exp\left(-\frac{E_0}{k_B T}\right) \tag{F.4}$$

with

$$E_0 = E_b + \frac{1}{2} h\nu_{OHO} - \frac{1}{2} h\nu_{OH} \tag{F.5}$$

where r is rate constant, h is Planck constant, k_B is Boltzmann constant, T is temperature, q_t and q_r are translational and rotational partition function respectively, q_v is vibrational partition function excluding the zero point energy, and ν is vibrating frequency. The initial

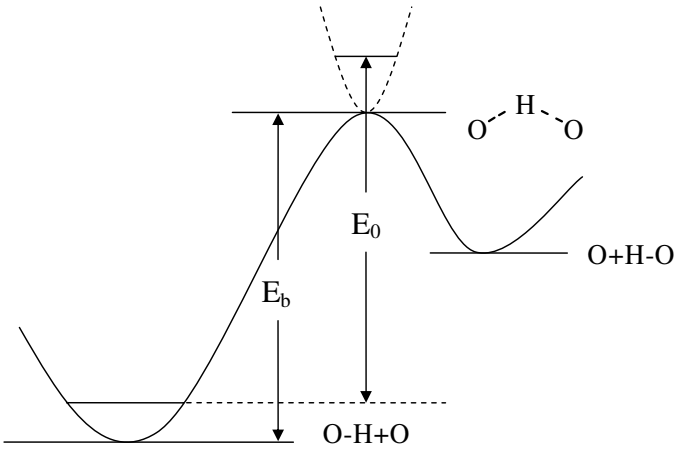

Figure F.5: The potential energy surface along the reaction coordinate.

state is labeled as OH and the transition state is labeled as OHO. A is the pre-exponential factor. E_b is the apparent energy difference between the transition state OHO and the initial state OH and E_0 is real energy difference that includes the zero point energy difference between the two states. The translational and rotational partition functions depend on the mass of the molecules while the vibrational partition functions depend on the reduced mass of the molecules. Since the mass of proton or deuteron is much smaller than that of oxygen, in the discussion of hydrogen isotope effect, we can ignore the translational and rotational partition functions. While the initial state OH has only one normal vibration mode, the transition state OHO is not linear from both theoretical calculations and neutron diffraction experiments.[131–134] Thus the three-atom transition state has 3n−6−1 = 2 (−1 because one degree of freedom has already been singled out in getting the rate constant) normal vibration modes, called OHO_1 and OHO_2 in the following discussion. From (F.4), the ratio of isotope rate constants can be expressed as

$$\frac{r^H}{r^D} = \frac{q_\nu(OHO_1)q_\nu(OHO_2)}{q_\nu(ODO_1)q_\nu(ODO_2)} \frac{q_\nu(OD)}{q_\nu(OH)} \exp\left(\frac{\Delta E}{k_B T}\right) \tag{F.6}$$

where the vibrational partition function, assuming harmonic oscillators, excluding zero point energy is

$$q_v = \sum_{n=0}^{\infty} e^{-nh\nu/k_B T} = \frac{e^{h\nu/k_B T}}{e^{h\nu/k_B T} - 1} \tag{F.7}$$

with

$$\nu = \sqrt{\frac{k}{\mu}} \tag{F.8}$$

where k is the force constant which is the same for the two isotopes, and μ is the reduced mass of the harmonic oscillator. Since the mass of proton or deuteron is much smaller than that of oxygen, the reduced mass can be approximated by the mass of proton or deuteron. The ratio of vibrating frequency of two isotopes are then

$$\frac{\nu_{OH}}{\nu_{OD}} \approx \sqrt{\frac{m^D}{m^H}} = \sqrt{2} \tag{F.9}$$

$$\frac{\nu_{OHO}}{\nu_{ODO}} \approx \sqrt{\frac{m^D}{m^H}} = \sqrt{2} \tag{F.10}$$

where m^H and m^D are the masses of proton and deuteron respectively. Since isotopes have the same chemical properties so it is assumed that E_b is also the same for two isotopes as force constant k. From (F.5), thus

$$\Delta E = E_0^D - E_0^H = \frac{1}{2}h\nu_{OH} - \frac{1}{2}h\nu_{OD} + \frac{1}{2}h\min(\nu_{ODO_1}, \nu_{ODO_2}) - \frac{1}{2}h\min(\nu_{OHO_1}, \nu_{OHO_2}) \tag{F.11}$$

where "min" represents minimum.

For the initial state OH, the vibrating frequency is high (around 3300 cm^{-1} which corresponds to 10^{14} s^{-1}), thus $h\nu_{OH} \approx 6.63 \times 10^{-34}$ J $\cdot$ s $\times$ 10^{14} s^{-1} ≈ 0.41 eV. Taking the temperature to be 300 °C, $k_BT \approx 1.38 \times 10^{-23}$ J $\cdot$ $\text{K}^{-1}\times$ 573 K ≈ 0.05 eV, we can safely make the approximation, $h\nu_{OH}/k_BT \gg 1$. From (F.7), this leads to

$$q_{OH} \approx 1 \tag{F.12}$$

For the transition state OHO, due to the longer bond distances, the vibrating frequency is smaller than that of the initial state.

(a) If the vibrating frequency of the transition state is much higher than k_BT, $h\nu_{OHO}/k_BT \gg 1$, from (F.7)

$$q_{OHO} \approx 1 \tag{F.13}$$

from (F.6), (F.12) and (F.13)

$$\frac{r^H}{r^D} \approx \exp\left(\frac{\Delta E}{k_B T}\right) \tag{F.14}$$

thus the ratio of pre-exponential factor A^H/A^D is around 1. To be more specific, if we assume that vibrating frequency of transition state is half of that of initial state, the difference in activation energy $\Delta E = \frac{1}{2}h\nu_{OH} - \frac{1}{2\sqrt{2}}h\nu_{OH} + \frac{1}{4\sqrt{2}}h\nu_{OH} - \frac{1}{4}h\nu_{OH} \approx 0.03$ eV.
(b) If the vibrating frequency of the transition state is very low, $h\nu_{OHO}/k_B T \ll 1$, from (F.7)

$$q_{OHO} \approx \frac{k_B T}{h\nu_{OHO}} \tag{F.15}$$

from (F.6), (F.12) and (F.15)

$$\frac{r^H}{r^D} = \frac{\nu_{ODO_1}\nu_{ODO_2}}{\nu_{OHO_1}\nu_{OHO_2}} \exp\left(\frac{\Delta E}{k_B T}\right) = \frac{1}{\sqrt{2}}\frac{1}{\sqrt{2}} \exp\left(\frac{\Delta E}{k_B T}\right) = \frac{1}{2}\exp\left(\frac{\Delta E}{k_B T}\right) \tag{F.16}$$

thus the ratio of pre-exponential factor A_H/A_D is around 1/2. Since the vibrating frequency of transition state is negligible compared to that of initial state, the difference in activation energy is approximately $\Delta E = \frac{1}{2}h\nu_{OH} - \frac{1}{2\sqrt{2}}h\nu_{OH} \approx 0.06$ eV. From the above analysis we can see 0.06 eV is basically the maximum activation energy difference predicted. This agrees well with the experimental value.

At the same time, it is worth noting there is also correlation between the pre-exponential factor ratio and the activation energy difference. If the vibrating frequency of the transition state is going to the lower limit, A_H/A_D will approach 0.5 and ΔE will approach 0.06 eV. If the vibrating frequency is going to the higher limit, A_H/A_D will increase to 1 and ΔE will decrease to 0.03 eV. This correlation is true for grain interior and specific grain boundary conductivity in our $La_2Zr_{1.9}Mg_{0.1}O_{7-\delta}$ sample. Grain interior conductivity has smaller ΔE (0.03 eV $<$ 0.05 eV) and larger A_H/A_D (1.04 $>$ 0.78). Since the structure of grain boundary is more open compared to that of grain interior, we would expect the vibrating frequency of the transition state will be lower.

The dynamic isotope exchange effect was also investigated by switching between H_2O- and D_2O- saturated argon while keeping the temperature unchanged at 500 °C. Both grain interior and specific grain boundary conductivities are extracted from the impedance data and they are plotted in Figure F.6. In Figure F.6(a), when the atmosphere was changed

from H_2O- saturated argon to D_2O-saturated argon, there was a gradual decrease in grain interior conductivities. When protons in the oxide were exchanged by deuterons, conductivities will go down from the above discussion on isotope effect. On the other hand, when the atmosphere was changed from D_2O-saturated argon to H_2O-saturated argon, there was a gradual increase in conductivities. Both grain interior and specific grain boundary curves exhibit scissor behaviors. In Figure F.6(b), a closer look at the portion of the curves upon changing atmospheres shows the curves corresponding to grain interior conductivities have larger curvatures compared to grain boundary conductivities. Also, the pivotal point of "grain boundary scissor" is lagging behind that of "grain interior scissor." This observation implies that the exchange rate of isotopes is faster along grain interiors than along grain boundaries. Since the conductivities of grain interiors are higher than those of grain boundaries, it is expected that the transfer of protons or deuterons is faster in grain interiors. This leads to the favored exchange kinetics along grain interiors while the exchange along the grain boundaries would be rate limiting. Thus large grained sample would have a faster rate than the small grained sample.

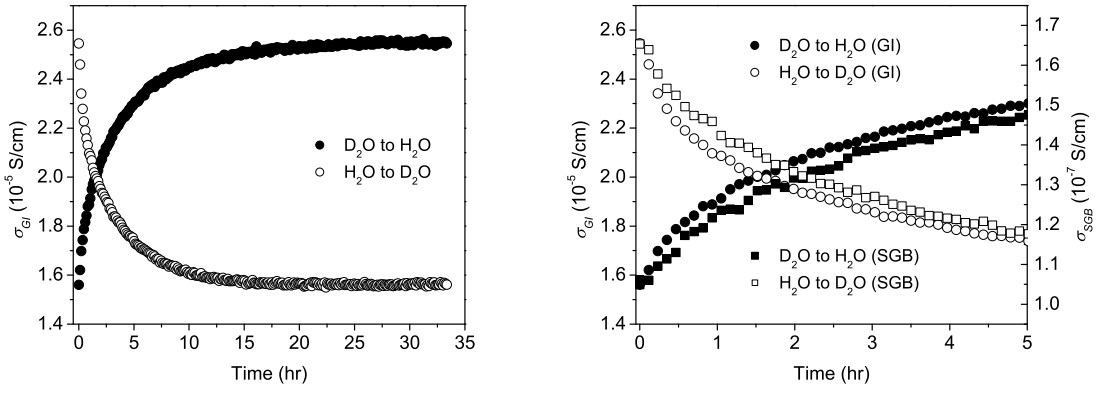

Figure F.6: (a) The dynamic isotope effect of grain interior (GI) conductivities upon change of H_2O or D_2O-saturated argon at 500 °C (b) Comparison of the dynamic isotope effect of grain interior (GI) and specific grain boundary (SGB) conductivities.

F.3.2.3 Conductivity Measurement of $La_2Zr_{2-x}Mg_xO_{7-\delta}$ (x = 0 to 0.2)

The effects of the amount of dopant on the conductivities are shown in Figure F.7(a) and Figure F.7(b) for grain interior and specific grain boundary respectively. The corresponding activation energies are listed in Table F.3.

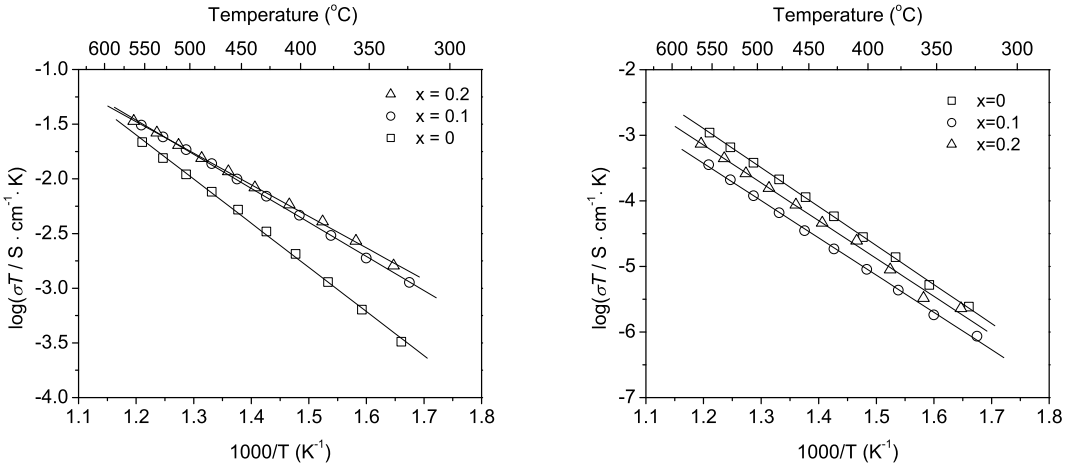

(a) (b)

Figure F.7: Temperature dependence of (a) grain interior and (b) specific grain boundary conductivities of $La_2Zr_{2-x}Mg_xO_{7-\delta}$ (x = 0, 0.1, 0.2) in H_2O-saturated argon.

Table F.3: Activation energies of grain interior and specific grain boundary conductivities as a function of Mg doping level

E_a, eV	$x = 0$	$x = 0.1$	$x = 0.2$
Grain Interior	0.80 ± 0.01	0.62 ± 0.01	0.57 ± 0.01
Specific Grain Boundary	1.18 ± 0.01	1.13 ± 0.01	1.14 ± 0.03

The doped samples exhibit higher grain interior proton conductivities than the undoped sample because of the increased amount of oxygen vacancies in the doped samples. These oxygen vacancies can incorporate more protons into the structure. The relationship of the activation energies of grain interior conductivity and lattice constants are also plotted in Figure F.3. The grain interior activation energies decrease with increasing lattice parameters. Such a correlation was also proposed to exist in ABO_3 perovskites.[135] In structures with larger lattice constants, there is more free volume so it is easier for the migration of protons.

However, in the case of specific grain boundary, the doped samples show lower conductiv-

ities than the undoped samples. This is probably caused by the structural and compositional difference of the grain boundary between the undoped and doped samples. Presumably, the grain boundary composition of the undoped sample is closer to grain interior. The lower specific grain boundary conductivity is only the result of the loose structure. On the other hand, for the doped sample, generally, the dopant tends to be enriched around the region of grain boundary so both the structure and composition might be far different from the undoped sample. Simply the grain boundary phase of the doped sample is not as conductive as that of the undoped sample. The higher conductivity of $x = 0.2$ sample than that of $x = 0.1$ can be explained by the increased oxygen vacancies from the previous discussion.

The conductivity of undoped $La_2Zr_2O_7$ is in the order of 10^{-5} S/cm which is about 2–3 orders of magnitude lower than that of doped perovskite oxide. This implies the structural oxygen vacancy in the pyrochlore structure is probably not active to proton incorporation. Also, the extrapolation of grain interior conductivity of $La_2Zr_{1.9}Mg_{0.1}O_{7-\delta}$ at 600 °C gives 5.4×10^{-5} S/cm which is lower than 3×10^{-4} S/cm of $La_2Zr_{1.8}Y_{0.2}O_{7-\delta}$[120] and 1.0×10^{-4} S/cm of $La_2Zr_{1.985}Ca_{0.015}O_{7-\delta}$.[121]

F.4 Conclusions

The results of this work can be summarized as follows:

(1) Undoped and Mg-doped $La_2Zr_2O_7$ with a pyrochlore structure were prepared by a combined EDTA-citrate complexing method. Pyrochlore phase was formed at 800 °C and the particle sizes are in the range of 0.05 um and 0.17 um from 800 °C to 1100 °C.

(2) $La_2Zr_{2-x}Mg_xO_{7-\delta}$ was single phase up to $x = 0.2$ and lattice parameters increase with Mg doping because the ionic radius of Mg is larger than Zr.

(3) An isotope effect under H_2O- or D_2O- containing atmospheres was observed, indicating that protons (or deuterons) are the mobile species. Both pre-exponential factor ratio and activation energy difference were discussed on the basis of a statistical mechanical transition state theory.

(4) The dynamic isotope exchange effect shows the exchange of isotopes along the grain boundary is the rate-limiting step.

(5) The grain interior conductivity of Mg-doped $La_2Zr_2O_7$ is higher than that of undoped $La_2Zr_2O_7$ while the specific grain boundary conductivity is lower. The extrapolation of grain interior conductivity of $La_2Zr_{1.9}Mg_{0.1}O_{7-\delta}$ at 600 °C gives 5.4×10^{-5} S/cm which is lower than conductivities of Ca or Y doped $La_2Zr_2O_7$.

F.5 Acknowledgments

Funding of this work has been provided by the Department of Energy.

Bibliography

[1] N. D. Cogger and R. V. Webb. Frequency response analysis, Technical report 10, Solartron instruments. http://www.solartronanalytical.com.

[2] B. C. H. Steele. Appraisal of $Ce_{1-y}Gd_yO_{2-y/2}$ electrolytes for IT-SOFC operation at 500 °C. *Solid State Ionics*, 129(1-4):95–110, 2000.

[3] S. R. Wang, T. Kobayashi, M. Dokiya, and T. Hashimoto. Electrical and ionic conductivity of Gd-doped ceria. *Journal of the Electrochemical Society*, 147(10):3606–3609, 2000.

[4] Z. P. Shao and S. M. Haile. A high-performance cathode for the next generation of solid-oxide fuel cells. *Nature*, 431(7005):170–173, 2004.

[5] M. Mogensen, N. M. Sammes, and G. A. Tompsett. Physical, chemical and electrochemical properties of pure and doped ceria. *Solid State Ionics*, 129(1-4):63–94, 2000.

[6] F. A. Kröger and H. J. Vink. Relations between the concentrations of imperfections in crystalline solids, pages 307–435, in *Solid State Physics: Advances in Research and Applications, Vol. 3*, edited by F. Seitz and D. Turnbull. Academic Press Inc., New York, 1956.

[7] I. Riess. Theoretical treatment of the transport-equations for electrons and ions in a mixed conductor. *Journal of the Electrochemical Society*, 128(10):2077–2081, 1981.

[8] A. J. Bosman and H. J. Vandaal. Small-polaron versus band conduction in some transition-metal oxides. *Advances in Physics*, 19(77):1–117, 1970.

[9] H. L. Tuller and A. S. Nowick. Doped ceria as a solid oxide electrolyte. *Journal of the Electrochemical Society*, 122(2):255–259, 1975.

[10] M. Godickemeier and L. J. Gauckler. Engineering of solid oxide fuel cells with ceria-based electrolytes. *Journal of the Electrochemical Society*, 145(2):414–421, 1998.

[11] N. Bonanos, B. C. H. Steele, and E. P. Butler. Chapter 4: Characterization of materials, page 207, in *Impedance Spectroscopy: Theory, Experiment and Applications*, edited by E. Barsoukov and J. R. Maconald. John Wiley & Sons, Inc., Hoboken, New Jersey, 2005.

[12] I. D. Raistrick, D. R. Franceschetti, and J. R. Macdonald. Chapter 2: Theory, page 37, in *Impedance Spectroscopy: Theory, Experiment and Applications*, edited by E. Barsoukov and J. R. Maconald. John Wiley & Sons, Inc., Hoboken, New Jersey, 2005.

[13] J. Bisquert. Theory of the impedance of electron diffusion and recombination in a thin layer. *Journal of Physical Chemistry B*, 106(2):325–333, 2002.

[14] D. R. Franceschetti, J. R. Macdonald, and R. P. Buck. Interpretation of finite-length-warburg-type impedances in supported and unsupported electrochemical-cells with kinetically reversible electrodes. *Journal of the Electrochemical Society*, 138(5):1368–1371, 1991.

[15] B. A. Boukamp. Electrochemical impedance spectroscopy in solid state ionics: recent advances. *Solid State Ionics*, 169(1-4):65–73, 2004.

[16] K. Levenberg. A method for the solution of certain problems in least squares. *Quarterly of Applied Mathematics*, 2:164–168, 1944.

[17] D. W. Marquardt. An algorithm for least-squares estimation of nonlinear parameters. *Journal of the Society for Industrial and Applied Mathematics*, 11(2):431–441, 1963.

[18] M. I. A. Lourakis. levmar: Levenberg-Marquardt nonlinear least squares algorithms in C/C++. `http://www.ics.forth.gr/~lourakis/levmar/`.

[19] J. R. Macdonald. Impedance of a galvanic cell with 2 plane-parallel electrodes at a short distance. *Journal of Electroanalytical Chemistry*, 32(3):317–328, 1971.

[20] J. R. Macdonald. Electrical response of materials containing space charge with discharge at electrodes. *Journal of Chemical Physics*, 54(5):2026–2050, 1971.

[21] J. R. Macdonal. Theory of space-charge polarization and electrode-discharge effects. *Journal of Chemical Physics*, 58(11):4982–5001, 1973.

[22] J. R. Macdonald. Simplified impedance/frequency-response results for intrinsically conducting solids and liquids. *Journal of Chemical Physics*, 61(10):3977–3996, 1974.

[23] J. R. Macdonald. Binary electrolyte small-signal frequency-response. *Journal of Electroanalytical Chemistry*, 53(1):1–55, 1974.

[24] J. R. Macdonald and J. A. Garber. Analysis of impedance and admittance data for solids and liquids. *Journal of the Electrochemical Society*, 124(7):1022–1030, 1977.

[25] D. R. Franceschetti and J. R. Macdonald. Electrode-kinetics, equivalent-circuits, and system characterization - small-signal conditions. *Journal of Electroanalytical Chemistry*, 82(1-2):271–301, 1977.

[26] J. R. Macdonald and D. R. Franceschetti. Theory of small-signal ac response of solids and liquids with recombining mobile charge. *Journal of Chemical Physics*, 68(4):1614–1637, 1978.

[27] D. R. Franceschetti and J. R. Macdonald. Compact double-layer effects in small-signal electrical response. *Journal of Electroanalytical Chemistry*, 87(3):419–422, 1978.

[28] D. R. Franceschetti and J. R. Macdonald. Numerical-analysis of electrical response - biased small-signal ac response for systems with one or 2 blocking electrodes. *Journal of Electroanalytical Chemistry*, 100(1-2):583–605, 1979.

[29] D. R. Franceschetti and J. R. Macdonald. Numerical-analysis of electrical response - statics and dynamics of space-charge regions at blocking electrodes. *Journal of Applied Physics*, 50(1):291–302, 1979.

[30] J. R. Macdonald and D. R. Franceschetti. Compact and diffuse double-layer interaction in unsupported system small-signal response. *Journal of Electroanalytical Chemistry*, 99(3):283–298, 1979.

[31] G. C. Barker. Aperiodic equivalent electrical circuits for electrolyte solution - ideally polarizable electrode and ion and its atmosphere. *Journal of Electroanalytical Chemistry*, 41(2):201–211, 1973.

[32] T. R. Brumleve and R. P. Buck. Transmission-line equivalent-circuit models for electrochemical impedances. *Journal of Electroanalytical Chemistry*, 126(1-3):73–104, 1981.

[33] J. Jamnik and J. Maier. Generalised equivalent circuits for mass and charge transport: chemical capacitance and its implications. *Physical Chemistry Chemical Physics*, 3(9):1668–1678, 2001.

[34] J. Jamnik and J. Maier. Treatment of the impedance of mixed conductors - equivalent circuit model and explicit approximate solutions. *Journal of the Electrochemical Society*, 146(11):4183–4188, 1999.

[35] A. A. Moya, A. Hayas, and J. Horno. Steady-state, transient and small-amplitude AC responses of an electrochemical cell with immobile background charge: A network approach. *Solid State Ionics*, 130(1-2):9–17, 2000.

[36] I. D. Raistrick, D. R. Franceschetti, and J. R. Macdonald. Chapter 2: Theory, page 43, in *Impedance Spectroscopy: Theory, Experiment and Applications*, edited by E. Barsoukov and J. R. Maconald. John Wiley & Sons, Inc., Hoboken, New Jersey, 2005.

[37] D. R. Crow. pages 166-171, in *Principles and Applications of Electrochemistry*. Chapman and Hall, New York, 1984.

[38] H. C. Chang and G. Jaffe. Polarization in electrolytic solutions. 1. Theory. *Journal of Chemical Physics*, 20(7):1071–1077, 1952.

[39] Z. Chen. Comparison of the mobile charge distribution models in mixed ionic-electronic conductors. *Journal of the Electrochemical Society*, 151(10):A1576–A1583, 2004.

[40] M. Kato. Numerical analysis of the Nernst-Planck-Poisson system. *Journal of Theoretical Biology*, 177(3):299–304, 1995.

[41] D. E. Goldman. Potential, impedance, and rectification in membranes. *Journal of General Physiology*, 27(1):37–60, 1944.

[42] D. S. Tannhauser. Theoretical energy-conversion efficiency of a high-temperature fuel-cell based on a mixed conductor. *Journal of the Electrochemical Society*, 125(8):1277–1282, 1978.

[43] M. L. Liu. Distributions of charged defects in mixed ionic-electronic conductors. 1. General equations for homogeneous mixed ionic-electronic conductors. *Journal of the Electrochemical Society*, 144(5):1813–1834, 1997.

[44] J. Pellicer, V. M. Aguilella, and S. Mafe. Validity of the electroneutrality and Goldman constant-field assumptions in describing the diffusion potential for ternary electrolyte systems in simple, porous membranes. *Journal of Membrane Science*, 29(2):117–126, 1986.

[45] D. F. Evans and H. Wennerström. Chapter 3: Electrostatic interactions in colloidal systems, page 139, in *The colloidal domain: where physics, chemistry, biology, and technology meet*. Wiley-VCH, New York, 1999.

[46] A. Tschope. Grain size-dependent electrical conductivity of polycrystalline cerium oxide II: Space charge model. *Solid State Ionics*, 139(3-4):267–280, 2001.

[47] S. Kim, J. Fleig, and J. Maier. Space charge conduction: Simple analytical solutions for ionic and mixed conductors and application to nanocrystalline ceria. *Physical Chemistry Chemical Physics*, 5(11):2268–2273, 2003.

[48] J. S. Lee and D. Y. Kim. Space-charge concepts on grain boundary impedance of a high-purity yttria-stabilized tetragonal zirconia polycrystal. *Journal of Materials Research*, 16(9):2739–2751, 2001.

[49] T. R. Brumleve and R. P. Buck. Numerical-solution of Nernst-Planck and Poisson equation system with applications to membrane electrochemistry and solid-state physics. *Journal of Electroanalytical Chemistry*, 90(1):1–31, 1978.

[50] W. Lai and S. M. Haile. Impedance spectroscopy as a tool for chemical and electrochemical analysis of mixed conductors: A case study of ceria. *Journal of the American Ceramic Society*, 88(11):2979–2997, 2005.

[51] J. Jamnik. Impedance spectroscopy of mixed conductors with semi-blocking boundaries. *Solid State Ionics*, 157(1-4):19–28, 2003.

[52] S. P. Jiang and S. P. S. Badwal. Hydrogen oxidation at the nickel and platinum electrodes on yttria-tetragonal zirconia electrolyte. *Journal of the Electrochemical Society*, 144(11):3777–3784, 1997.

[53] J. Fleig, S. Rodewald, and J. Maier. Microcontact impedance measurements of individual highly resistive grain boundaries: General aspects and application to acceptor-doped $SrTiO_3$. *Journal of Applied Physics*, 87(5):2372–2381, 2000.

[54] X. Guo and J. Maier. Grain boundary blocking effect in zirconia: A Schottky barrier analysis. *Journal of the Electrochemical Society*, 148(3):E121–E126, 2001.

[55] J. S. Lee and D. Y. Kim. Space-charge concepts on grain boundary impedance of a high-purity yttria-stabilized tetragonal zirconia polycrystal. *Journal of Materials Research*, 16(9):2739–2751, 2001.

[56] X. Guo and R. Waser. Electrical properties of the grain boundaries of oxygen ion conductors: Acceptor-doped zirconia and ceria. *Progress in Materials Science*, 51(2):151–210, 2006.

[57] M. Mogensen, N. M. Sammes, and G. A. Tompsett. Physical, chemical and electrochemical properties of pure and doped ceria. *Solid State Ionics*, 129(1-4):63–94, 2000.

[58] M. I. Mendelson. Average grain size in polycrystalline ceramics. *Journal of the American Ceramic Society*, 52(8):443–446, 1969.

[59] J. H. Han and D. Y. Kim. Analysis of the proportionality constant correlating the mean intercept length to the average grain-size. *Acta Metallurgica et Materialia*, 43(8):3185–3188, 1995.

[60] J. J. Sprague, O. Porat, and H. L. Tuller. Mixed conducting gas sensors: atmosphere dependent electrode impedance. *Sensors and Actuators B: Chemical*, 36(1-3):348–352, 1996.

[61] A. Atkinson, S. A. Baron, and N. P. Brandon. AC impedance spectra arising from mixed ionic electronic solid electrolytes. *Journal of the Electrochemical Society*, 151(5):E186–E193, 2004.

[62] P. Jasinski, V. Petrovsky, T. Suzuki, and H. U. Anderson. Impedance studies of diffusion phenomena and ionic and electronic conductivity of cerium oxide. *Journal of the Electrochemical Society*, 152(4):J27–J32, 2005.

[63] J. W. Demmel, S. C. Eisenstat, J. R. Gilbert, X. Y. S. Li, and J. W. H. Liu. A supernodal approach to sparse partial pivoting. *Siam Journal on Matrix Analysis and Applications*, 20(3):720–755, 1999.

[64] T. A. Davis and I. S. Duff. An unsymmetric-pattern multifrontal method for sparse lu factorization. *SIAM Journal on Matrix Analysis and Applications*, 18(1):140–158, 1997.

[65] T. A. Davis and I. S. Duff. A combined unifrontal/multifrontal method for unsymmetric sparse matrices. *ACM Transactions on Mathematical Software*, 25(1):1–19, 1999.

[66] T. A. Davis. A column pre-ordering strategy for the unsymmetric-pattern multifrontal method. *ACM Transactions on Mathematical Software*, 30(2):165–195, 2004.

[67] T. A. Davis. Algorithm 832: Umfpack, an unsymmetric-pattern multifrontal method. *ACM Transactions on Mathematical Software*, 30(2):196–199, 2004.

[68] T. Kobayashi, S. R. Wang, M. Dokiya, H. Tagawa, and T. Hashimoto. Oxygen nonstoichiometry of $Ce_{1-y}Sm_yO_{2-0.5y-x}$ (y = 0.1, 0.2). *Solid State Ionics*, 126(3-4):349–357, 1999.

[69] H. L. Tuller and A. S. Nowick. Small polaron electron-transport in reduced CeO_2 single-crystals. *Journal of Physics and Chemistry of Solids*, 38(8):859–867, 1977.

[70] Y. P. Xiong, K. Yamaji, T. Horita, N. Sakai, and H. Yokokawa. Hole and electron conductivities of 20 mol %-$REO_{1.5}$ doped CeO_2 (RE = Yb, Y, Gd, Sm, Nd, La). *Journal of the Electrochemical Society*, 151(3):A407–A412, 2004.

[71] X. Guo, W. Sigle, and J. Maier. Blocking grain boundaries in yttria-doped and undoped ceria ceramics of high purity. *Journal of the American Ceramic Society*, 86(1):77–87, 2003.

[72] A. Tschope, S. Kilassonia, B. Zapp, and R. Birringer. Grain-size-dependent thermopower of polycrystalline cerium oxide. *Solid State Ionics*, 149(3-4):261–273, 2002.

[73] S. B. Adler. Factors governing oxygen reduction in solid oxide fuel cell cathodes. *Chemical Reviews*, 104(10):4791–4843, 2004.

[74] J. Mizusaki, K. Amano, S. Yamauchi, and K. Fueki. Electrode reaction at Pt,O_2(g)/stabilized zirconia interfaces. Part 1. Theoretical consideration of reaction model. *Solid State Ionics*, 22(4):313–322, 1987.

[75] J. Vanherle and A. J. McEvoy. Impedance characteristics of platinum-electrodes on yttria-stabilized zirconia. *Berichte Der Bunsen-Gesellschaft-Physical Chemistry Chemical Physics*, 97(3):470–474, 1993.

[76] N. L. Robertson and J. N. Michaels. Oxygen-exchange on platinum-electrodes in zirconia cells - location of electrochemical reaction site. *Journal of the Electrochemical Society*, 137(1):129–135, 1990.

[77] J. Mizusaki, K. Amano, S. Yamauchi, and K. Fueki. Electrode reaction at Pt,O_2(g)/stabilized zirconia interfaces. Part 2. Electrochemical measurements and analysis. *Solid State Ionics*, 22(4):323–330, 1987.

[78] W. F. Zhang, P. Schmidt-Zhang, and U. Guth. Electrochemical studies on cells M/YSZ/PT (M=Pt, Pt-Ga_2O_3) in NO, O_2, N_2 gas mixtures. *Solid State Ionics*, 169(1-4):121–128, 2004.

[79] D. Y. Wang and A. S. Nowick. Cathodic and anodic polarization phenomena at platinum electrodes with doped CeO_2 as electrolyte. I. Steady-state overpotential. *Journal of the Electrochemical Society*, 126(7):1155–1165, 1979.

[80] D. Y. Wang and A. S. Nowick. Cathodic and anodic polarization phenomena at platinum electrodes with doped CeO_2 as electrolyte. II. Transient overpotential and AC impedance. *Journal of the Electrochemical Society*, 126(7):1166–1172, 1979.

[81] A. Mitterdorfer and L. J. Gauckler. Reaction kinetics of the Pt, O_2(g)|c-ZrO_2 system: precursor-mediated adsorption. *Solid State Ionics*, 120(1-4):211–225, 1999.

[82] J. Mizusaki, H. Tagawa, K. Isobe, M. Tajika, I. Koshiro, H. Maruyama, and K. Hirano. Kinetics of the electrode-reaction at the H_2-H_2O porous Pt stabilized zirconia interface. *Journal of the Electrochemical Society*, 141(6):1674–1683, 1994.

[83] D. R. Rolison. Catalytic nanoarchitectures - The importance of nothing and the unimportance of periodicity. *Science*, 299(5613):1698–1701, 2003.

[84] J. Kaspar and P. Fornasiero. Nanostructured materials for advanced automotive depollution catalysts. *Journal of Solid State Chemistry*, 171(1-2):19–29, 2003.

[85] M. L. Anderson, R. M. Stroud, and D. R. Rolison. Enhancing the activity of fuel-cell reactions by designing three-dimensional nanostructured architectures: Catalyst-modified carbon-silica composite aerogels. *Nano Letters*, 2(3):235–240, 2002.

[86] H. D. Gesser and P. C. Goswami. Aerogels and related porous materials. *Chemical Reviews*, 89(4):765–788, 1989.

[87] D. R. Rolison and B. Dunn. Electrically conductive oxide aerogels: new materials in electrochemistry. *Journal of Materials Chemistry*, 11(4):963–980, 2001.

[88] A. C. Pierre and G. M. Pajonk. Chemistry of aerogels and their applications. *Chemical Reviews*, 102(11):4243–4265, 2002.

[89] A. Trovarelli. Catalytic properties of ceria and CeO_2-containing materials. *Catalysis Reviews-Science and Engineering*, 38(4):439–520, 1996.

[90] A. Trovarelli, C. deLeitenburg, and G. Dolcetti. Design better cerium-based oxidation catalysts. *Chemtech*, 27(6):32–37, 1997.

[91] A. Trovarelli, C. de Leitenburg, M. Boaro, and G. Dolcetti. The utilization of ceria in industrial catalysis. *Catalysis Today*, 50(2):353–367, 1999.

[92] B.T Kilbourn. *Cerium, a Guide to its Role in Chemical Technology.* Molycorp Inc., White Plains, NY, 1992.

[93] B. C. H. Steele. Oxygen-transport and exchange in oxide ceramics. *Journal of Power Sources*, 49(1-3):1–14, 1994.

[94] B. C. H. Steele. Appraisal of $Ce_{1-y}Gd_yO_{2-y/2}$ electrolytes for IT-SOFC operation at 500 °C. *Solid State Ionics*, 129(1-4):95–110, 2000.

[95] B. C. H. Steele, P. H. Middleton, and R. A. Rudkin. Material science aspects of SOFC technology with special reference to anode development. *Solid State Ionics*, 40-1:388–393, 1990.

[96] S. D. Park, J. M. Vohs, and R. J. Gorte. Direct oxidation of hydrocarbons in a solid-oxide fuel cell. *Nature*, 404(6775):265–267, 2000.

[97] C. HoangVan, R. Harivololona, and B. Pommier. Preparation of single and binary inorganic oxide aerogels and their use as supports for automotive palladium catalysts. *Studies in Surface Science and Catalysis*, 91:435–443, 1995.

[98] E. Abiaad, R. Bechara, J. Grimblot, and A. Aboukais. Preparation and characterization of CeO_2 under an oxidizing atmosphere - Thermal-analysis, XPS, and EPR study. *Chemistry of Materials*, 5(6):793–797, 1993.

[99] M. Hirano and E. Kato. Hydrothermal synthesis of cerium(IV) oxide. *Journal of the American Ceramic Society*, 79(3):777–780, 1996.

[100] M. ValletRegi, F. Conde, S. Nicolopoulos, C. V. Ragel, and J. M. GonzalezCalbet. Synthesis and characterization of CeO_2 obtained by spray pyrolysis method. *Materials Science Forum*, 235:291–296, 1997.

[101] A. Tschope and J. Y. Ying. The effects of non-stoichiometry and dopants in nanocrystalline cerium oxide-based catalysts on redox reactions. *Nanostructured Materials*, 6(5-8):1005–1008, 1995.

[102] M. Pijolat, J. P. Viricelle, and M. Soustelle. Nucleation and growth of ceria from cerium III hydroxycarbonate. *Studies in Surface Science And Catalysis*, 91:885–892, 1995.

[103] T. Masui, K. Fujiwara, K. Machida, G. Adachi, T. Sakata, and H. Mori. Characterization of cerium(IV) oxide ultrafine particles prepared using reversed micelles. *Chemistry of Materials*, 9(10):2197–2204, 1997.

[104] Y. C. Zhou, R. J. Phillips, and J. A. Switzer. Electrochemical synthesis and sintering of nanocrystalline cerium(IV) oxide powders. *Journal of the American Ceramic Society*, 78(4):981–985, 1995.

[105] Y. Liu, H. L. Sun, Q. S. Liu, and H. F. Jin. Co oxidation over ceria aerogel-supported copper catalysts. *Chinese Journal of Catalysis*, 22(5):453–456, 2001.

[106] M. P. Kapoor, Y. Ichihashi, K. Kuraoka, W. J. Shen, and Y. Matsumura. Catalytic methanol decomposition over palladium deposited on mesoporous cerium oxide. *Catalysis Letters*, 88(1-2):83–87, 2003.

[107] M. Lundberg, B. Skarman, F. Cesar, and L. R. Wallenberg. Mesoporous thin films of high-surface-area crystalline cerium dioxide. *Microporous and Mesoporous Materials*, 54(1-2):97–103, 2002.

[108] D. M. Lyons, K. M. Ryan, and M. A. Morris. Preparation of ordered mesoporous ceria with enhanced thermal stability. *Journal of Materials Chemistry*, 12(4):1207–1212, 2002.

[109] D. Terribile, A. Trovarelli, J. Llorca, C. de Leitenburg, and G. Dolcetti. The synthesis and characterization of mesoporous high-surface area ceria prepared using a hybrid organic/inorganic route. *Journal of Catalysis*, 178(1):299–308, 1998.

[110] K. S. W. Sing, D. H. Everett, R. A. W. Haul, L. Moscou, R. A. Pierotti, J. Rouquerol, and T. Siemieniewska. Reporting physisorption data for gas solid systems with special reference to the determination of surface-area and porosity. *Pure and Applied Chemistry*, 57(4):603–619, 1985.

[111] E. P. Barrett, L. G. Joyner, and P. P. Halenda. The determination of pore volume and area distributions in porous substances. I. Computations from nitrogen isotherms. *Journal of the American Chemical Society*, 73(1):373–380, 1951.

[112] G. Reichenauer and G. W. Scherer. Effects upon nitrogen sorption analysis in aerogels. *Journal of Colloid and Interface Science*, 236(2):385–386, 2001.

[113] G. Reichenauer and G. W. Scherer. Nitrogen sorption in aerogels. *Journal of Non-Crystalline Solids*, 285(1-3):167–174, 2001.

[114] M. Pijolat, M. Prin, M. Soustelle, O. Touret, and P. Nortier. Thermal stability of doped ceria: Experiment and modeling. *Journal of the Chemical Society-Faraday Transactions*, 91(21):3941–3948, 1995.

[115] H. Iwahara, T. Esaka, H. Uchida, and N. Maeda. Proton conduction in sintered oxides and its application to steam electrolysis for hydrogen-production. *Solid State Ionics*, 3-4:359–363, 1981.

[116] N. Bonanos. Oxide-based protonic conductors: point defects and transport properties. *Solid State Ionics*, 145(1-4):265–274, 2001.

[117] T. Norby. Solid-state protonic conductors: principles, properties, progress and prospects. *Solid State Ionics*, 125(1-4):1–11, 1999.

[118] K. D. Kreuer. Proton conductivity: Materials and applications. *Chemistry of Materials*, 8(3):610–641, 1996.

[119] M. A. Subramanian, G. Aravamudan, and G. V. S. Rao. Oxide pyrochlores - a review. *Progress in Solid State Chemistry*, 15(2):55–143, 1983.

[120] T. Shimura, M. Komori, and H. Iwahara. Ionic conduction in pyrochlore-type oxides containing rare earth elements at high temperature. *Solid State Ionics*, 86-8:685–689, 1996. Part 1.

[121] T. Omata and S. Otsuka-Yao-Matsuo. Electrical properties of proton-conducting Ca^{2+}-doped $La_2Zr_2O_7$ with a pyrochlore-type structure. *Journal of the Electrochemical Society*, 148(6):E252–E261, 2001.

[122] R. D. Shannon. Revised effective ionic-radii and systematic studies of interatomic distances in halides and chalcogenides. *Acta Crystallographica Section A*, 32:751–767, 1976.

[123] J. E. Huheey. *Inorganic Chemistry: Principles of Structure and Reactivity.* Harper and Row, New York, 1983.

[124] Z. P. Shao, W. S. Yang, Y. Cong, H. Dong, J. H. Tong, and G. X. Xiong. Investigation of the permeation behavior and stability of a $Ba_{0.5}Sr_{0.5}Co_{0.8}Fe_{0.2}O_{3-\delta}$ oxygen membrane. *Journal of Membrane Science*, 172(1-2):177–188, 2000.

[125] S. M. Haile, D. L. West, and J. Campbell. The role of microstructure and processing on the proton conducting properties of gadolinium-doped barium cerate. *Journal of Materials Research*, 13(6):1576–1595, 1998.

[126] T. Scherban and A. S. Nowick. Bulk protonic conduction in Yb-doped $SrCeO_3$. *Solid State Ionics*, 35(1-2):189–194, 1989.

[127] K. C. Liang and A. S. Nowick. High-temperature protonic conduction in mixed perovskite ceramics. *Solid State Ionics*, 61(1-3):77–81, 1993.

[128] A. S. Nowick and A. V. Vaysleyb. Isotope effect and proton hopping in high-temperature protonic conductors. *Solid State Ionics*, 97(1-4):17–26, 1997.

[129] R. P. Bell. *The Tunnel Effect in Chemistry.* Chapman and Hall, London, 1980.

[130] I. N. Levine. *Physical Chemistry.* McGraw-Hill, Boston, 2002.

[131] E. Matsushita and T. Sasaki. Theoretical approach for protonic conduction in perovskite-type oxides. *Solid State Ionics*, 125(1-4):31–37, 1999.

[132] F. Shimojo, K. Hoshino, and H. Okazaki. Stable positions of a proton in Sc-doped $SrTiO_3$ determined by the first-principles pseudopotential calculation. *Journal of the Physical Society of Japan*, 65(5):1143–1145, 1996.

[133] K. S. Knight. Powder neutron diffraction studies of $BaCe_{0.9}Y_{0.1}O_{2.95}$ and $BaCeO_3$ at 4.2 K: a possible structural site for the proton. *Solid State Ionics*, 127(1-2):43–48, 2000.

[134] N. Sata, K. Hiramoto, M. Ishigame, S. Hosoya, N. Niimura, and S. Shin. Site identification of protons in $SrTiO_3$: Mechanism for large protonic conduction. *Physical Review B*, 54(22):15795–15799, 1996.

[135] A. Mitsui, M. Miyayama, and H. Yanagida. Evaluation of the activation-energy for proton conduction in perovskite-type oxides. *Solid State Ionics*, 22(2-3):213–217, 1987.